A Diagnostic Analysis Of A SciTech STAR Class 0.5m Telescope For The Purpose Of High Precision Photometry

Submitted by
John Caleb Barentine, B.S.
Department of Physics

In partial fulfillment of the requirements
For the Degree of Master of Science
Colorado State University
Fort Collins, Colorado
Fall 2002

WE HEREBY RECOMMEND THAT THE THESIS PREPARED UNDER OUR SUPERVISION BY JOHN C. BARENTINE ENTITLED "A DIAGNOSTIC ANALYSIS OF A SCITECH STAR CLASS 0.5M TELESCOPE FOR THE PURPOSE OF HIGH PRECISION PHOTOMETRY" BE ACCEPTED AS FULFILLING IN PART REQUIREMENTS FOR THE DEGREE OF MASTER OF SCIENCE

Committee On Graduate Work

_____ Dr. Roger B. Culver, Adviser

_____ Dr. Eric R. Craine, Member

_____ Dr. Raymond S. Robinson, Member

_____ Dr. Stephen Thompson, Member

_____ Dr. David Krueger, Department Chair

ABSTRACT

A DIAGNOSTIC ANALYSIS OF A SCITECH STAR CLASS 0.5M TELESCOPE
FOR THE PURPOSE OF HIGH PRECISION PHOTOMETRY

The results are presented of a characterization study of a SciTech STAR class
0.5m prototype telescope, provided to the Global Network of Automated Telescopes
(GNAT) for evaluation purposes. This effort was undertaken in part to determine
the attainable photometric precision of data the telescope collects and to relate that
precision to the science goals of the GNAT project.

Consideration was given to mechanical issues involving the telescope and mount,
performance of the CCD detector and reproducibility of photometry results. Obser-
vations of the open cluster M67 were used as engineering data to test the performance
of particular aspects of the system. Practical benefits of this survey include develop-
ment of protocols for data handling and reduction as well as image co-addition and
astrometry.

The following are identified as the principal contributors to photometric error
in the system: an unidentified noise source external to the telescope, non-Poissonian
background noise in the data, poor pointing and guiding, the use of sky flats, potential
undersampling, poor charge transfer efficiency, charge traps on the detector, dust on
the detector, and short exposure times. A large data rejection rate gives rise to
significant gaps in the time-series quality of the data GNAT produces.

The effect these conclusions has upon the GNAT science goals is discussed with
specific reference to how the overall photometric precision affects the potential search
for extrasolar planets in M67 and similar open clusters.

ACKNOWLEDGMENTS

and understanding with which I now approach research.

DEDICATION

This thesis is dedicated to the life and memory of Dr. Karen L. Harvey (1942-2002), who passed away during the weeks shortly before its completion. Dr. Harvey's influence on my professional development is acknowledged with deep appreciation, and she will certainly be missed.

Contents

List of Figures

List of Tables

1. Introduction

Astronomy relies on the detection of light across broad ranges of the electromagnetic spectrum for its success; ultimately, all of the information available regarding distant astrophysical objects arrives as photons of light. It is the job of the astronomer to detect and study the qualities of these photons in order to deduce the properties of the cosmos.

The relatively recent introduction of charge-coupled device (CCD) detectors and cameras, built on a foundation of modern solid state detectors, has revolutionized astronomy. For examples of how routine CCD astronomy has become, see Howell (2000). The very high quantum efficiencies of CCDs (generally 80% or more) have allowed them to effectively replace photographic plates entirely as the detecting medium of choice for modern observational astronomers. This technology has enabled astronomers to obtain photometric data with high precision over fields of unprecedented spatial extent in a single effort. $\leq 1\%$ photometry over a square degree of sky or more is now commonly realized on large-format CCD frames, with night-to-night stability. This precision was formerly limited to single channel photometers until the emergence of CCD imaging technology in the 1970's and 80's. Furthermore, significant efforts have been made to develop photometric data reduction routines utilizing point spread function (PSF) fitting to resolve individual stars in crowded fields – no small feat when one considers the daunting prospect of conducting photometry on

crowded fields with the single channel devices commonly available 25 years ago.

Millimagnitude photometric accuracy, made possible now even for very small instruments (Howell et al. 1999), is opening windows on low-amplitude optical phenomena involving various astrophysical objects. This makes for fertile ground for those with the patience and computing power to reduce large quantities of synoptic observations in the hope of observing previously unknown phenomena. The power of these techniques is important in considering, for example, the future ability of "small" instruments (apertures of 1 m and less) at various world observatories to compete with 8 to 10 m-class instruments for funding priority. Certainly the development of synoptic, high-precision photometric observing programs utilizing small telescopes is critical to their continued existence. This in turn affects the access of graduate and undergraduate students to observing time on these telescopes and the educational opportunities associated with that experience.

In this study, the results of the characterization of one small telescope, designed in part with a goal of observing low-amplitude, time-series phenomena, are presented. This effort was carried out to understand the behavior of the telescope, detector and site and how each element of the system affects the achievable photometric precision. Section 2 contains a description of the motivation for pursuing this study and a broad overview of project goals. In Section 3 the relevant characteristics of the open cluster M67, at which observations were targeted to obtain data for this work, are introduced.

High Precision Photometry (HPP) is discussed in Section 4, specifically as the techniques needed to achieve high photometric precision apply to the Global Network of Automated Telescopes (GNAT) prototype telescope and its science objectives. The GNAT project and the prototype GNAT telescope are covered in Section 5, where results are reported of a lengthy analysis of its abilities and shortcomings in pursuit of the goal of high photometric precision. In Section 6, protocols for the handling and reduction of data from the GNAT telescope from raw images to finished light curves are outlined; some results from photometry of actual data are presented in Section 7. The factors which were found to ultimately limit the photometric precision of the telescope are given in Section 8, and finally in Section 9 the implications these limits have for the long-term science objectives of the GNAT project are discussed.

2. Motivation

By the early 1990's some observers began to report that optical wavelength photometry at a precision around 1% was a practical achievement with small telescopes and could be implemented on a large spatial scale across the night sky. Few groups, however, have yet approached observing in this fashion systematically. Some controversy still exists within the astronomical community about the accuracy of photometry carried out with the two-dimensional pixel array of modern CCDs. Some purists maintain that such results are inherently suspect because the response of individual pixels on large arrays is not well understood; these individuals maintain that only the results from single-channel photoelectric photometers are sufficiently reliable, since a single detecting element is easier to characterize than an array of order 10^6 detecting elements. In this work, the ramifications of this debate are largely ignored and the widely-held presumption that CCD's can, in fact, yield reliable photometry is adopted.

A typical, present day application of HPP is in the search for extrasolar planets (ESPs), which involves generally large-scale, wide-field imagery of the sky in "survey" mode (Borucki et al. (1985) and Brown (2000)). The serendipitous detection of a photometric transit event involving the star HD 209458 in 1999 (Henry et al. 1999) is proof that this discovery method is viable and the current state of photometric precision sufficient to detect the extremely small light amplitude variations

such transits are predicted to have. The goal of wide-field photometric searches is to encompass the largest number of stars in a single frame possible, presuming the probability of seeing a transit event scales with the number of stars monitored. Thus, targeting observations to small regions and/or compact objects is discouraged simply in the name of increasing the probability of a positive detection. Such an approach, while lending itself to serendipitous discoveries of phenomena other than extrasolar planets, overlooks the power of targeting observations to specific associations of stars and other objects. By observing stellar associations in a systematic manner and performing HPP on their member stars, a great deal can be learned about the behavior of stars that share a common evolutionary history at the $\leq 1\%$ light amplitude level. This is a largely unexplored realm within astronomy at high temporal frequency.

The goal of the present work is to analyze the photometric capabilities of the GNAT prototype telescope in order to establish lower limits on the photometric precision of the instrument and site. In addition, a data reduction and analysis pipeline for GNAT was developed to aid in this evaluation. Observation of a set of photometric standards applicable to the imaging system particular to the GNAT telescope will help guide future observations, including a plan to systematically search open clusters for extrasolar planet transits. The first candidate cluster to be routinely observed was M67; observations were thus targeted to a specific open cluster whose characteristics were already well established by more than two generations of observational and theo-

retical astronomers. By characterizing the cluster at the millimagnitude photometric level, the foundation for further work involving clusters and other stellar associations can be established, with the goal of understanding how stars in such associations vary at low amplitudes.

3. Introduction To M67

The open cluster M67 (=NGC 2682; $\alpha_{2000.0}=08^h50^m26\overset{s}{.}1$, $\delta_{2000.0}=+11°48'46''$, see Figure 1) was chosen as a target for a photometric telescope characterization for a simple reason: it is a well-studied cluster used for many years as a testbed of high-precision photometry methods.

According to Montgomery et al. (1993), "With the exception of the Hyades and the Pleiades, few open clusters are as well studied as M67." Several of its characteristics make it an optimal target for observations in this program: 1) its location within 1 kpc of the Sun, 2) low interstellar reddening in its direction (E(B-V)=0.059 mag), and 3) its position of sufficiently high galactic latitude ($b=+31.72°$) to minimize confusion with background stars.

M67's age places it in a unique category of open star clusters: those whose member stars have occupied the Main Sequence for perhaps half their total lifetimes, and yet remain kinematically and gravitationally bound. A color-magnitude diagram for the cluster is shown in Figure 2; the age of the cluster is reflected in the number of evolved stars seen on the upper main sequence and in the giant branch. The data comprising this figure were derived from Schild (1983), Sagar & Pati (1989), Gilliland et al. (1991), Chevalier & Ilovaisky (1991), Montgomery et al. (1993), Anupama et al. (1994) and Kim et al. (1996).

Fig. 1.— M67 in a pseudo-true color image taken from the Second Palomar Sky Survey (PSSII). PSSII captured images of the sky on red- and blue-sensitive plates; for this composite image, an equivalent green frame was contrived by averaging the red and blue images. The resulting RGB frames were co-added to simulate the true colors of the stars in the cluster. The color saturation was then stretched to emphasize the color differences between stars. North is up and east left, and the image is approximately 0.5° on a side.

Only 19 open clusters are thought to be as old or older than M67 (Phelps &

Janes 1994). Hobbs & Thorburn (1991) find a metallicity of the cluster of [Fe/H]=

-0.04 ± 0.12, implying a turnoff age of $\tau = 5.2\pm1.0$ Gyr for the cluster members; τ

is thus of order the age of the cluster itself. This agrees well with the metallicity
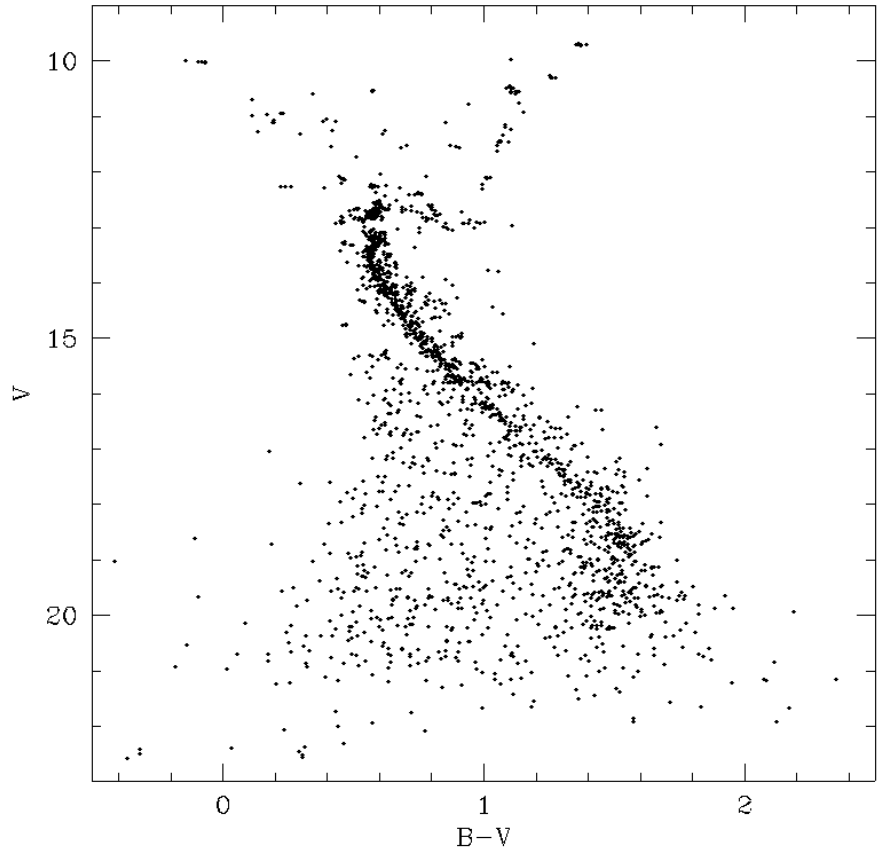
Fig. 2.— A color-magnitude diagram of stars belonging to M67. Data for this figure were taken from sources referred to in the text.

[Fe/H]= -0.05 ± 0.03 derived by Montgomery et al. (1993). Its stars have much in common with the Sun including age, calculated by several groups using color-magnitude data and evolutionary models as $\simeq4$ Gyr (Kim et al. 1996; Dinescu et al. 1995); this agrees well with the white dwarf cooling age of 4.0 Gyr obtained by Richer et al. (1998). There are approximately 1,000 stars which have been identified as cluster members, and most are of similar spectral type and age to the Sun (Fan et al. 1996). It would not be surprising that such an assortment of stars might exhibit the variety

of small-amplitude variability over a range of time scales which are well-suited to the

observational goals of the GNAT project.

The range of V magnitudes represented in the cluster is given in the histogram

in Figure 3, compiled from the stars listed in Table 3 of Montgomery et al. (1993).

Magnitudes were obtained for 1,445 stars down to $\sim m_V = 22.5$ and the histogram
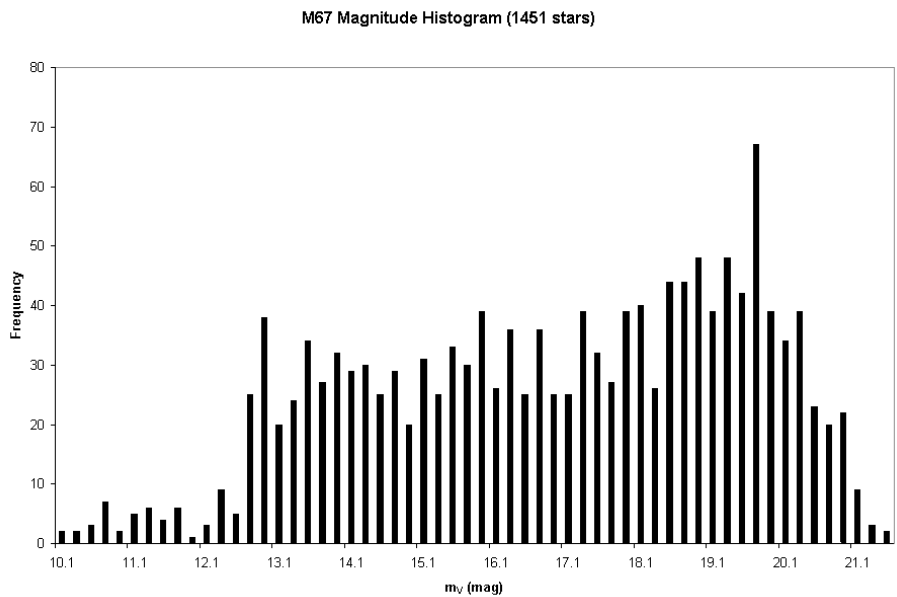
Fig. 3.— Histogram of V-band magnitudes represented among 1,451 stars in the central 15′ of M67, as identified by Montgomery et al. (1993).

here constructed with bins 0.2 mag wide. For reference, a single 60 s integration

performed with the GNAT telescope reaches a limiting V magnitude of approximately

+15. Co-addition of ten such 60 s integrations results in a limit of approximately +18

in V.

The stated reason for choosing M67 as a target begs an even greater question:

why choose an open cluster, much less specifically this one, for an extrasolar planet search? An intriguing observation has emerged in support of searching stellar associations like M67: stars with known planetary systems appear to be more metal-rich than stars without planets (Santos et al. 2001). The recent work reported by Santos *et al.* suggests two broad conclusions: "1) stars with planets are significantly metal-rich, and 2) that the source of the metallicity is most probably 'primordial'." This is at odds with an earlier interpretation that the metal enrichment was due to host stars "engulfing" their planets and incorporating material from differentiated planetary bodies, following a number of models of orbital migration to explain the presence of giant planets in short-period orbits. Yet the same research group reports independent evidence for ^{6}Li enrichment in the spectrum of the star HD82943, known to have at least one planet (Israelian et al. 2001). As primordial ^{6}Li is thought to be destroyed in the early evolution of solar-type stars yet preserved in giant planet atmospheres, this seems to suggest the lithium enrichment of HD82943 took place as it consumed an infalling planet. Thus both mechanisms, primordial enrichment and orbital migration, might explain the association of high metallicity and planets among host stars.

It must be remembered that confirmed knowledge of planets around ordinary stars has come only within the last decade. The number of stars sampled for planets is relatively small and selection bias is likely because of instrumental limits. The

technique for identifying planets explored in this work – photometric transit events – while postulated nearly 20 years ago, was only first demonstrated with data in 1999. The statistics of host stars in planetary systems is likely to change, perhaps drastically, in coming years. For now, planets are pursued where they are statistically most likely to be found: a concentration of evolved, metal-rich stars.

3.1. M67 as a target for high-precision photometry

A number of groups have conducted photometric surveys of M67 in the past 15 years, some at high photometric precision; what follows is a review of the efforts and their results. Emphasis is placed on results that involve categorically *small* telescopes (≤ 1 m) such as the instrument employed in the study presented here.

Several photometric surveys of M67 were reported in the 1980's, though most were not time-series measurements and thus could only reveal parameters such as metallicity and cluster membership. Among the last of these photometric surveys of M67 involving the use of photographic plates to appear in print is the work of Rajamohan et al. (1988). Their work consisted of measuring stellar profile diameters with a measuring engine and performing a least-squares fit to the diameters, using the magnitudes of stars known to be nonvariable as a calibration. They cite residuals of approximately 60 millimagnitudes to their fit, corresponding well with the measurement error of $\simeq 1\mu$m. The authors write, "The nonlinear response of the photographic

emulsion is a distinct disadvantage but as a panoramic detector, its advantage is still unsurpassed." In the intervening years, CCD fabrication technologies have advanced to the point where modern large-format detectors now rival photographic plates for their sky coverage while their high quantum efficiency allows observers to far surpass the precision of Rajamohan et al. CCDs now give high resolution across wide fields of view, and when coupled with their high quantum efficiency, the reasons for the switch from plates are clear.

The first photometric surveys of M67 with electronic detectors were contemporaneous with the final investigations utilizing photographic plates. Gilliland & Brown (1988) were among the first to apply CCD-based differential photometry to the problem of searching for stellar variability among cluster members in M67. This work represented the beginning of an effort to identify p-mode oscillations in other stars, as had already been observed in the Sun; they would later expand their photon-gathering capabilities (see below). A photometric precision of 1.5 millimagnitudes was reported for the 1988 work on the then-#2 36" (0.9m) telescope at Kitt Peak.

Gilliland et al. (1991) did additional work with a set of small (1 m class) telescopes to further push the envelope of achievable photometric precision into the μmag range. Their differential observations of M67 comprised a 14 night time series with 1 min temporal resolution, yielding a noise level of an impressive 0.0008 mag at 13th magnitude over a 9 hr time series. In addition to yielding some promising possible

detections of stellar oscillations among the stars in their sample, their observations resulted in the "serendipitous" discovery of several previously undescribed variables (see Table 1).

In Gilliland et al. (1993), results were reported from a collaboration with six other groups in 1992 to observe 12 program stars in M67 with a network of 4m-class telescopes around the world in 22 telescope nights for a total of 156 hours of observation. Their results yielded an astonishing photometric precision of 250 μmag, enough to suggest that perhaps as many as half the stars in their program group showed promising suggestive evidence for oscillations. Upper limits for oscillation amplitudes were calculated which they claim are near the lower range predicted by theory.

Montgomery et al. (1993) imaged the central one-half degree of M67 in $UBVI$ colors to V=20 and found in comparison with previous efforts that high-precision CCD photometry can "...produ[ce] a uniform set of measurements consistent with the photometric system defined primarily by the Landolt standard sequence." They compiled $UBVI$ colors for 1468 stars within the central 15′ of the center of the cluster and cite a typical photometric error of 10 to 20 millimagnitudes. Additionally, they "...present a sample of stars suitable for use as internal standards in the cluster."

One of the first systematic approaches toward making synoptic, high-precision photometric observations of galactic clusters was reported by Janes et al. (1997).

Monitoring of the clusters NGC 188, M67, NGC 6819 and NGC 7789 using the University of Illinois 1 m telescope at the Mt. Laguna Observatory is cited in conference proceedings, yet to date no results from this effort have appeared in the literature. The Janes et al. monitoring project also appears to be among the first systematic attempts to locate hitherto unidentified low-amplitude variable stars in M67.

Taylor et al. (1999) report observations of immediate concern to this work, as they consist of early engineering data obtained with the GNAT 0.5m prototype (see Section 5 for a description of the GNAT instrument). They observed a 15′ x 15′ field within M67 centered on the so-called 'dipper' asterism (see Montgomery et al. (1993) and Figure 4) encompassing 355 program stars and report a night-to-night
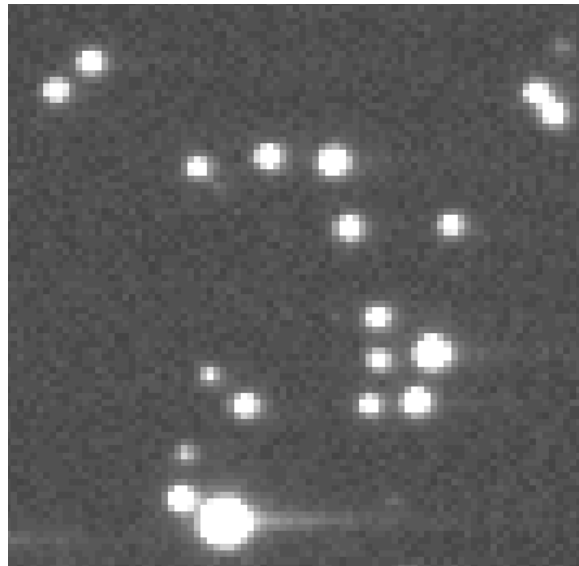
Fig. 4.— The "dipper" asterism of M67 in a 135x135 pixel subsampled region of a single 60 second GNAT frame. North is at top and west at left.

photometric accuracy of 4-5 mmag. Further discussion of this work as it pertains to

the photometric precision of the GNAT telescope will be discussed later.

Sandquist & Shetrone (2001) report observations over ten nights at the Mt. Laguna 1m telescope revealing two previously unrecognized variables (S 757 and S 1016). Their images contained enough stars to perform relative photometry "...of millimagnitude accuracy for many of the stars." Their precision was sufficient to firmly establish variability of some stars at approximately the 30-40 millimag level.

And most recently, results are presented in two papers (van den Berg et al. (2002) and Stassun et al. (2002)) of time series photometry of 990 sources in and around M67 are presented. This work was done with three 1m telescopes yielding BVI photometry to precisions of between approximately 10 and 20 mmag. The goal of this work was to search for optical variability in known cluster x-ray sources; it succeeded in demonstrating optical variations while also leading to the discovery of several new variables. Table 5 in the second paper lists all of the stars characterized as "variable"; due to the novelty of this work, these results have not been incorporated into Table 1 of this work (see next section).

3.1.1.   Known variables in M67

Previous investigations involving M67 stars have revealed a number of stars whose light output varies on both high and low amplitude, as well as differing time scales.

Table 1 summarizes the variables catalogued to date.

"Ordinary variables", i.e., those which we arbitrarily define as having amplitudes ≥ 1 mmag are distinguished in Table 1 from "asteroseismological variables" (see Gilliland et al. (1993)). These stars show variation on the μmag level and are associated with p-mode oscillations such as those observed for over forty years in the Sun. Additionally, a number of suspected variables identified by Gilliland et al. (1991) are tabulated as a separate group.

The intent in compiling references to these variables in the literature and the stars' properties was twofold: 1) to prevent erroneous "detections" of extrasolar planet transit candidates in the data or rediscovery of known low-amplitude variables, and 2) to use these variables as a practical test of the detection capabilities of the GNAT prototype system.

A quick look at the table presents a variety of variable types present in this cluster. Those types[1] are

> **Oscillating blue stragglers**. This is a collective including both δ Scuti and SX Phe variables, characterized by early spectral types (A0-A5), low amplitude (dozens to hundreds of mmag) and short period (0.01-0.2 d).

---

[1]Information on variables is taken from the file `vartype.txt` available electronically from http://vizier.u-strasbg.fr/cgi-bin/getCatFile?II/214A/vartype.txt.

Table 1.   Described Variable Stars In M67

Designation	$\alpha_{1950.0}$	$\delta_{1950.0}$	Period (days)	Amplitude (mmag)	
EX Cnc = F190[1,4]	$8^h48^m50\overset{s}{.}18$	$+12°02'28\overset{''}{.}3$	0.14 ± 0.04	$\sim$4-5	Os
ES III-12[1]	$8^h48^m48\overset{s}{.}47$	$+12°01'58\overset{''}{.}4$	0.06 ± 0.02		Os
AH Cnc = ES III-33[1]	$8^h48^m53\overset{s}{.}74$	$+12°02'15\overset{''}{.}2$	1.00×10^{-4}	$\sim$400	
ES III-2[1]	$8^h48^m49\overset{s}{.}53$	$+12°03'02\overset{''}{.}9$	4.413×10^{-1}	$\sim$70	
ES III-79[1]	$8^h48^m42\overset{s}{.}50$	$+12°07'29\overset{''}{.}7$	2.70×10^{-1}	60	
EU Cnc = II-222[1]	$8^h51^m27''$	$+11°47.0'$	$(8.71\pm0.008)\times10^{-2}$	$\sim$600	
S 1113[2]	$8^h48^m40\overset{s}{.}88$	$+12°14'14\overset{''}{.}6$	2.823094 ± 0.000014		S
F86 = S 1063[2,3]	$8^h48^m29\overset{s}{.}18$	$+12°02'56\overset{''}{.}8$	18.396 ± 0.005	140	S
F61 = S 757[3]	$8^h48^m20\overset{s}{.}73$	$+11°57'12\overset{''}{.}7$	$\sim$0.4		
F105 = S 1016[3]	$8^h48^m32\overset{s}{.}99$	$+11°59'33\overset{''}{.}0$	$\sim$40	30	
ES Cnc = F131 = S 1082[5]	$8^h48^m36\overset{s}{.}60$	$+12°04'43\overset{''}{.}2$	1.0677	$\sim$120	
			Possible Variables[1]		
ES IV-221	$8^h48^m31\overset{s}{.}50$	$+12°02'13\overset{''}{.}1$	10.6	0.6	
F6 = S 1019	$8^h48^m39\overset{s}{.}19$	$+11°59'43\overset{''}{.}8$	9.75	15	
F117	$8^h48^m34\overset{s}{.}61$	$+11°58'19\overset{''}{.}8$	9.79	13	
ES IV-18	$8^h48^m34\overset{s}{.}64$	$+12°02'35\overset{''}{.}8$	5.44		
ES IV-2	$8^h48^m42\overset{s}{.}43$	$+12°00'37\overset{''}{.}8$	1.0065	5.4	
ES II-22	$8^h48^m45\overset{s}{.}32$	$+11°56'45\overset{''}{.}3$	10.1	2.8	
ES II-17	$8^h48^m51\overset{s}{.}97$	$+11°57'51\overset{''}{.}6$	4.88	2.5	
F143 = S 1040	$8^h48^m39\overset{s}{.}64$	$+12°01'06\overset{''}{.}5$	7.97	12	
EY Cnc = ES III-210	$8^h48^m51\overset{s}{.}02$	$+12°01'49\overset{''}{.}3$	8.39	0.22	

Note. — Recognized catalog designations have been used where possible; e.g., ES = Eggen & Sandage (1964).

References. — [1]Gilliland et al. (1991), [2]Mathieu et al. (2000), [3]Sandquist & Shetrone (2001), [4]Zhou (2001)

These stars experience physical pulsation which may yield oscillations with multiple, superimposed periods.

W UMa binaries. Eclipsing binaries with periods of less than 1 day that are generally ellipsoidal in shape due to strong tidal interactions. The component stars in these systems are very nearly in contact and display light curves in which it is generally difficult to discern the exact times of ingress and egress.

AM Her cataclysmic variables. These are close binary systems comprised of a K or M type dwarf and a compact object with a high magnetic field. Their light output is characterized by variable polarization, both linear and circular.

Eclipsing binaries. Binaries whose orbital inclinations are very close to 90° will undergo eclipses as seen from Earth. The depth and duration of these eclipses are determined by the orbital parameters and physical sizes of the component stars. These stars have periods in the approximate range of days.

BY Draconis. Emission-line dwarfs of dKe-dMe spectral type showing quasiperiodic light changes with periods from a fraction of a day to 120 days and amplitudes from several hundredths to 0.5 mag in V. The light variability is caused by axial rotation of a star with a variable degree of

nonuniformity of the surface brightness (spots) and chromospheric activity. Some of these stars also show flares similar to those of UV Cet stars, and in those cases they also belong to the latter type and are simultaneously considered eruptive variables.

Additional variable types may well be present in M67. Since many types are now known involving variation on the mmag level, it is expected that more stars in M67 will be classified as variables in coming years.

4. Introduction To High Precision Photometry (HHP)

Photometry is the process of measuring the amount of light an object radiates which is intercepted by the aperture of a telescope and recorded by a detector coupled to it. What sounds deceptively simple when stated in words turns out to be quite demanding in practice; for some perspective on the delicate task of photometry, see Figure 1 in Howell (1992). In this work, "high precision photometry" is informally defined as that with a precision of better than 10% (0.1 magnitudes).

The major complication to this otherwise straightforward description of what photometry is involves the fact that there are a number of *other* sources of photoelectrons, originating between object and detector, which imprint their signal upon that of the incoming light from the object under observation. It is this unwanted signal that accounts for some of the error associated with measurements made in photometry, and a good photometrist will spend time understanding telescope, detector and other factors in order to minimize that error as much as is practically possible.

A good survey of photometric techniques and potential pitfalls is offered in Dacosta (1992), and the interested reader is referred to this paper for a full indoctrination into the theory of photometry. However, here the discussion of this review is restricted to what DaCosta identifies as the three fundamental tasks of stellar photometry: determining the center of a stellar image, estimating the sky background and calculating

the total amount of light from a star. Only the nuances of the photometry of stars with two dimensional CCD arrays, being germane to the other aspects of this thesis, will be considered here. The additional complications attendant to the surface photometry of extended objects will not be discussed.

The photometry of point sources and compact objects proceeds schematically as follows. First, the photometry target is located on an object frame, and its geometric centroid determined by software algorithms. A software "aperture" is placed around the target, amounting to a mask with zero transmission outside the aperture and full transmission within. These apertures can take on a number of shapes, but in respect to the symmetry of stellar profiles, are nearly always circular. The pixel values within the bounds of the aperture are summed and a raw "flux" from the star reported. Using the definition of the magnitude scale, this flux could then be converted into a magnitude if the gain of the CCD and the wavelength of the observation are known. However, the night sky itself emits a small amount of light, and there are additional concerns over various atmospheric and telescopic effects which can scatter light from outside the aperture to within its bounds. Unless a correction for this additional light is applied to the measured flux within the aperture, a consistent overestimation of the brightness of the star will ensue.

To help mitigate this problem, a sample of the empty sky surrounding the target must be taken in order to know how much signal to subtract from the aperture

corresponding to the sky contribution. There are two subtleties to this process: 1) there is no truly "empty" part of the night sky and 2) variations in response across the detector and small regional variations in sky background prevent unbiased sampling of any given part of the sky. Measuring the flux from otherwise "empty" (i.e., devoid of any star images above the noise level inherent in the detector) sky is still valid because the detector noise sets an arbitrary floor, below which fainter stars cannot contribute significant signal. The spatial restriction is necessitated in order that the background values most pertinent to an individual target are not incorrectly sampled. A solution to this problem commonly in practice is to form a "sky annulus" around the target which has an inner radius larger than the photometry aperture and an outer radius still reasonably close to the target to include the local background effects. "Reasonably close" is subject to the individual peculiarities of the site, telescope and weather, but small values of the annulus width are preferred when possible in order to avoid any "spillover" of light from nearby stars in crowded fields. The flux within the annulus is summed and divided by the number of pixels to arrive at a value for the average background flux per pixel. As the final step, this value is multiplied by the number of pixels in the photometry aperture the result subtracted off the "raw" stellar flux measurement. Correction made, the result is then properly calibrated for instrumental magnitude calculation. This type of photometry is known as *absolute* because it results in a flux with units appropriate to the actual energy received at the

surface of the Earth from the star. It is absolute in the sense that it can be directly and quantitatively compared to others' measurements of the same target object.

Because some astrophysical phenomena manifest themselves at very low light amplitudes, researchers carrying out very sensitive investigations must often consider sources of error beyond those outlined here in order to attain the highest possible photometric precision. One method of eliminating some of these error sources, specifically those whose contributions are invariant with the length of an integration, is *differential* photometry, discussed in Section 4.2. Additional errors are considered in the following section.

4.1. Limitations and sources of error

Understanding the sources of error in HPP is crucial to identifying its ultimate limitations, as well as its practical uses.

The arrival of photons is characterized by *Poisson statistics*[2], and this behavior imprints itself on both the signal received from an object through the telescope as well as the noise which is present in the final data product. This noise results from the random arrival times of photons received at the telescope; though the individual

---

[2]The discussion here of Poisson statistics owes much to the online document "Quick Facts #3: Poisson Noise" by Graham Woan, University of Glasgow, Scotland. It may be found at `http://radio.astro.gla.ac.uk/a2lectures/pw/qf3.pdf`

photons are expected to arrive at an *average* rate r, their arrival cannot be expected at regular intervals in time. The average number of photons arriving in some interval of time τ is estimated by the expectation value $\langle N \rangle = r\tau$. This is only a time-average; in some intervals, more photons than $\langle N \rangle$ will arrive, in others, less will arrive. Their arrival times are referred to as "uncorrelated" events; because photons are bosons (spin-zero particles), their arrivals are unaffected by the presence of other photons already having arrived.

From statistics it can be shown that the probability of detecting some exact quantity N of photons in a given time interval is

$$p(N) = exp(-\langle N \rangle)\frac{\langle N \rangle^{N}}{N!}. \tag{1}$$

This is the Poisson distribution with mean value $\langle N \rangle$ and standard deviation $\sigma = \sqrt{\langle N \rangle} = \sqrt{r\tau}$. What this indicates for purposes of estimating the error of a photometry measurement, represented by σ, is this: if just one measurement of the photon flux is made and N photons recorded, then the best estimate of $\langle N \rangle$ is N. The error associated with the measurement is then $\sigma = \sqrt{N}$. This error is variously referred to by terms such as "Poisson noise," "shot noise" or "root N noise." The significance of Poisson noise is that it sets a lower limit on the achievable noise suppression in any electronic astronomical observation; $\sqrt{N}$ *is* the random error associated with all photoelectric observations. The fundamental signal recorded by a CCD in photometric

data taking is dominated by this noise, regardless of telescope, detector or location; note, however, that for stars the fainter the star, the less Poissonian its signal. This work concentrates mainly on stars bright enough to avoid suffering this effect. In the next section, the term "signal-to-noise" is defined as a figure of merit for these observations, which are found to be fundamentally limited by $\sqrt{N}$.

4.1.1. The Signal-To-Noise Ratio (S/N) and photometric precision

The following discussion and derivation of the signal-to-noise equation is largely appropriated from the work of Howell (1992). The detection of light with electronic devices is essentially a discrete process involving the counting of individual photons with some degree of spatial and temporal resolution. When experiments involve the counting of events per unit interval, it is most generally appropriate to assume an underlying Poisson distribution for the probability of a given event occurring in that interval. A characteristic of this probability distribution is the dependence of the signal-to-noise ratio (S/N) on the square root of the number of observed events (in this case, photon detections):

$$S/N = \frac{S}{N} = \frac{N_*}{\sqrt{N_*}} = \sqrt{N_*} \tag{2}$$

where S is the observed number of counts in the signal, N is the observed number of counts attributed to noise (from all sources), and N_* is the total number of counts in the source. Since the signal-to-noise equation is the basis for calculating the photometric error, it is important to understand the nature of each of its terms. This form of the S/N assumes a system which is essentially noiseless. Of course, this is far from the observed behavior of any "real life" detector; to account for this, additional terms must be incorporated into the working definition of the S/N given here.

A standard equation for the S/N of a point source as measured with a CCD exists, mentioned frequently in the literature (Howell cites no less than six different SPIE Proceedings volumes where it appears), known colloquially as the "CCD Equation":

$$S/N = \frac{N_*}{\sqrt{N_* + n_{pix}(N_S + N_D + N_R{}^2)}} \qquad (3)$$

where n_{pix} is the total number of pixels enclosed in the photometry aperture, N_S is the sky level in electrons/pixel, N_D is the dark current count in electrons/pixels and N_R is the read noise of the CCD in rms electrons/pixel. Equation 3 is used typically as a first-order S/N estimate for point-source observations in order to calculate sample integration times for various detectors. Additional terms are present in the equation which have been left out here; these are usually negligible but in some cases can become dominant if conditions are right. A full treatment of the S/N must include

these extra terms. A very thorough treatment of their derivation is given in Howell & Merline (1995). Their final result is cast in the form

$$S/N = \frac{N_*}{\sqrt{N_* + n_{pix}(1 + \frac{n_{pix}}{n_B})(N_S + N_D + N_R{}^2 + G_o - G^2\sigma_f{}^2)}}. \tag{4}$$

The additional terms are n_B (total number of pixels used in the background determination), G (gain of the CCD in electrons/ADU), G_o (gain when the CCD parameters were determined), and $\sigma_f{}^2$ (variance of the digitization noise). There are two additional terms in Equation 4 which are not present in Equation 3. The first, $(1 + \frac{n_{pix}}{n_B})$, deals with the error associated with the background determination, depending on the number of sky pixels used. The $(G_o - G^2)$ term accounts for the digitization error inherent in the output data. This type of error is a consequence of the conversion of the signal represented by the data from analog to digital format in the camera electronics, and depends largely on the type of A/D converter used. $G_o - G^2$ is taken to be a constant value intrinsically tied to the particular CCD electronics used. It is particularly important in the Equation 4 when a CCD system of large gain is being used.

The type of object under observation is principal in determining which version of the S/N can be reliably used. In the case of Equation 3, when $N_* \gg n_{pix}(N_S + N_D + N_R{}^2)$ the equation reduces to the Poisson result of $S/N = N_*$ which was obtained in Equa-

tion 2. That is to say, for a large enough signal (corresponding to a "bright" source), the result is perfectly Poissonian. This is a useful working definition of what constitutes a "bright" source. However, as the source intensity begins to drop, the additional noise terms of Equation 4 eventually begin to dominate and thus cannot be reasonably ignored.

The reason for grinding through the theory behind the S/N ratio is to set the stage for the introduction of photometric precision σ_p as a derived parameter. It is connected to the S/N though a constant and the CCD gain:

$$\sigma_p = \frac{1.0857}{S/N} \tag{5}$$

$$\sigma_p = 1.0857 \frac{\sqrt{N_* + n_{pix}(1 + \frac{n_{pix}}{n_B})(N_S + N_D + N_R{}^2 + G_o - G^2 \sigma_f{}^2)}}{N_*} \tag{6}$$

This form of σ_p comes from the fact that error is the inverse of the signal-to-noise ratio (the fraction of the total signal comprised of noise), adjusted by the constant that comes from theoretical concerns. Some of the terms in this last equation will be revisited here as they arise in the discussion of tests performed on the system to determine an empirical value of σ_p.

4.1.2. Background determination

In standard two-dimensional aperture photometry of fields which are not crowded with stars (i.e., no chance of overlap of the stellar profiles), an aperture of given size is centered on a source and the flux contained within it is summed. The contribution of background flux is determined by summing the flux in an annulus of sky whose inner radius is larger than the radius of the aperture. Optimal values for both radii are determined empirically, e.g., by the use of growth curve analysis. An average value for the background level in counts/pixel is found by statistical means and then multiplied by the total number of pixels in the source aperture. This result represents the total number of background counts in the source aperture, which is subtracted from the sum taken earlier.

The amount of error introduced into the result of this process depends largely on the number of counts from the source, N_*; for these bright sources, very little error results, so the method by which the background level is determined matters little. Typically, data reduction is not this simple in practice, as only rarely are sufficiently bright sources the targets of observations. Rather, background determination is usually a critical procedure in the case of low S/N observations, and the different statistical modes used to estimate the background are essential to understand. The method of determining the background can have far-reaching consequences for the precision of the photometry of sources over a wide dynamic range of brightness; as

Howell points out, it is unlikely that two methods for taking an average of the background pixels (mean vs. median, to use his example) will lead to the same result for the background value.

During the characterization study presented here, some troubling aspects of the background in the data were noted, discussed in detail in Section 5.3.7. The data suggest a non-Poissonian component to the background levels attributable to some other source than the night sky. This interpretation of the defect has a serious and profound effect on the photometry results presented in this work.

4.1.3. Effects of atmospheric extinction

Every ground-based astronomical observation involves some amount of absorption and scattering of incoming light by the Earth's atmosphere, a term generally referred to as extinction. Young et al. (1991) cite the extinction of a star of color C observed at airmass M as approximated by

$$\Delta Mag = AM - WRMC - \frac{W(RM)^2}{2} \tag{7}$$

where A is the extinction coefficient at the passband centroid, R is the atmospheric reddening coefficient, and W is the bandpass of the filter. AM represents the first-order extinction coefficient; it is the elimination of this term which is the chief virtue of doing differential vs. absolute photometry (see the next section for a discussion of

the differences).

The need for extinction correction in absolute photometry is quite clear – left uncorrected, magnitudes derived from actual data would suffer systematic error as the light from stars was observed through a changing number of airmasses. In the type of differential measurements routinely made by GNAT, any such effects are largely removed under the assumption that the airmass (and hence, the extinction coefficient) changes insignificantly across the field of view of the telescope and the short duration of the integration time. Extinction thus affects all objects on a given CCD frame essentially equally. Everett & Howell (2001) cite the magnitude of any errors arising from extreme color differences in differential photometry at about 1 mmag; furthermore, they cite variations in atmospheric transparency as an additional potential source of error, this time much harder to account for.

Returning to Young's equation, assuming the second-order term is small (W=0.03 for the V band) compared to the leading terms, the differential extinction between two stars is $(WR\Delta C)\Delta M$ where now ΔC is the color difference between the stars in the passband. W is a constant, R is typically small (but scales with airmass), and M only changes by approximately 0.005 across the scale of a single GNAT frame (Taylor et al. 1999). If it is allowed that one of the stars is in the ensemble and the other is being compared against the ensemble, then ΔC ultimately controls the error to the program star's ensemble differential magnitude contributed by extinction. The data

in Table 1 of Montgomery et al. (1993) gives 2.37 as the difference in $B - V$ colors of the reddest and bluest stars surveyed in M67; the distribution of colors is bimodal with peaks at the giant branch and the lower end of the main sequence. The near absence of stars with extreme colors, as expected in an evolved open cluster, strongly reduces the probability that a random selection of two stars would contribute $\Delta C \geq 1$ to the ΔMag. Still, assume the full color difference of 2.37 for a hypothetical example. Further assume an airmass difference of 0.005 as quoted by Taylor *et al.* and R=0.08, a reasonable estimate of the difference between the extinction coefficients in the B and V bands. These values would give the exceedingly small result of $\Delta Mag = 0.00003$ mag. Again, this is the result for the uncertainty contributed to a *differential* measurement between two stars.

Everett & Howell (2001) note "...that for cases in which differential photometry needed to be performed over a wider range of spectral types or airmass, color term effects could be reduced by matching the colors of the ensemble to the stars of interest..." If serious doubt existed regarding the validity of the differential magnitudes obtained, separate ensembles with different color biases (i.e., a "red ensemble" and a "blue ensemble") could well be used. However, as we shall see, there are other sources of photometric error we encountered in this analysis that renders the discussion of color-dependent extinction moot.

4.2. Differential Photometry

This work forsakes the exactness of absolute photometry for the flexibility and high precision of differential photometry, which allows the observer to make use of nights of less than "photometric" quality. The practice of differential photometry has been in use for many years now and its effectiveness is well-established.

In its essence, differential photometry makes use of observing small changes in light output from sources *relative* to other such sources in the same region of sky, thus minimizing the effect of changing atmospheric conditions on a very local scale. On a CCD frame, each object is subjected to the same exposure time; assuming a range of magnitudes among objects recorded on the detector, the S/N for each object will differ, perhaps widely. A direct comparison of the raw light curves (after cosmetic data reduction, of course) is therefore impossible, but these S/N's can be scaled in a way such that a comparison is enabled. The desire for information on the apparent variability of sources motivates the need for this comparison as an important part of differential photometry.

Two broad categories of variability in astronomical sources are assumed: one component attributable to "instrumental noise", which takes into account all sources of noise at the instrumental (telescope + detector) level, and another component reflecting actual variation of the source output itself. The point of differential pho-

tometry is to eliminate, as much as possible, the contribution of instrumental noise, assumed to be invariant both spatially across the detector and temporally during the CCD integration time, without affecting any "real" variability of the source. This elimination assumes that the instrumental and object "noise" are uncorrelated. Instrumental noise can be conceptualized as an irregular pedestal upon which the source signal rests; differential measurements are designed to remove this pedestal, leaving the shape of the incoming signal intact.

However, differential measurements are *relative* measurements that can only be compared internally; that is, comparisons can only be made among objects on one frame taken during a single integration. If the data encompass one or more photometric "standard stars" of known (i.e., previously measured) brightness, then the data can be approximately transformed to a standard photometric system. Differential photometry is useful for science objectives that do not require comparison with other sources of known brightness; examples are color indices and periodicity analyses.

All differential measurements being relative measurements, some sort of reference is required to say what the measurements are relative to, particularly light curves are to be examined for low-amplitude variability. A common approach to this problem is so-called *ensemble differential photometry* in which a group of stars (defining the "ensemble") is chosen whose members are known or at least thought to be non-variable at the level of interest. Any variation in the combined total of their light in a time

series indicates instrumental or sky background noise; hence, by subtracting their combined brightness from that of program objects, any remaining variability ought to be due solely to actual changes in the output of light of the sources. This is why it is crucial that non-variable stars be chosen for the ensemble, for any variability of *any* ensemble stars will necessarily be imprinted on the light curves of every program object.

Use of a word like "non-variable" to describe stars begs the question: are any stars truly non-variable? It is important to consider this factor in cases of photometry being performed at extremely high (≤ 10 mmag) precision, given that otherwise quiescent stars are thought to undergo activity cycles analogous to the 11-year solar cycle. In recent years, efforts to monitor main-sequence stars in the chromospheric H and K lines of Ca II have turned up positive results for very low amplitude, long period variability (GrandPre et al. (2001), Hall & Lockwood (2000) and Radick (2000)) Such long-term variation may not be significant in studies involving short time series on the order of hours, days or even months, yet short time scale phenomena such as large flares on individual stars have been observed in time-series photometric data. Such events would yield variability near the threshold of most precision photometry measurements and could well be mistaken for variation in program objects if an ensemble star were to undergo an eruptive event during a time-series observation. Therefore, the good photometrist is wise to not only understand his or her detector

well, as previously discussed, but to also know the output behavior of ensemble stars thoroughly. In this way, only stars shown to be non-variable at the level of photometric precision of an observation will be included in the ensemble, potentially eliminating the prospect of "false positives" in low-amplitude variation.

5. The SciTech STAR class Prototype Telescope

Data were collected for this project by use of a commercial instrument being tested by the GNAT consortium. In this section, the concept of GNAT is discussed along with details of the prototype's operation which are pertinent to the data collected.

5.1. The Global Network Of Automated Telescopes: Project goals and accomplishments

GNAT is the result of an effort in recent years advancing the utility of small (typically $\leq$ 1m) optical telescopes for conducting survey work and synoptic observations beyond the realm of larger telescopes' usual observing duties. The project will ultimately support a linked network of several identical 1m-class, fully automated (or "robotic") telescopes distributed throughout longitude to provide for continuous temporal monitoring of target objects. Currently, the working end of GNAT consists of a single 0.5m telescope located near Tucson, Arizona that is used for engineering tests in consideration of the final telescope design and matching with an imaging system. The GNAT prototype has been in operation since 1995, and tremendous gains have been made in understanding the challenges associated with building, operating and maintaining such an instrument. Scientific interests involving the telescope include

photometric searches for extrasolar planets and monitoring of photometric standard stars and long-period Mira variables; for a review of GNAT science goals, see Culver et al. (2000). Involvement of students, both at the undergraduate and graduate level, in GNAT research at member institutions has been a priority of the project from its initiation in the late 1980's.

Some science has already emerged from this telescope. Results are available in the areas of photometric monitoring of open cluster stars (Roberts et al. 2000) and general differential photometry (Taylor et al. 1999).

5.2.   The prototype telescope and camera

A full account of the technical aspects of the GNAT prototype design is given by Craine (1999). The prototype arrangement, shown in Figure 5, consists of a 0.5m "STAR" class telescope manufactured and assembled by SciTech Astronomical Research of Foresthill, CA, conceived as a forerunner to the eventual fleet of 1.0m telescopes which would be deployed worldwide. As such, a number of engineering issues exist pertaining to the performance of the STAR class prototype loaned to GNAT which currently restrict both the efficiency with which astronomical observations can be made and the quality of those observations. **The reader should note that GNAT has since declined to purchase the telescope manufactured by SciTech and delivered to GNAT for the purpose of evaluation.** In this work,

Fig. 5.— The GNAT prototype telescope. Image taken from the GNAT project website at `http://www.gnat.org`

generic references to "the GNAT telescope" pertain specifically to the SciTech brand and this specific telescope manufactured by them.

The GNAT telescope was designed by SciTech as the prototype for its "STAR" class of instruments with the goals of the GNAT project in mind: namely, to deploy a series of identical telescopes capable of reliable operation with minimal human intervention. The resulting Ritchey-Chretien design is solid and compact. The 0.5m, f/5.6 primary mirror is housed in an open-frame tube resting in an equatorial split-ring or

"horseshoe" mount. As delivered, the encoders and drive motors on both rotation axes interfaced with a control computer via the SciTech Telescope Control System (TCS). This arrangement was found not to be functional and was replaced by a new control system called GNATCS, developed by Don Epand and licensed to SciTech. Automatic observations are scripted through a proprietary command language called the Automatic Telescope Instruction Set (ATIS)[3], composed of simple commands for slewing the telescope, acquiring a target, rotation of a filter wheel and operation of a CCD imaging camera. ATIS was developed in response to the needs of the growing community of astronomers desiring to operate telescopes automatically (see e.g., Henry (1996)). It has been implemented at facilities such as Fairborn Observatory in southern Arizona, which has had a great deal of success in the operation of multiple automated telescopes, each using ATIS.

The user of a telescope such as the GNAT prototype compiles an ATIS file, consisting of strings of simple, one-line commands, for each observing night and then uploads this file to the host computer at the telescope. In the case of full facility automation, the computer will open the dome and "wake" the telescope at a prescribed hour of the day, then proceed to take requested calibration images before the sky is dark enough to begin observing. When the computer determines that the Sun has reached a predetermined angle below the local horizon, as specified by the user, it

---

[3]ATIS was not developed by SciTech and works independently of its telescope.

proceeds to read the first slew command from the ATIS file, thus commencing observations for the night. As objects are located, the computer issues commands to an attached CCD camera and filter wheel, recording the images onto hard disk in the Flexible Image Transport System (FITS) format, and incorporating certain telescope and/or camera parameters into the FITS file header for later reference. A 486-based PC separate from the telescope control computer is used to control the camera and archive acquired data. Once a sufficient number of images has been acquired and saved to disk, the results can be transmitted elsewhere via FTP or written to CD-R or Zip disk for ease of transport.

The imager for the GNAT prototype is a camera built by Roy Tucker of Southwest Cryostatics in Tucson, Arizona (Tucker 1994). It uses a SITe TK512 CCD array manufactured by Scientific Imaging Technologies, Inc., of Tigard, Oregon. The TK512 comprises an array of 512x512 pixels, each pixel having nominal dimensions 24μm x 24μm. It has low specified values of dark current and readout noise, high charge transfer efficiency, and a full well depth of approximately 350,000 electrons. The chip, mounted in a cryostat, is cooled by a four-stage thermoelectric cooling scheme, and uses a running-water cooling bath for heat exchange outside the telescope. Consistent operating temperatures as low as about -60° F have been achieved and are stable over periods longer than one night, minimizing the effects of thermal cycling on chip performance.

5.3. Optical characterization of the GNAT prototype

Gauging the photometric precision of the GNAT prototype is of critical importance in evaluating its use in an intended long-term project to monitor stars in M67 for extrasolar planet transits. To this end a series of tests, performed on actual data, were devised to evaluate various parameters of the telescope and camera as applies to photometric precision. Where possible, measured system parameters are compared to manufacturers' specifications and developed an informal "SciTech protocol" of data handling to yield the most reliable operation of a telescope found to have a host of problems. The experimental method proceeded as follows: First, some important detector parameters (linearity, response, charge transfer properties) were examined, followed by tests of the quality of the telescope's optical components. Finally the impact of the telescope's mechanical systems on image quality was considered; additional comments concern other problems present in the data which affect their quality, such as pattern noise.

5.3.1.   General performance of the SITe TK512 detector: linearity, response and charge transfer efficiency

At the heart of any photometry program is the reliability of the detector to yield reproducible results. A number of characteristics of CCDs can be measured to

help determine that reliability. The linearity of the detector's response to light was measured over the Johnson V band, a wavelength range approximating the "visual" response of the human eye. To assess the linearity under "real-world" operating conditions, measurements were made of the instrumental magnitudes of 54 stars in M67 of known V magnitude with PSF photometry (see Section 6.5). These stars have published V magnitudes which range from +12.4 to +13.6, placing them among the brighter stars on the frame; they are representative of the range of magnitudes for which the GNAT project hopes to obtain precise photometric results. Data are shown in Figure 6. As expected, the result is strongly linear, with a correlation coefficient of r=0.993 from a least-squares fit. The data points in Figure 6 were deliberately averaged over fifteen nights spanning a total window of 56 days' time to check for long-term linearity variations. No evidence exists in these measurements to indicate non-linearity over the range of magnitudes of program stars in M67. A further affirmation of the quality of the detector's results can be obtained by comparing the measured signal-to-noise ratio (S/N) of stars imaged by the detector to theoretical models. Such a model, based on the work of Howell (1992) has already been reviewed here; his final, working definition of the S/N has been further refined to match the particular characteristics of the GNAT prototype and the result appears in Taylor et al. (1999):

$$(S/N)^2 = \frac{1}{n/g + R_{eff}{}^2 + ((g^2 - 1)/12)/n^2 + (1/200)^2} \qquad (8)$$
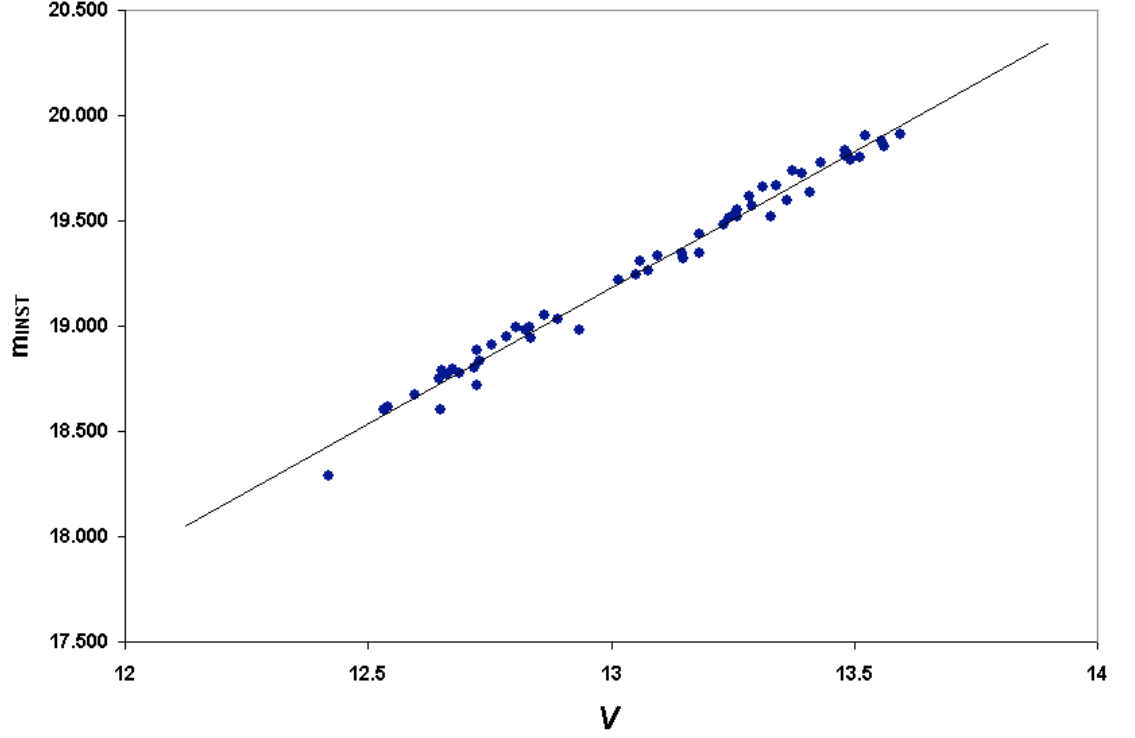
Fig. 6.— Instrumental magnitude versus V magnitude for a sample of 54 stars in M67. m_{INST} was determined by averaging the results of PSF photometry on 102 individual 60 s integrations of M67 taken over 15 nights. A least-squares fit to the data is superimposed.

where n is the number of background-subtracted counts (i.e., corrected flux within the photometry aperture), g is the gain of the detector and R_{eff} is the effective read noise of the camera controller. Values of g=13 and R_{eff}=1, as provided by Eric Craine (GNAT) from engineering data taken earlier with the camera, were used in calculation of model S/Ns. Aperture photometry results for 784 stars within approximately 15′ of the center of M67 are plotted in Figure 7 along with model S/N values calculated over the same flux interval. Good agreement between model and data is evident in this plot, indicating the reliability of current estimates of g and R_{eff} as well as the
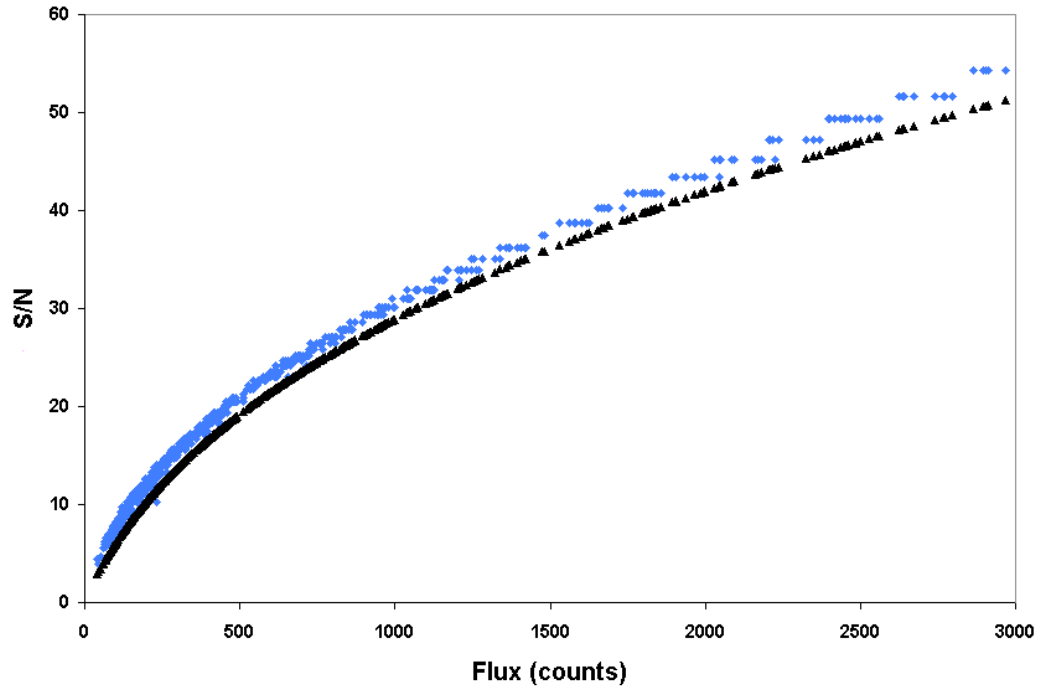
Fig. 7.— Signal-to-Noise Ratio values for 784 stars in and around M67 (blue diamonds) plotted as a function of the corrected flux within a 5-pixel radius aperture. The black squares overplotted represent "model" S/N values obtained with Equation 8.

response of the detector over a range of magnitudes.

Many of the brighter stars in M67 imaged by the GNAT prototype show signs of what, at first glance, would appear to most observers as saturation along rows. This effect is manifested in the form of bright "spikes" trailing away from those stars in the direction antiparallel to that in which the CCD is read. An example of this phenomenon is presented in Figure 8, which shows several bright stars in M67 near the "Dipper" asterism. An examination of pixel values of these stars leads to a conclusion ruling out saturation, as the values fall far below the full well-depth of the CCD and
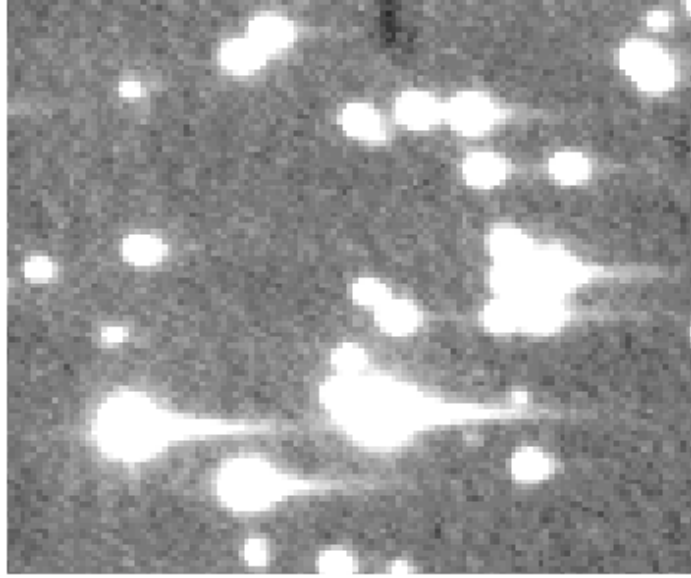
Fig. 8.— A sub-region taken from a coadded image made on 30 January 2001 comprising nine individual 60s integrations. The effects of poor Charge Transfer Efficiency (CTE) can be seen in the form of bright "spikes" running antiparallel to the read direction from the brighter stars.

inside the threshold for A/D saturation. The asymmetry of the spikes is strongly suggestive of poor Charge Transfer Efficiency (CTE) native to the SITe chip and its associated electronics.

CTE is a measure of how efficiently photoelectrons, produced in the bulk semiconductor of the detector pixels upon exposure to light, are shifted from pixel to pixel in the readout process. The efficiency itself is defined as the ratio of charge transferred from a given pixel to the next adjacent pixel in the readout direction to the amount of charge actually generated during an integration. Howell (2000) cites values of near 0.99999 for "modern" CCDs. Significantly lower values of the CTE are typically indicated by residual amounts of charge being "left behind" as the CCD

is read out, resulting in a continuous series of ghost images of the bright stars (i.e.,

the fuller charge wells) emanating in the direction opposite that of the readout. The

trails extend until the amount of residual charge matches the noise level, into which

the ghosts disappear. Therefore, even the fainter stars, that is, those *not* showing

evidence for trails on visual inspection of an object image displayed with Ximtool,

probably have the same kind of tails. Figure 9 shows a line plot taken through the
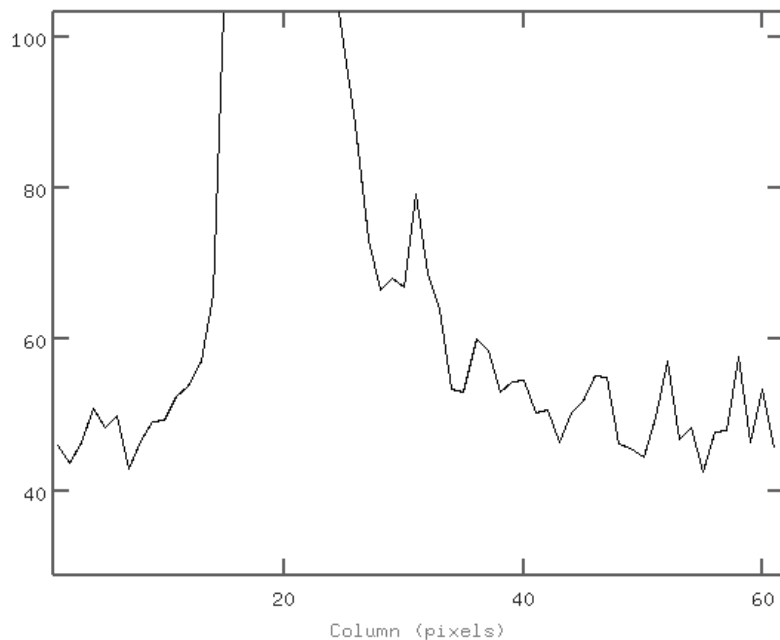
Fig. 9.— Line plot through an undesignated bright star on the GNAT M67 "A" field
in an object image taken on 25 January 2001. The scale of the plot has been adjusted
to show the structure in the right wing of the profile.

centroid of a bright star in M67, selected to illustrate this effect. The upper half of

the central, brightest part of the star is beyond the upper limit set on the ordinate,

such that the structure evident in the wings of the star can be seen. The noise level

in the left wing of the stellar profile sets a context for the right wing, which has levels

clearly above the noise. These elevated levels are maintained for nearly 30 pixels be-

fore returning to the level of the noise, an observation consistent with the qualitative

information in the previous figure.

To quantify the CTE in the SITe detector, the contributions to a stellar image

on a typical object frame from both the star itself and the CTE spike were measured;

division of these values gives a ratio representing the CTE. Pixel values in a region

around the same star whose profile is plotted in Figure 9 were measured using the

IRAF[4] task[5] `imexamine`; the cursor is placed over the region of interest and a 'z'

keystroke returns pixel values in an 11x11 pixel grid centered on the position of the

cursor as a row-column matrix. This process was repeated four times to produce a

matrix of 11x44 entries to cover the entire length of the CTE spike plus a few pixels

on either side in order to properly estimate the local background value in the region.

These additional pixel values were averaged, yielding a mean value of 45.96 counts

and $\sigma = 3.25$ counts. A 3σ detection threshold was selected in order to retain as

many counts within both the star and the CTE spike while remaining comfortably

---

[4]IRAF is distributed by the National Optical Astronomy Observatories, which are operated by the Association of Universities for Research in Astronomy, Inc., under cooperative agreement with the National Science Foundation.

[5]As a matter of convention in this thesis, IRAF task names, task packages, task parameters and image header parameters will be identified with different cases and typefaces. Tasks will use a 'terminal' typeface (e.g., `ccdproc`), task packages will use small capital letters (e.g., DAOPHOT), task parameters will be given in lowercase italics (e.g., *output*), and header parameters will be given in all capital letters in normal text style (e.g., EXPTIME).

above the background level; pixel values in the matrix which fell below the cutoff 3σ above background were discarded.

Estimating the flux contained strictly within the stellar PSF proceeded as follows. The center of the star was located in pixel-value space by finding the highest pixel value in the array; this point also approximately coincides with the centroid of the star on the CCD, as expected. A line drawn along a column at this position divided the stellar profile roughly in half along the rows. The pixel values in the stars to the left (i.e., lower pixel numbers in x) of this dividing line were summed and the result multiplied by two in order to estimate the total flux due *only* to the star. Next, the total flux from both star and CTE tail was determined by adding all pixel values together which were spatially contiguous above the 3σ threshold. The estimated star flux was 74,621 counts and the star + spike total was 79,391 counts, yielding a CTE estimate of 0.9399. This value falls seriously short of the value for "good" CTE cited by Howell and the values of 0.99995-0.99999 at -45°C specified by the manufacturer. CTE is among the detector parameters which is under some direct discretion of the user; the clocking voltage of the chip, controlled in the camera electronics, must be optimized in order to result in the highest achievable CTE value. Camera designer Roy Tucker has indicated to the author privately that this optimization has not yet been performed, but the results of this investigation have made that goal a priority for short-term improvements to the GNAT system.

The SITe chip is generally well-suited to GNAT science objectives, both cosmetically and performance-wise. It has a linear response over a large dynamic range, follows the predicted S/N model well, and at worst, displays correctably low CTE.

5.3.2. Optical aberrations

Detection issues are not the only factors which influence the final photometric precision achievable with a given telescope and detector. Implicit in the assumptions of the error and S/N formulae are good optical collimation, high throughput and distortion-free transmission of light from front end to focal plane. To this end, GNAT data were examined for the telltale signs of any anomalies in the optics which may contribute error to photometry performed with the telescope.

Examination of a few object images quickly reveals an anisotropy of stellar profiles as imaged by the telescope onto the detector. In an ideal telescope, with well-collimated optics, a true point source will be imaged into a circularly-symmetric PSF with an image diameter fundamentally limited by the condition for diffraction by a circular aperture. For Earth-based telescopes, the size of the diffraction-limited PSF is augmented by the contribution due to the "smearing" effect of seeing, as the point source is imaged through the turbulent cells in the atmosphere before ever reaching the telescope. Extremely bad seeing, on the order of tens of arcseconds or more, will tend to enlarge the PSF well beyond the diffraction limit, but will generally preserve

its circular shape provided essentially perfect optical alignment. It should also be noted that a tendency toward elliptical profiles is natural for any telescope observing stars at increasingly larger airmasses due to differential refraction caused by the atmosphere.

Examination of stars imaged with the GNAT prototype reveals a significant deviation from the ideal case just described. This effect is manifested as a significant ellipticity of the images with the long axis of the PSF along the CCD rows. Figure 10 shows a contour plot of a typical stellar profile on a GNAT object image. This
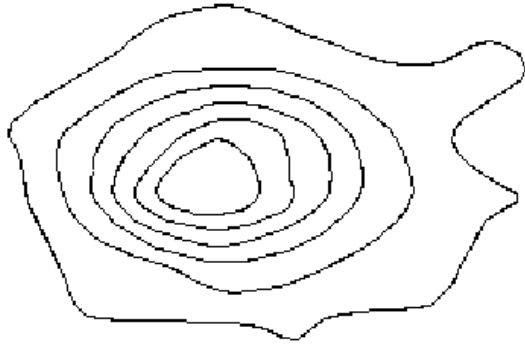
Fig. 10.— A contour plot of the star I-51 taken from object image P51935HG, obtained on 25 January 2001.

figure was made using the IRAF task `contour` with six contours drawn to eliminate background artifacts and focus attention on the shape of the profile. The ellipticity of such a profile can be calculated with the relation

$$e = \frac{R_e - R_p}{R_e} \qquad (9)$$

where R_e is the "equatorial" or semimajor axis of the ellipse and R_p is the "polar" or semiminor axis of the ellipse. Values of R_e and R_e, expressed in pixels, can be obtained by fitting Gaussians across the stellar profile through its centroid in x and y, noting the FWHM of the profile in each direction. The case in Figure 5 is somewhat extreme, with a value of $e = 0.36$; typical values for most stars in GNAT images are near 0.1 to 0.2. However, when the elliptical PSF is convolved with profile distortions due to seeing, the ellipticity can vary significantly. In Figure 11 the calculated profile ellipticity of the star I-51 as a function of time is plotted over several hours of observing on the night of 25 January 2001. The value of e is seen to range from nearly circular at
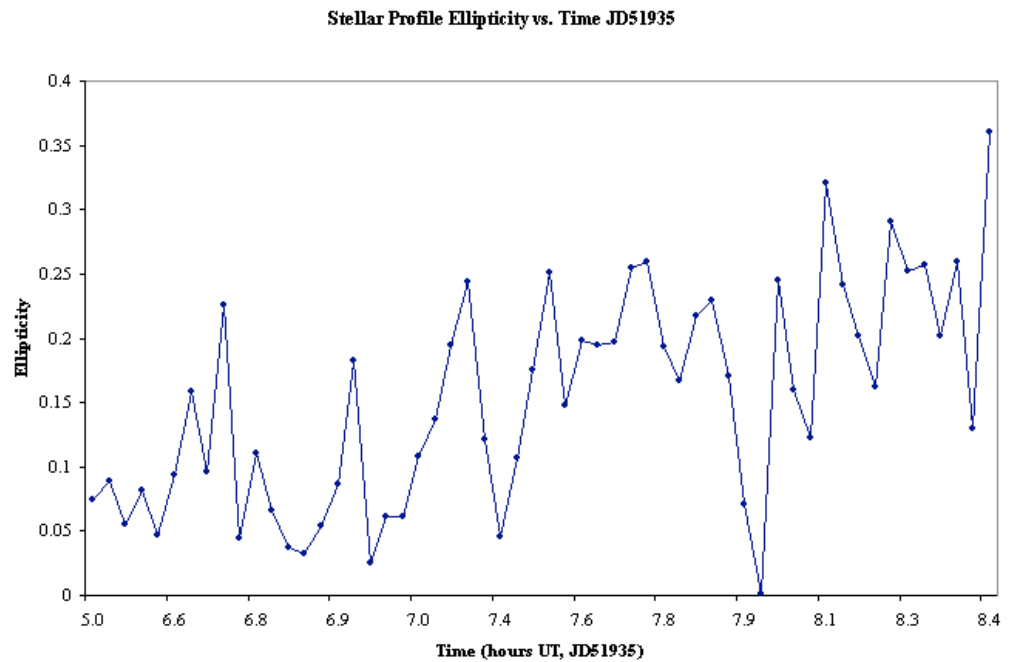
Fig. 11.— Ellipticity of the PSF of star I-51 as a function of time on the night of 25 January 2001. N is up and W at left in this image.

a value of zero up to a maximum near 0.35. While the numerical value of e is variable, the orientation of the ellipse is generally constant, with R_e in alignment with the rows of the CCD. These observations can be largely accounted for by a combination of collimation and guiding errors rather than the position of the telescope on the sky, as most observations analyzed here were made at relatively low airmass. Temporally-consistent ellipse orientation is indicative of poor collimation in the telescope optics, while the variable ellipticity is due to problems in guiding. Of these two error sources, the guiding issue appears to contribute more to e than the optical collimation, given how widely the data in Figure 6 vary and the known tracking problems outlined in the following section. While better collimation would reduce the ellipticity of the stellar profiles imaged with the telescope optics, any gains in PSF shape would be offset by the losses due to guiding errors.

It is thought, however, that this ellipticity problem is not severe enough to warrant correction, especially in consideration of the fact that such a remedy would involve making changes to the alignment of the telescope optics. PSF photometry will account for the noncircular stellar profiles to a reasonable extent, and at this time no evidence exists to suggest that, for example, `daophot`, which is being used to perform PSF photometry, is failing to fit PSFs correctly. Other photometry methods investigated as part of formulating a GNAT photometry protocol can be modified to accommodate noncircular stellar PSFs.

5.3.3.   Tracking issues in the SciTech telescope

As a prototype instrument, a certain degree of mechanical irregularities is expected to be observed in the SciTech telescope, and it is in the process of testing its performance under "real world" conditions that these irregularities become evident. A major limitation to the efficacy of any HPP survey using the GNAT prototype in its current incarnation is the inability of the telescope and drive systems to accurately track objects moving at the sidereal rate with sufficient consistency.

SciTech's major claim of innovation in the manufacture of small telescopes for serious research work lies in its physical telescope design and corresponding tracking method. The design for the GNAT mount incorporates a so-called "split ring" polar bearing design, a feature common in large ($\geq$2m, generally) optical telescopes. The edge of the "horseshoe" is a steel ring resting on rollers in the telescope base; by rotating the rollers at the proper rate, the telescope can be made to track through the corresponding rotation of the polar axis via friction. This concept relies on the accuracy to which the outer ring has been machined; departures from a theoretically "perfect" curve will yield tracking errors as faulty portions of the ring pass over the base rollers. This is an acknowledged phenomenon on the part of SciTech; their solution was an attempt to program, in software, a correction to the errors by "mapping" the locations of the faults in the ring's machining and, via a drive corrector, altering the tracking rate as each defect passes over the base rollers to compensate for the

RA drift which would otherwise be induced. Such a process is akin to similar solutions devised by other commercial telescope manufacturers to reduce or eliminate the effects of, for example, the common problem of periodic drive errors. Note also that there are significant tracking errors in declination, which uses a similar split ring approach. In the case of neither axis has the tracking been found reliable.

Implementation of the software correction solution has so far failed to result in a satisfactory improvement of the tracking accuracy. Approximately 30% of the images obtained by the telescope in its current state are routinely discarded before being calibrated due to blurring or trailing of stellar sources, resulting from tracking inaccuracies. The imperative need for a solution to this problem is clear upon consideration of this rejection rate.

A number of distinct image defects, severe enough in their effects to warrant outright rejection of images from GNAT data sets, has been identified and a classification scheme for these defects devised. Figure 12 gives examples of several of the tracking anomalies noted in GNAT data, while the frequency of each type in the GNAT data set is given in Table 2.

Colloquial names for each type of defect are:

"Slight Blur": Small drive errors deviating from the true sidereal rate result in small (2-3 pixel) blurring in the RA (i.e., along CCD rows). These
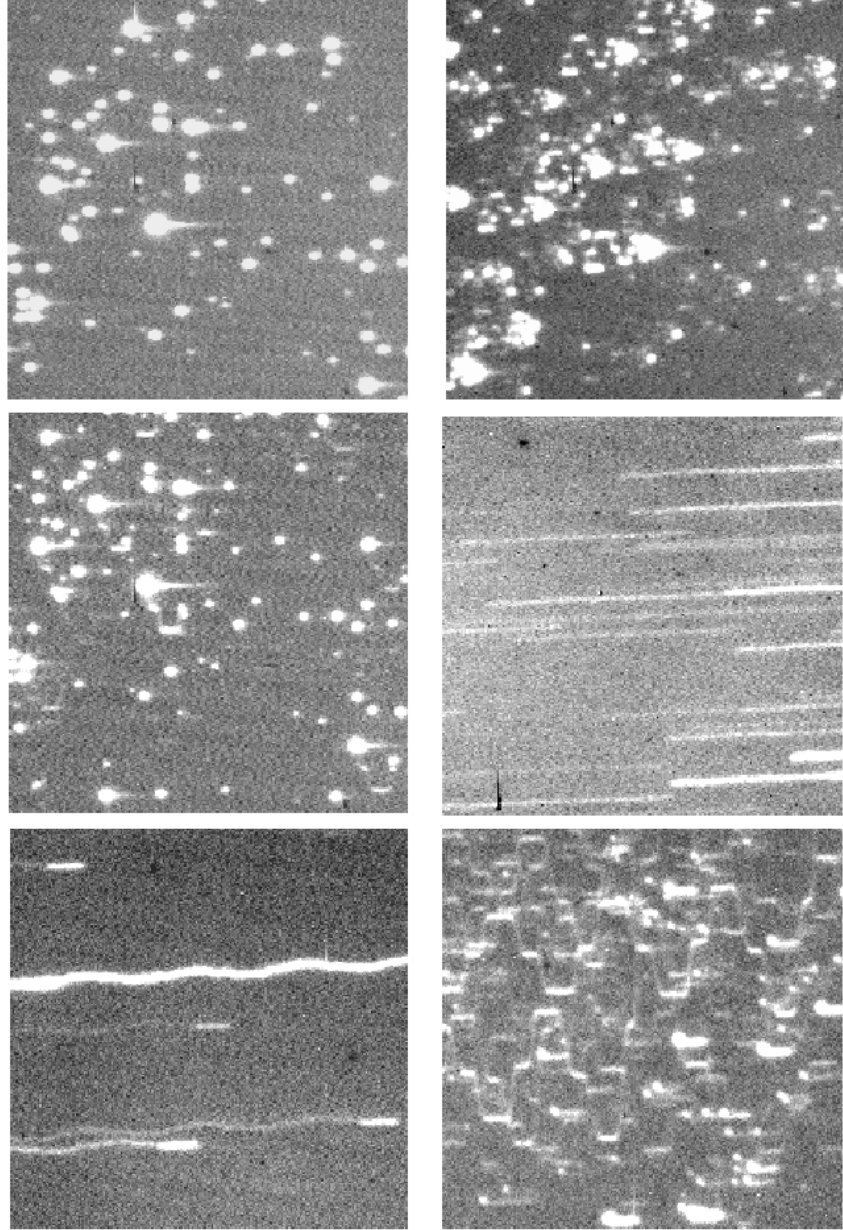
Fig. 12.— A taxonomy of image defects in the GNAT prototype system resulting in image rejection. Left to right, top to bottom they are: "Slight Blur", "Doubled", "Artifacts", "Trailed", "Wiggled", "Weird Blur". Descriptions of each type are given in the text. Images are 219x219 pixel subsamples of full, uncalibrated data frames.

image yield PSFs with high ellipticity that cannot be accurately modelled for PSF photometry.

"Doubled": Multiple ghost images of stars on individual CCD frames, often convolved with two-dimensional tracking errors, yield phantom targets for automatic star detection with, e.g., `daofind`. "Doubled" is the term given to images showing two or more sets of ghost images, since they superficially resemble double-exposed photographs. When the telescope control software thinks it has acquired the wrong field for whatever reason, it continues jogging the telescope around the field attempting to locate its target. The camera, having already started an integration, records a star image each time the telescope stops in-between jogs.

"Artifacts": A combination of single-exposed star images and two-dimensional tracking errors resulting in stars with 'tails' and other spurious appendages.

"Trailed": Severe tracking errors in RA result in star trails running almost, if not completely, off the frame within a single integration. This effect correlates to the direction in RA (east or west) from which the field is initially acquired in the duty cycle. Approaching from the east appears to trigger an unidentified mechanism, causing the telescope to continue slewing after the target has already passed.

"Wiggled": A combination of the severe tracking errors evident in "Trailed"

images with slight oscillations in declination; a mild form of the "weird blur" class. The form suggests small-amplitude, periodic jogging of the telescope in declination while stars are allowed to drift across the frame in right ascension.

"Weird Blur": Severe tracking errors in two dimensions result in star trails showing interesting structure along both columns and rows. These defects often suggest periodic jogging of the telescope position in both right ascension and declination in some fashion as the telescope vainly tries to acquire its target.

There are two additional, although considerably more rare, kinds of tracking errors which deserve separate treatment from the others. The first is the case of true "doubling", which is a phenomenon quite different in nature than the previously-termed "doubling". An example of this can be seen in Figure 13. True doubling is the appearance of exactly two star images, separated by some constant number of pixels, for each star in the imaged field. It is thought to result in a hysteresis effect in pointing which occurs as discontinuities in the polar axis ring pass over the RA rollers, causing a sudden jump in position. In this way a star image initially formed at pixel location (x, y) before the jump is re-imaged at $(x + C, y + D)$, where $\ell = \sqrt{C^2 + D^2}$ is the number of pixels represented in the jump. The flux recorded in each image is proportional to the amount of the integration time spent before and after the jump.
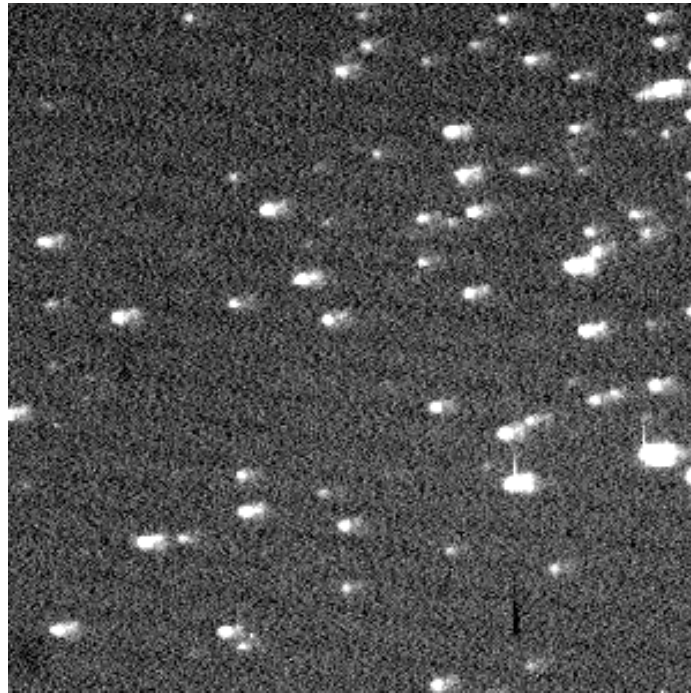
Fig. 13.— "True" doubling of star images in a subframe selected from the object image P51961FH. Note the duplicate image of each star on the frame located a few pixels away from the original at about the two o'clock position.

This hypothesis is borne out in testing of images which show this effect; pairs of star images have disparate flux values in the two images.

The second unusual case is dubbed "vertical tripling" (see Figure 14). It is characterized by three images of each object on the frame, arranged roughly along the columns of the CCD, with a slight offset across two or three columns. The cause of this effect is thought to be related to the case of "true doubling" but instead involving the declination ring of the telescope.

The last effect noted in some images causing them to be rejected from the data set differs entirely from those noted so far. A small quantity of images contain no
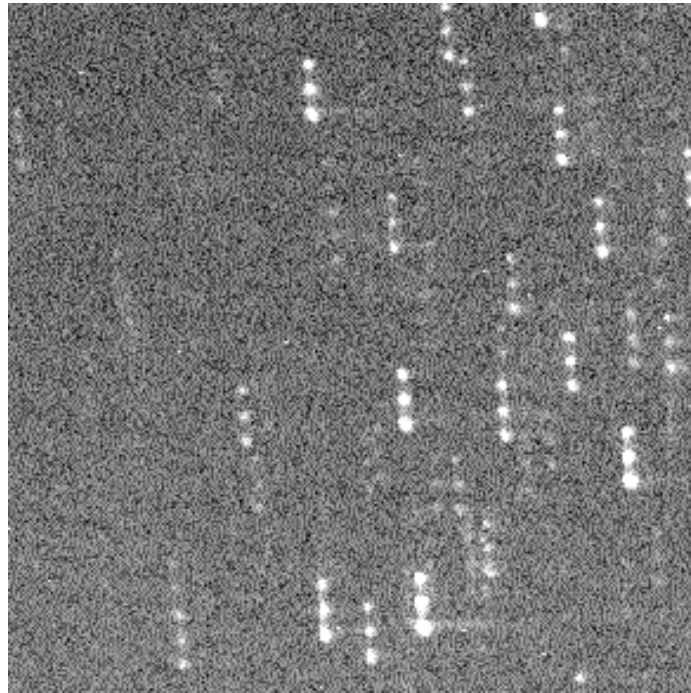
Fig. 14.— The tracking error known as "vertical tripling" in a subsection of the object frame P51991EE, taken on 22 March 2001.

data whatsoever, despite being created by the camera software. When displayed in

XImtool, these images show uniform pixel values of zero across the entire frame. This

effect is not indicative of a mechanical shutter failure, as such a failure would still

result in dark current remaining in the ensuing normal, 60 s integration. Rather, the

computer command to start an integration appears to be ignored, and the camera

returns a null image which is saved as the expected next file name in the object data

series.

One significant factor common to nearly all of these errors is that the camera

continues an integration even when the telescope is slewing. That is, an integration

proceeds whether or not the telescope has properly acquired its target and is tracking normally. Consequently, any movement of the telescope after the nominal field acquisition time has ended is recorded as the integration proceeds. This scenario is sufficient to explain nearly all the tracking errors noted in the aforementioned list.

A simple solution to this problem lies in software; before the command to begin an integration is issued to the camera, a check should be performed that the telescope has in fact acquired its target,is fixed on a single position and tracks properly. Failure to acquire the target can, in principle, result in the telescope control software entering an infinite loop in which the difference between the perceived and actual positions of the telescope never decreases and the command to begin integration is never issued. This may in fact be happening in the cases considered above, but the loop is cancelled by the issuing of the next ATIS command to move the telescope. Such a loop condition would require user intervention to "home" the telescope back to a known position again and re-initialize its coordinate system before acquiring the target again and proceeding to integrate. Seeing as how user intervention defeats the purpose of an automated telescope, the details of this problem demand careful consideration.

SciTech makes the following claims regarding the accuracy of its tracking scheme in its sales literature[6]:

---

[6]`http://www.scitechastro.com/starhom4.html`

"Tracks object Sidereal Rate open-loop within +/- 0.5 arc sec in Right

Ascension and Declination per 5 minutes. Tracking jitter less than 0.3

arc sec (rms) in Right Ascension and Declination."

While perhaps it hopes to achieve these tolerances in further commercial versions of telescopes based on the GNAT prototype, these values are very definitely *not* reproducible with any consistency in the GNAT prototype telescope. This conclusion is borne out by the data, which provide ancillary information about telescope parameters such as tracking accuracy. In Section 6.2.3 the method developed to handle the registration and co-addition of GNAT image sets is discussed; this process involves calculating the x and y pixel shifts required for registration with respect to a reference image.

By subtracting the values of the pixel shifts applied to successive images in a set, the tracking drift from one frame to the next can be determined; the drift is *significantly* greater than the 0.3″ tolerance claimed by SciTech. These results are shown in Figure 15, where the drift in y (declination) is plotted versus the drift in x (right ascension); note that the plate scale for the current configuration of the telescope is 1.82″ per pixel. Grid lines have been added at 1-pixel intervals to show how evidently wide the drift is as projected onto a grid representing the array detector elements themselves. In fairness, it can be seen clearly from the figure that in most cases the drift is no more than a pixel or two from frame to frame, though this nevertheless
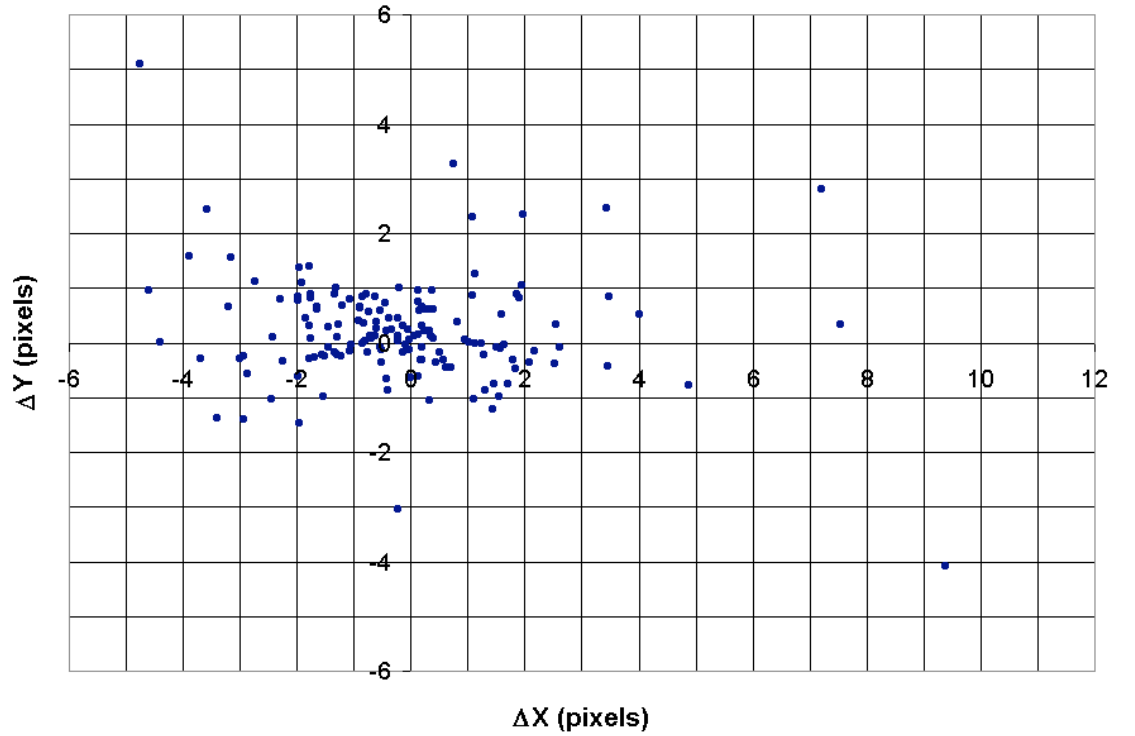
Fig. 15.— Frame-to-frame positional drift exhibited by the GNAT telescope.

amounts to a few arcseconds. A significant number of the points, however, lie beyond about three pixels, corresponding to a drift of nearly 6″ over a mere 60 seconds of integration time, plus the few seconds required for readout and target re-acquisition. Anecdotal observations of some frames are noted in which the drift is far more serious – measured in *dozens* of pixels – resulting in their complete rejection from the registration and co-addition process. Their rejection is not merely a matter of convenience, but rather of necessity: pixel shifts beyond the bounds of Figure 15 generally cause a failure of the registration fitting function to converge, and prevent image co-addition altogether. Since each image in a set rejected for drift errors results in progressively

larger error bars on the resulting photometry, the need to minimize the effect of these positional and tracking issues is rather clear if image coadding to increase S/N is to be routinely used.

There are several possible means of correcting the tracking issues that could be implemented with varying degrees of cost and required service time if SciTech is to be accepted as the vendor for the entire GNAT fleet. These are:

1. **Complete replacement of the telescope mount altogether**.
    While nearly assuring a solution to the problem, this most drastic step is also the most costly option.

2. **Purchase and installation of a working autoguider**, either the off-axis variety or in the form of a separate camera and guide telescope riding "piggyback" on the GNAT instrument. This solution was preferred by SciTech, but it was unable to furnish a working autoguider. The advantage of an autoguider, besides its relatively low cost, is essentially real-time guiding corrections based on continuous observations of a guide star, rather than the "mapping" method, as implemented by SciTech, described previously, which relies on a pre-defined correction sequence. Mapping does not take into account the continuous, though slight, deformation of the polar axis ring as the telescope moves throughout a night, or the gradual mechanical wear on the ring which would require frequent

refinement updates to the mapping corrections. An autoguider would also provide the fringe benefit of real-time monitoring of the seeing at the GNAT site by automatically measuring stellar profiles imaged on the autoguider chip and computing the seeing on-the-fly; see Section 8.5 for a discussion of the impact of seeing on GNAT photometric precision.

3. **Complete re-machining of the polar axis ring**. This would be a short-term fix only, as it, too, does not account for long-term wear which deforms it from its intended shape.

Despite the high cost involved, the complete replacement of the telescope mount is endorsed as the most effective solution to the tracking problem.

5.3.4.   Focus drift

SciTech provided an autofocuser with the telescope which has proven to be problematic from the start; GNAT abandoned its use early on when the trouble became evident. The use of autofocusers in general has become quite routine, even with smaller telescopes, primarily as a matter of convenience; in the case of an automated telescope, reliable autofocusing is critical to achieving science objectives. Focus drift due to mechanical strain on the telescope, diurnal thermal cycling and other factors presents a substantial challenge to the execution of an automated observing program,

but a reliable autofocuser can readily solve this problem.

The telescope focus is stable over very short runs, but over long periods of time this focus stability is unpredictable. Drift can ensue without warning and render images useless within minutes to hours after beginning an observing night. The observations of MJD 51992 (UT 23 March 2001) provide an excellent example of this. The night began with the first observations of M67 at 0001 UT; by 0118, focus drift had begun, initially manifested by stellar profiles with slowly increasing FHWMs. To the casual observer, this merely appears to be the effect of increasingly bad seeing, causing the profiles to "smear out" over a larger number of pixels. By 0240 UT, the focus had drifted enough to cause star images to take on the "doughnut" shape indicative of an out of focus image, as the shadow of the secondary mirror is resolved against the illuminated primary. The image in Figure 16 shows this effect very clearly. Of the 192 images of M67 obtained on the night of MJD 51992, 139 were rejected due to being too far out of focus to be usable, for a loss of 72% of the data taken on one night.

A small focus drift (e.g., that noticed between 0118 and 0240 UT on this particular night) is technically acceptable, although it results in oversampling of the stellar profiles by the CCD. These drifts can be treated as if they were simply conditions of bad seeing, provided the FHWMs of the profiles are not so large that adjacent stars' profiles overlap; this type of overlap causes errors in the determination of stellar PSFs
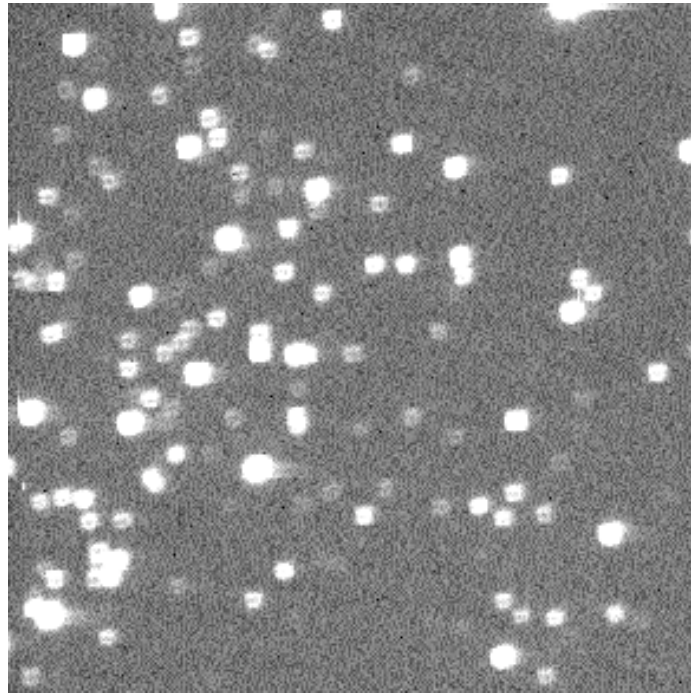
Fig. 16.— The practical effect of focus drift: out of focus star images in the object frame P51992FC, taken on the night of 23 March 2001.

and thus renders them useless for photometric purposes. Stars so out of focus that they take on the "doughnut" pattern cause fatal errors in automated PSF determination and must be rejected outright. The need for visual inspection of all raw data obtained with the GNAT prototype is reinforced by these conclusions, as for now a trained eye is required to differentiate useful out of focus images from those which are not useful and require rejection.

5.3.5.   Flat fielding concerns

The reliability of photometry results from any detector is strongly influenced by the quality of calibrations applied to the raw images the detector produces, in addition to the "built-in" characteristics of CCDs already considered. This section, and the one which follows, speak directly to calibration irregularities peculiar to the SITe detector in operational use on the GNAT telescope as of late 2000 and early 2001. Flat field images used the twilight sky as a source of illumination; it is the choice of this type of flat which drives the comments about flats made here. Two perceived defects in twilight sky flats taken with GNAT are discussed here in relation to their effects on processed object images after flat field division: 1) cosmetic defects and, 2) a changing illumination function.

Figure 17 shows a typical "average" (i.e., median-combined result of several individual flats) flat field image, composed of the median of six individual 0.1 s images taken on the night of 30 January 2001. Combining of the images was done with the IRAF task `flatcombine` in the noao.imred.ccdred package, with the "median" as the type of the combining operation (see section 6.2.1 for a further discussion of flat fielding parameters). The usual assortment of cosmetic defects are seen on this frame. Note, however, the four objects marked with circles; each represents a major defect either at or below the detector surface. The rightmost three have been identified as charge traps, resulting from imperfections in the manufacturing of the detector, which
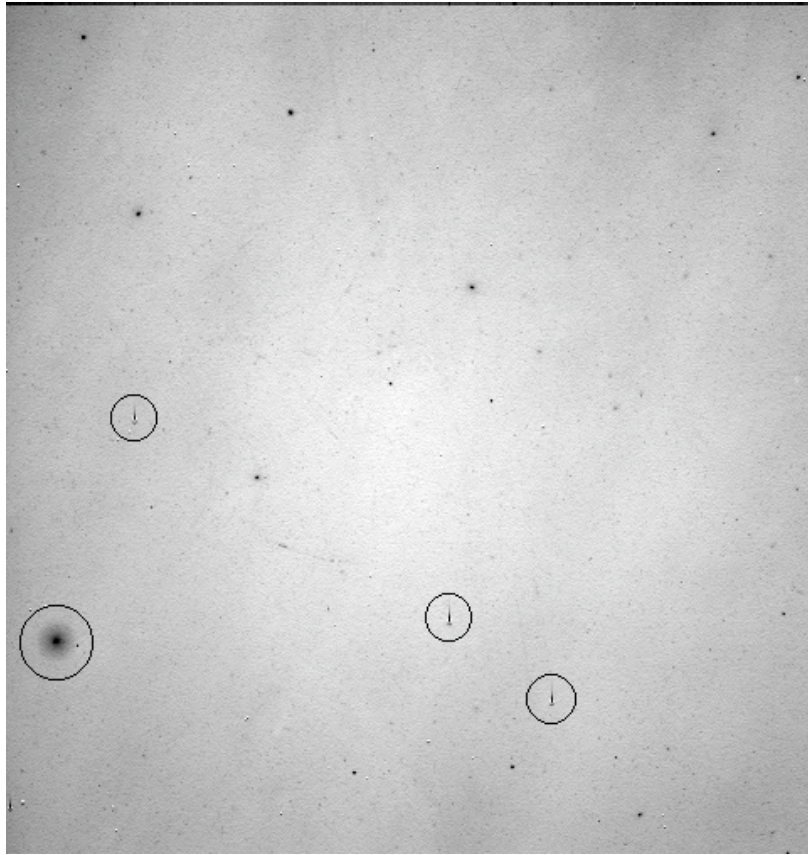
Fig. 17.— A typical flat field image produced by the SITe TK512 detector at evening twilight on 30 January 2001. Circles have been drawn around features germane to the discussion in the main text.

cause a loss of charge transfer efficiency during readout of the chip by "trapping" electrons from other pixels as they pass by. There is evidence of this phenomenon in the form of "spikes" along the columns identified with the center of certain stars on the frame. When these columns are compared closely with the flat field images, these columns are seen to coincide with the positions of the traps. Due to frequent, large frame-to-frame drifts in telescope position among images taken during a given night as discussed in the previous section, this phenomenon tends to affect different stars

in a given field throughout the night. The effect these traps have on the photometric

precision is examined in Section 8.7.

The fourth circled feature, near the left edge of the image, represents the largest

and most obvious of a class of defects scattered across the frame. These curious spots

are not removed from object images upon flat-field division. Figure 18 shows a line
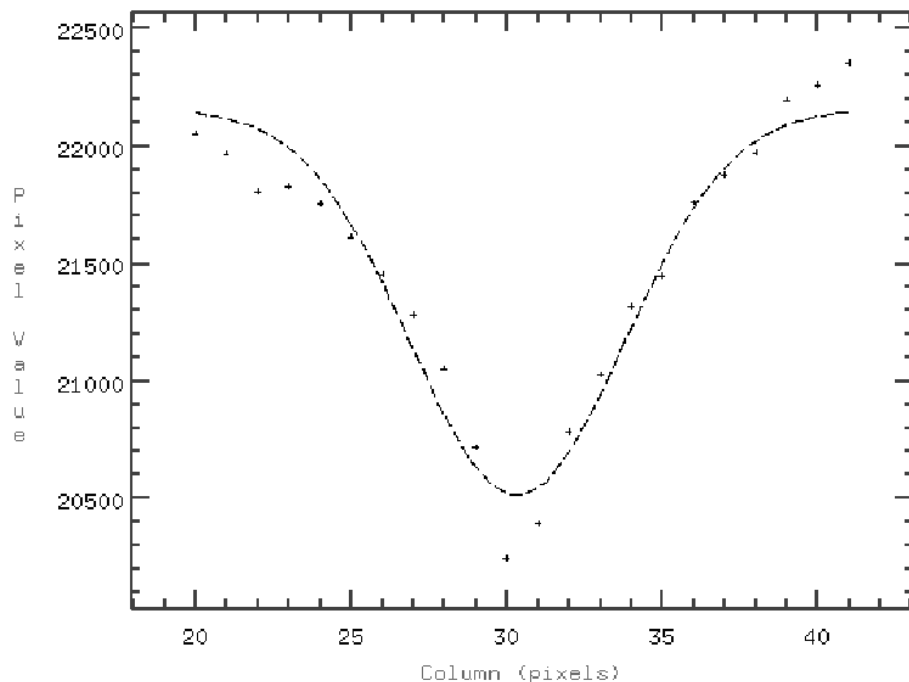
Fig. 18.— Line profile plot of the largest dust spot observed on the GNAT detector
surface with an overplotted Gaussian fit line.

plot taken through the center of the feature on the average flat from 25 January 2001.

The plot contains data from lines 125-129 on the image, and the IRAF task `imexamine`

was used to fit and overplot a Gaussian. The fit is clearly good, indicating what

appears to be diffraction from a roughly spherical particle with a circular profile. This

feature is, however, known to be a flaw in the antireflection coating on the illuminated side of the detector that causes some specular reflection at that particular point.

The other dark spots are believed to be dust particles, present *at the surface of the detector* , whose shadows appear in the flat field images. These are not the classic "dust doughnuts" traditionally observed on flats, caused by dust particles adhering to the outer window of the camera. Rather, these particles were sealed into the chamber containing the detector and thus are not easily removed without endangering the chip itself. Fortunately, they appear to remain fixed over time, despite repeated changes in the orientation of the camera with respect to the ground. These spots, however, are not removed upon flat field division of object images and thus remain on those frames; their contribution to decreased photometric precision is discussed in Section 8.8.

The stability of the flats taken with the system is an issue of particular interest as it serves as a probe of the mechanical systems of the telescope in addition to the camera and detector. In the case of twilight sky flats, the illuminated surface is effectively at infinity and yields an illumination function that takes into account the entire light path of the telescope from top end to detector plane. This pattern of illumination should not change significantly over a period of days to months due to flexure of components in the telescope or camera. In an earlier analysis by Taylor et al. (1999), the stability of flat fields on a night-to-night basis was measured by dividing

the master flat from one night by that of the next; any change will be manifested by pixel values in the image departing from unity be more than the expected noise. Taylor found a variation of "at most 0.5%" with this method and give a histogram of pixel values in the resulting image in their Figure 3. This procedure was repeated, keeping in mind the need to minimize the influence of illumination sources external to the telescope other than the solar illumination of the twilight sky. To this end the nights of MJD 51961 and 51962 were selected to divide flats from, since the interference due to moonlight was minimal on these two nights (see Table 3).

A histogram of pixel values in the resulting image after dividing master flats for these two nights is shown in Figure 19. The values are distributed in a nearly perfectly Gaussian, as Taylor found in the earlier analysis. The reason for the histogram not being centered at the expected value of unity is due to slightly different exposure densities for the component flats used in its production. Because of a very slightly longer integration time, the pixel values in the flat for MJD 51961 are a few percent higher than those of the following night. For component flats of identical density, the value is expected to fall at a mean of one and thus unusual behavior of the system accounting for the difference is not suspected.

Flats generated in this fashion are acceptably stable over the lengths of time considered important for time-series analysis of GNAT photometry program data. Long-term shifts in the quality of flattened images made with this camera are not
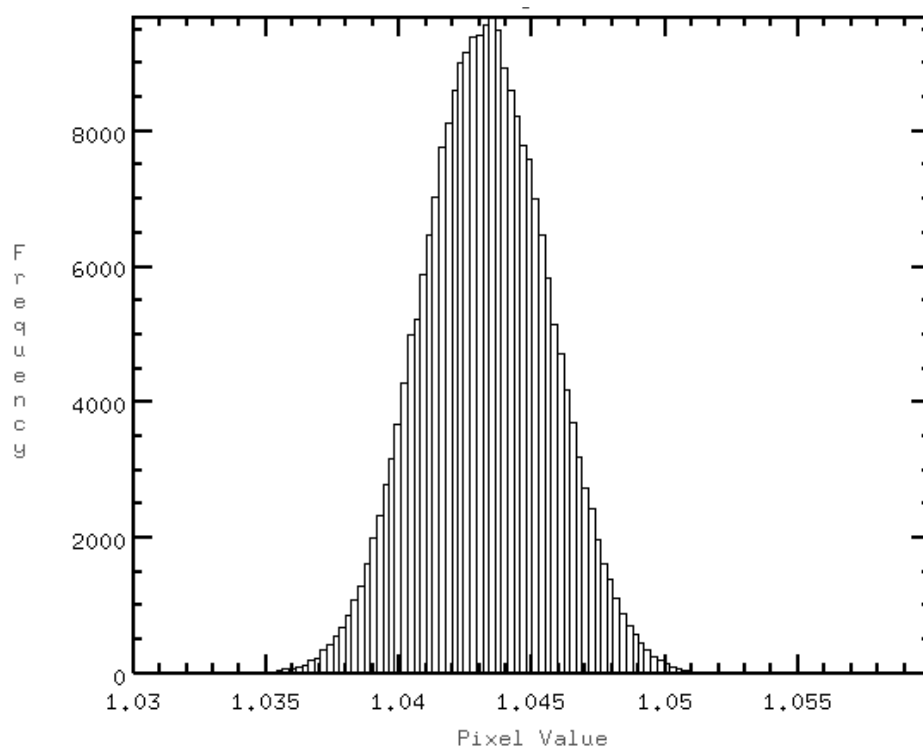
Fig. 19.— Histogram of pixel values in the image resulting from division of the master flat from 2001 February 21 by that of February 22.

anticipated.

5.3.6.   Noise structure in calibration and object frames

In addition to the other stated disorders afflicting the operation of the current (winter 2000/1) SITe TK512 detector in the GNAT prototype, a persistent noise structure in all object frames taken with this detector is noted, as well as in some calibration frames. This structure has the character of a "stripe" pattern with a spatial frequency of approximately 20 pixels on the detector, and an amplitude ranging

between approximately 6% and 9% above the mean level of the background in any given object image. The amplitude of this structure and its spatial variability over time scales of seconds to minutes strongly suggests the presence of RF interference in the camera electronics or transmission lines. The spatial frequency of the noise in the images seems to rule out pure 60Hz noise alone as the source of the pattern, but other harmonics may be at fault.

A similar structure is evident in the calibration frames, specifically, darks and bias frames. A typical bias frame taken with the detector is shown in Figure 20. Due
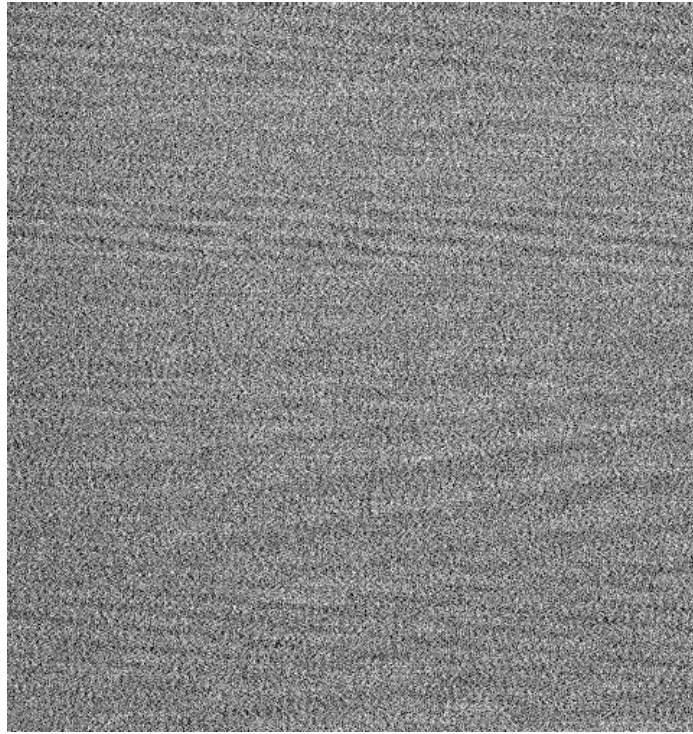
Fig. 20.— A typical bias frame produced by the SITe TK512 detector on 31 January 2001 showing very clear structure across the image.

to the variability of this pattern over time, it is not possible to remove its contribution

through subtraction of calibration frames (see Section 6.2.1). The contribution of this noise to the photometric error is discussed in Section 8.1.

5.3.7. Background noise

Finally, an examination of the characteristics of the sky background in the object images was made to understand its behavior and stability over the length of the time series on M67 collected in the spring of 2001.

Statistical information on the background was gathered in order to evaluate its compatibility with the noise models assumed in Section 2. The noise turned out to be superficially Gaussian, as expected. Figure 21 shows a histogram of values within a "blank sky" portion of the GNAT object image P51942DY, selected to exclude stars and representative of data obtained with the SciTech telescope in general. The section encompassed a sample of 2,301 pixels with a mean value of 75.29 counts and σ=4.162 counts. If this noise was Poisson-distributed, it would behave like $\sigma = \sqrt{\overline{N}}$; clearly this is not the case. This discrepancy has a significant effect on the interpretation of photometry results generated by this telescope and detector.

A possible explanation for the non-Poissonian nature of the background levels in the data was identified: variation in the background values over the course of a night not associated with external effects. Figure 22 shows the mean background value in
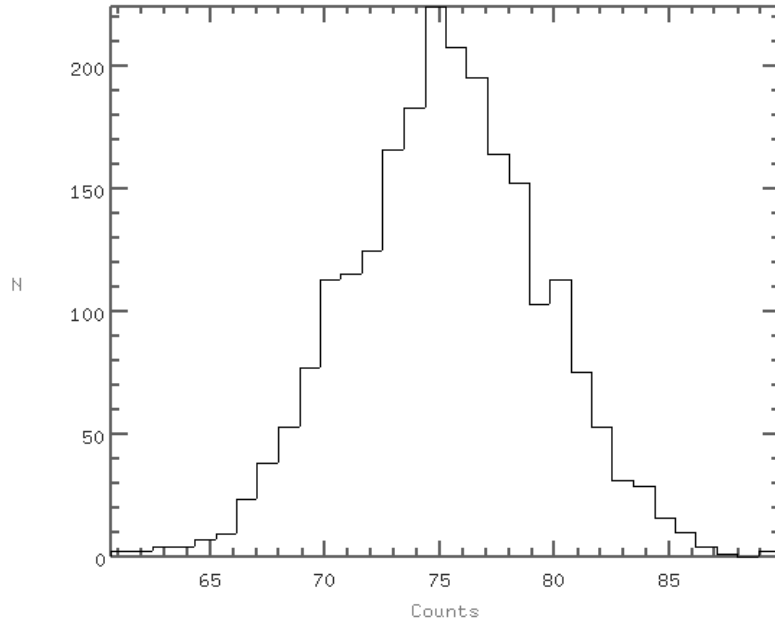
Fig.   21.— Histogram of values in the section [377:415,396:454] of object image P51942DY, taken on 2 February 2001.

a constant image section as a function of time. These mean values were determined after the images had been registered (see Section 6.2.3) such that the *same* area on the sky was being sampled in each case. The image section used was chosen in a "blank sky" portion of the M67 field, devoid of stars above the level of the background, such that the measurements were not contaminated with any flux from potentially variable stars. The reader can immediately see the problem in this plot: the "reverse J-curve" behavior of the background mean, starting with a high value at the beginning of a night, and dropping rapidly to finally achieve something of a stable equilibrium value as the night goes on. The value of σ for the same image section is nearly constant over the course of the night; what this implies is that the background starts out the
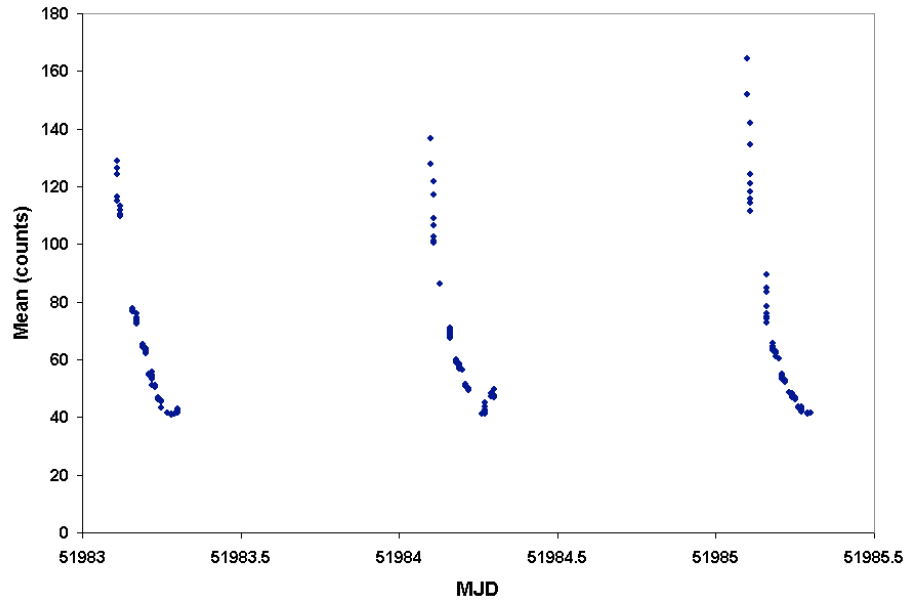
Fig. 22.— Changing mean values of the background in M67 images. Data are re-stricted to three nights here in order to show the structure of the change more clearly.

night decidedly non-Poissonian and gradually becomes more Poisson-distributed as

the night goes on. No elementary type of function has been found to satisfactorily fit

the curves in Figure 22 and such have little indication of the cause of the problem. The

tails are nearly exponential in their decay, but for the first approximately one hour of

each night's observing, the decay is much faster than exponential. Furthermore, the

shape of the decay changes nightly, making it impossible to model each night with

the same function. The curves bear only a superficial resemblance to each other. And

finally, on some nights the background defies predictability entirely. Figure 23 shows

a particularly notable example of this; the background mean for the night of MJD

51960 follows no pattern, whereas the variation of the background on the subsequent

night is considerably more regular.
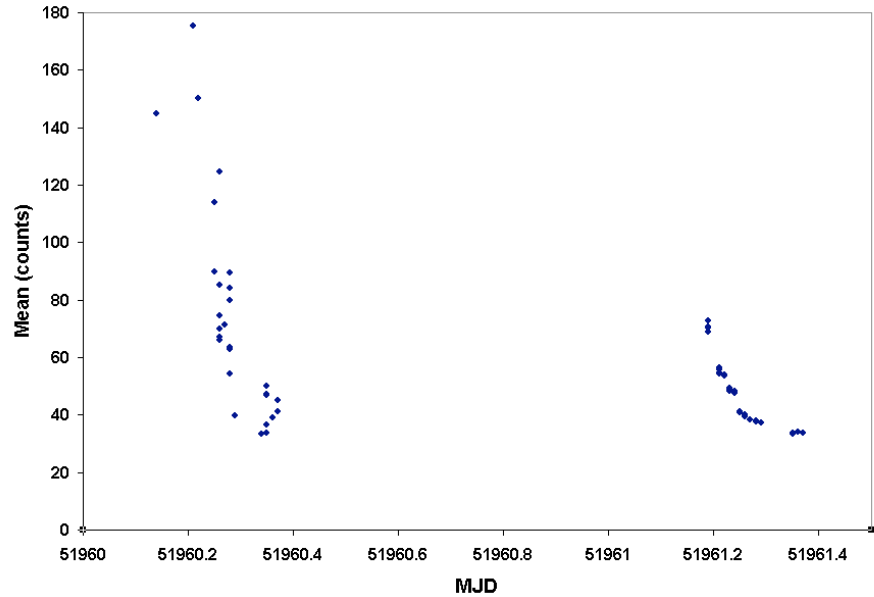
Fig. 23.— Mean background values versus MJD for the nights of 51960 and 51961. Note the significant scatter of points on 51960 as compared to the much greater regularity of values on the following night.

Assigning cause for this behavior is difficult. There are certain sources of background not directly associated with the telescope or detector which can cause changing background values, including moonlight illumination of the sky and changing sky transparency. The consistent behavior from night to night of the background over the course of a given night seems to rule such sources out; there is no dependence on airmass at the time of observation or percent illumination of the Moon to support the conclusion of an external source. Some internal sources have also been ruled out, such as unregulated behavior of the detector temperature, which would contribute a changing degree of thermal noise throughout a night. However, without fail, it is an effect that causes the background mean to begin each observing night at a high value

and decrease over an interval of hours to a lower value. It is this phenomenon which appears to have the most significant effect on the attainable photometric precision of this system.

In summary of the data quality presented by the GNAT prototype, the informality of Massey & Jacoby (1992) in their review article "CCD Data: The Good, The Bad, and The Ugly" is adopted to describe the GNAT telescope data as "ugly". That is to say, the images are *pretty* linear, with the exception of the serious cosmetic defects described previously that are not removed in calibrations, the noise is *close* to Gaussian, and the data are non-flat. In some regard, particularly with respect to the persistent defects, the data are at some level "bad" and require long-term solutions to the problems outlined here if the quality of the data products from the GNAT prototype are to approach the level required by the overall science objectives.

Table 2.   Occurrence of image defect types in 622 images of GNAT data from JD51935-51960

Defect Type	N	Percentage
"Badly Trailed"	73	11.7
"Slight Blur"	72	11.6
"Doubled"	21	3.4
"Weird Blur"	9	1.4
"Wiggled"	3	0.5
"Artifacts"	1	0.2
Total Rejected	179	28.7

6. Data Acquisition And Reductions

In this section the pipeline of the data reduction is described. This discussion includes the methods of obtaining the data, packaging them for transport, and reduction at the CSU node of the GNAT project. The photometry method investigated for constructing light curves of the program stars in M67 is also discussed.

6.1. Acquisition procedure and data storage/archival

Images from the telescope are named according to the type of image, the Modified Julian Date (the heliocentric Julian date - 2440000, and where each falls in the series of data taken on a given night in the format (type)(MJD) (sequence). Following a standard ATIS protocol, images carry a prefix of "P" for object images, "B" for biases, "D" for darks and "F" for flats. The sequence content of the image suffix is a two-letter designation beginning with AA and proceeding AB, AC, etc. The sequence counter is reset for each image type among the calibrations and object images obtained each night.

The raw data are written to CD-R for archival purposes and have been provided to the CSU contingent of the GNAT project on copies of these CDs. The images were reduced on a Pentium II-based PC (gnat1.colostate.edu) running Mandrake Linux 7.2 and PC-IRAF v2.11.3. Each raw GNAT frame is approximately 581kB

in size and gnat1 has 4.2GB of disk space available for data storage; this allows for approximately 5 nights' worth of data on average to be stored and manipulated at any time. To effectively manage this amount of space, data are reduced as received and the calibrated images written back to CD-R for on-site storage. In this fashion users can easily restore the archived, reduced images for manipulation.

The results reported here have been extracted from 19 nights of data provided to the CSU node of the GNAT project by Eric Craine, covering the dates JD 51935-52029. There is no large-scale contiguity of the nights, save for a handful in March 2001, which were characterized as among the "best" in terms of data quality and temporal cadence. Details of these nights are summarized in Table 3.

6.2.   Standard CCD reductions

6.2.1.   Calibrations

Calibrations of the raw images proceeded in the usual manner under the semi-automated convention of the IRAF task `ccdproc`[7]; for a complete, step-by-step reduction protocol, please see Appendix A. After examination of a number of calibration images, a decision was made to deliberately *not* bias or dark correct the object im-

---

[7]For an introduction to CCD image reduction practices, see the document "A User's Guide to CCD Reductions with IRAF" by Philip Massey available from the IRAF website at `http://iraf.noao.edu`.

Table 3.   Summary of observing nights, spring 2001

MJD	UT Date	Lunar phase (%)
51935	2001 January 26	6.4
51940	2001 January 31	46.1
51941	2001 February 1	56.7
51942	2001 February 2	67.4
51959	2001 February 19	8.0
51960	2001 February 20	3.8
51961	2001 February 21	1.1
51962	2001 February 22	0.1
51983	2001 March 15	54.9
51984	2001 March 16	45.2
51985	2001 March 17	35.9
51986	2001 March 18	27.2
51987	2001 March 19	19.4
51988	2001 March 20	12.7
51991	2001 March 23	0.8
51992	2001 March 24	0.3
51994	2001 March 26	5.0
51995	2001 March 27	10.4
51996	2001 March 28	17.6
51997	2001 March 29	26.4
51998	2001 March 30	36.5
51999	2001 March 31	47.5
52012	2001 April 13	62.2
52028[1]	2001 April 29	44.6
52029[1]	2001 April 30	56.1

Note. — [1] These two nights were discarded because of severe interference from the nearby Moon.

ages. This decision was based on the recurrent appearance of structure (see Section 5.3.6) within the biases and darks which changed in spatial distribution and frequency over time. If these structures were invariant with time, they would be easily removed from the object images by biasing and dark correction, but their variability prevented this. Keeping these steps in the calibration process would contribute the error in the biases and darks to the object images, and in the interest of maximizing the resultant photometric precision in the object images, they were rejected. Such a policy is supported by certain factors native to this instrument; namely, low dark current due to short integrations and a low bias setting. The rejection of darks and biases would not be appropriate if targets much fainter than the brighter stars in M67 were being observed, for these noise sources contribute more to the S/N of an observation as N_* decreases (see Equation 3).

Additional characteristics of these calibration images allow biases and darks to be neglected without adversely affecting the object images. Figure 24 shows the histograms of both average dark and bias frames; note the shapes in good agreement with the expected Gaussian distributions, composed of single peaks with no secondary maxima. These darks and biases are characteristically "good", according to criteria in Howell (2000) and free of defects which calibration is designed to correct for. The large-scale spatial structure in these images, however, is not accounted for in these histograms; thus any spatial frequencies in the noise will be propagated to
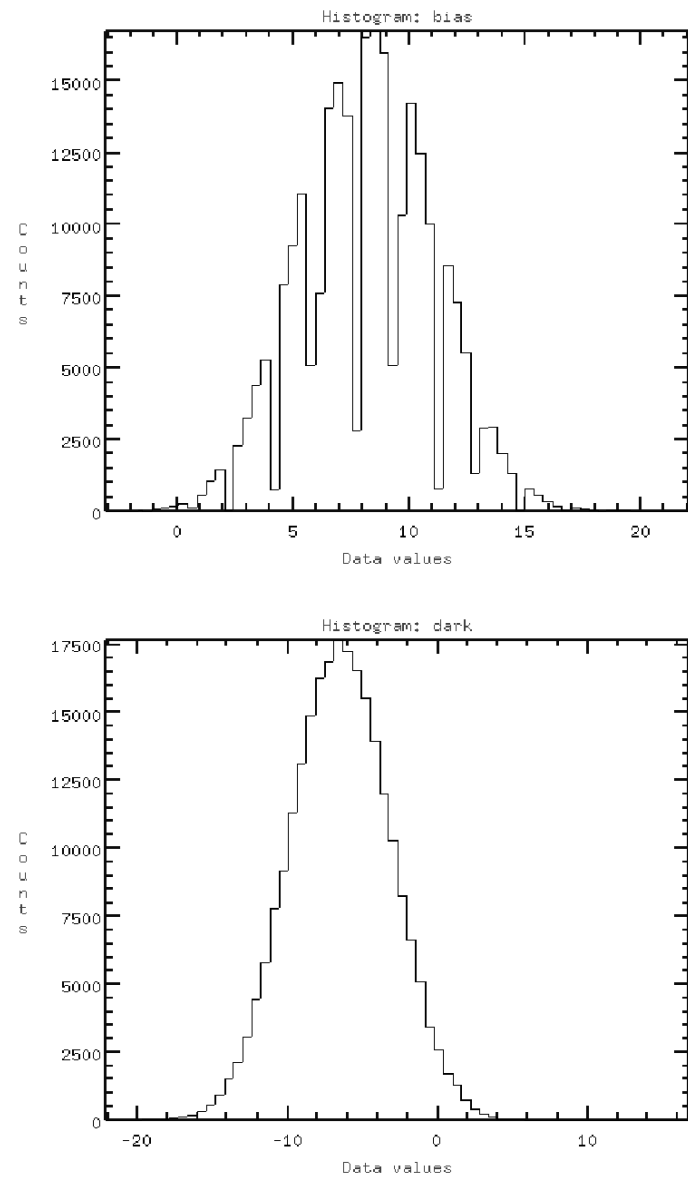
Fig. 24.— Histogram showing the frequency of data values within an average bias image (upper) and an average dark frame (lower) made on 25 January 2001.

object frames when calibrations are performed. As a side note, the width of the bias histogram provides an independent assessment of the read noise of the detector. Howell (2000) gives the relation between the width of the histogram, the gain and read noise as

$$\sigma_{ADU} = \frac{ReadNoise}{Gain}. \tag{10}$$

The 2σ width of the histogram is approximately 8 counts; since the GNAT detector was photon counting (i.e., gain = 1 electron per ADU), the read noise estimate is 8 electrons per pixel. This value turns out to be much smaller than the nominal value of 13 used in the reductions thus far. While the measured value is considered "good" for a modern, low-noise detector, it has implications for the noise in the final product of any image coadding done with GNAT images (see Section 6.2.3 for further discussion).

There are additional concerns beyond the noise pattern noted earlier that appear to be 'hardwired' into the detector and thus non-removable with calibrations. Figure 25 shows column plots through the "overscan" region (image section [28:49,7:512]) of two images taken on MJD 51986. This region, present on all frames, is composed of 21 rows of "pseudo-pixels" generated by sending additional clock cycles to the CCD after the on-object integration has finished but before readout and is used in the determination of the bias level in the absence of separate bias frames being taken (Howell 2000). Since this represents the pedestal level of the CCD before object
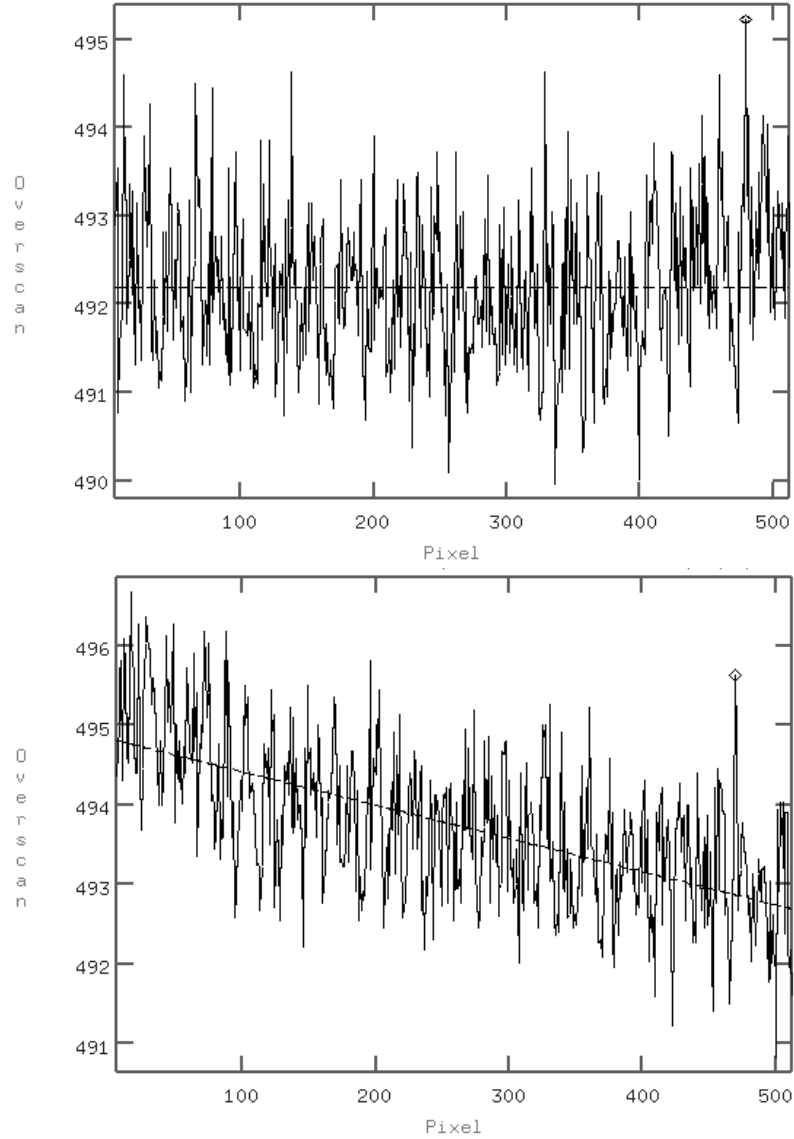
Fig. 25.— Column plots through two images taken on MJD 51986: the overscan regions of flat field F51986AB (top) and the object image P51986AZ (below). Dashed horizontal and diagonal lines represent model fits made using `ccdproc`.

signal is applied, overall this pedestal will look largely "flat" across the chip; this is

particularly important because of the decision to omit biasing from data reductions

to reduce the noise present in calibrated object images. Although it is not unusual

for some chips to exhibit gradients of ~ 1 ADU from one end to the other, the fig-
ure shows a nearly linear gradient of approximately 4 ADU, with the noise pattern
observed in the biases superimposed. Since object images were not bias subtracted,
it is only natural to assume that this gradient is present "under" the object images
and not being calibrated out. At 4 ADU, however, we a structure is being considered
whose amplitude is well below background and stellar pixel values and whose spatial
extent is far larger than either the stellar profiles or the photometry apertures. Thus
this gradient does not contribute significantly to the precision of stellar photometry
beyond the regime of Poisson noise. While a noticeable gradient in the object image
overscans exists, the upper panel in the figure shows that flat field overscans tend
to be rather uniform. There is no ready explanation for the difference in the slope
of the overscan gradient which depends on image type, but note that it is consis-
tent throughout the data set. This gradient is fit with a first-order polynomial in
reductions and removed from the data.

6.2.2.   Updating image header parameters

In order to properly calibrate raw object images produced by the GNAT proto-
type, and later to perform photometry on those images, certain information must be
added to the header file associated with each image. This information, typically con-
sisting of telescope/detector parameters, is passed to IRAF tasks requiring it at the

time of their execution. Long-range plans for the use of the GNAT telescope include updating the camera control software to automatically incorporate these parameters into the FITS image header upon image file creation at the telescope, but for now they must be manually added to all image files as a step in the reduction process. The parameters, and their nominal values, are given in Table 3.

Both photometry routines investigated required values for a variety of image header parameters not added by the image acquisition software. The determination of the "ST" or sidereal time parameter is done according to the Julian Date (JD) of observation. In all calculations involving the date, the MJD is used. Any decimal part of the MJD is kept and designated the Fractional Julian Date (FJD). The local sidereal time matches the Universal Time (UT) at the moment of the autumnal equinox; thus, calculation of the ST depends on what fraction of a sidereal year has passed since the most recent autumnal equinox. ST has the form

$$ST = UT + \frac{(JD - 51808) \cdot 4}{60} - 7. \tag{11}$$

In nearly every case reported here, the 2000 equinox (MJD=51808) is referred to. The number of days since the 2000 equinox[8] is computed, and the result multiplied by 4 to obtain the difference between ST and UT, accounting for the approximately

---

[8]In earlier or later years, correction of this value must be made to the nearest autumnal equinox date to avoid the accumulation of errors in calculating ST.

4 minute difference in the lengths of the sidereal and mean solar days. A conversion to hours is made by dividing by $60\frac{min}{hr}$. Finally, 7 hours are subtracted to account for the time zone difference between MST and UT.

ST, UT, the date of observations parameter DATE-OBS and the observatory location parameter OBSERVAT must be provided in order for IRAF to automatically determine the airmass at the time and location of observation. This is accomplished via the `setairmass` task in the ASTUTIL package. `setairmass` calculates the hour angle of the object knowing the object RA and the current local ST. The hour angle correlates directly with the airmass according to the secant of the zenithal angle at the moment of observation; corrections to this value are then applied based on the altitude of the observing site, which IRAF stores in tables for pre-defined observatory sites. No site is currently defined for the location of the GNAT prototype, so the site entry for Kitt Peak National Observatory, located nearby, is used. Note that this introduces a slight amount of error into the calculation of the AIRMASS parameter due principally to the difference in elevation between the two sites ($\sim$1500m)

Two CL scripts have been written to streamline the process of updating the image headers. These scripts are simple sequences of IRAF commands which can be performed on either IRAF or FITS format images. The first script, called `addheaderparams.cl` adds basic header keywords for detector parameters and image types:

```
# Convert from .FTS extension (which IRAF can't cope with) to
```

```
# .fits (which it can)


rename .FTS .fits *.FTS


# Change data pixel type from "short" to "real"


chpixtype *.fits real


# Add various header parameters needed in later processing


hedit *.fits GAIN 1 add+ ver-

hedit *.fits RDNOISE 13 add+ ver-

hedit *.fits TRIMSEC [60:538,7:512] add+ ver-

hedit *.fits BIASSEC [28:49,7:512] add+ ver-


# Add the header parameter IMAGETYP which tells IRAF what kind

of file

# each image is (e.g., object, flat, etc.)


hedit B*.fits IMAGETYP zero add+ ver-

hedit F*.fits IMAGETYP flat add+ ver-

hedit P*.fits IMAGETYP object add+ ver-

hedit D*.fits IMAGETYP dark add+ ver-
```

Note that these are all fairly "generic" updates which do not require any information

specific to the data set from a particular night (e.g., the MJD, date, times, etc.)

Some parameters do not change with time; e.g., the overscan region size and limits

are always the same. For the purpose of calculating parameters such as the sidereal

time, as discussed previously, such information is required, and a separate script called

`hupdate.cl` has been written which requires the user to edit certain fields to provide

night-specific information:

```
# Change the designation of the Right Ascension parameter, which
was
# incorrectly added to the header by the camera control software.


hedit *.fits "RA" "(R.A.)" add+ ver-


# Change the format of the DATE-OBS parameter to a format IRAF
can deal
# with.  NOTE: change ''yyyy-mm-dd'' to the proper date below


hedit P*.fits "DATE-OBS" "yyyy-mm-dd"


# Add the epoch at the time of the observations.
```

```
# NOTE: change "yyyy" to the year at time of observation.


hedit P*.fits "EPOCH" "yyyy"


# Add a UT parameter indicating the Universal Time at the time
of
# observations based on the Julian Date and Fractional Julian
Date
# (JD.FJD) previously added to the header.
# NOTE: replace "-JD" in the expression below with the proper
5 digit
# expression for the Julian Date of observation


hedit P*.fits "UT" add+ ver- value="((JD.FJD)-JD)*24"


# Add a ST parameter indicating the Sidereal Time at the time
of
# observations based on the date of the most recent Autumnal Equinox.
# Replace JD as in the last step.


hedit P*.fits "ST" add+ ver- value="(UT)+((((JD-51808)*4)/60)-7)"


# (51808 is the JD for the equinox of 21 September 2000.  Update
```

```
for

# subsequent years with the correct JD.)


# Add a header keyword for the location of the observatory


hedit P*.fits "OBSERVAT" "kpno" add+ ver-
```

As each of these scripts is run, the resulting changes to the image header are echoed to the screen. The order in which they are run is unimportant, as neither relies on parameters set previously by the other.

6.2.3.   Registration and co-addition of object frames

The integrations were deliberately kept short to minimize the effects of tracking errors as discussed in Section 5.3.3 with the additional benefit of minimizing dark current. However, this also tends to diminish the value of $N_\star$, which should be maximized to achieve the highest S/N possible. A standard technique in astronomy was used to work around this apparent problem: coadding a series of short-duration images to yield a single image of equivalent total integration time. While it does carry the disadvantage of adding the read noise from the multiple frames of equivalent total integration time, it is the only effective way found to deal with the tracking problem.

As of the most recent release of IRAF (v2.11.1), there is no single task yet available which allows the user to register and co-add a set of images. Rather, there exist a number of freestanding tasks which, run in a certain series, can produce the desired effect. A process was devised to meet this challenge; described schematically, it is to first locate the brightest stars on the first frame ("reference") in an image series, find the coordinates of their geometric centroids, calculate the pixel shifts in (x, y) required to register subsequent images to the reference, register the images using the calculated shifts and finally co-add the results.

As an example of how the images were registered and co-added, assume that 10 images exist in the range of image names P51935CV to P51935DE, taken on MJD 51935, and these images are to be combined into a single, 600 s effective integration frame. The first step is to compile an image list, consisting of a text file with one entry per line, each entry being the file name, using the task `sections`:

```
sections P51935C*.imh,P51935D*.imh > m67list
```

The user then opens this file in a text editor (e.g., the vi editor), and manually edits the contents of the list generated by `sections` to contain only those in the selected file name range. In the next step, stars must be located on the frame and their centroid coordinates determined in order to provide information for calculating the registration shifts. To find stars, the task `daofind` in the DAOPHOT package is

employed; the user begins by editing the parameter file for this task. By convention, the resulting coordinate output file is named in the format image.XX.coo, where XX represents the two-letter frame designation native to the ATIS system.

The star-locating task `daofind` has a series of parameters associated with its operation which must be explicitly specified by the user. "FWHM" is the full width at half maximum of the radial intensity profile of a given star on the image. Its value is determined by examining a few radial plots of stars on an object image (done by running `imexamine`, placing the cursor over a star, typing "r" and reading the FWHM as the last number given at the lower-right corner of the xgterm window); the FWHM is a parameter calculated by IRAF which appears in the display along with the radial profile. "sigma" is the standard deviation of the background in an image in counts, determined by the formula $\sigma = \sqrt{sp + r^2}$, where p=1 is the gain of the detector, r=8 is the read noise of the detector and s is the mean pixel value of the background. s was measured by running the IRAF task `implot` on section of an object image chosen specifically such that no stars are visible on the frame within the section; an "s" keystroke in the `implot` window echoes a series of statistics pertaining to the section to the command window, among which is the value of σ. An average value of σ=14.26 counts was calculated over several frames which was used in all subsequent instances of `daofind`. "datamin" is the minimum useful number of counts in an image, setting a threshold for acceptable pixels; it is nominally given by $s-3\sigma$, which

in this particular case gives a negative value. The value of "datamin" was forced to zero as a result. Finally, "psfrad" is the radius of the circle within which the Point Spread Function is defined. A value of approximately one-half the diameter (in pixels) of the largest star image on an object frame was selected, yielding psfrad=3.5 pixels. The choice of one-half the diameter was made in order to encompass all the flux from even the brighter stars when performing photometry.

After running `daofind` the user next extracts a two-column (x, y) coordinate list from the `daofind` output file via the IRAF task `fields`; the result is piped to a file generically called "coords":

```
fields image.XX.coo 1,2 > coords
```

This type of formatted ASCII file is required by the task `imcentroid`, used to determine the centroid coordinates of each object on the frame. IRAF uses "coords" as a rough guess approximation of locations of stars on the frame; `daofind` does not locate star centers with any appreciable geometric precision, resulting in a need for accurate star centroid determination. `imcentroid` takes the coordinate entries in "coords" and draws a box, of user-defined size, around each coordinate entry in which it expects to find the star. The user specifies two box sizes, "coarse" and "fine", for which values of 11 and 7 pixels, respectively, were adopted; these values, determined empirically, seemed to yield the most consistent centroid values. It iteratively narrows

the size of the fine box once it locates the star until the box just encompasses the star; it then uses geometric algorithms to locate the pixel value corresponding to the centroid of the star. In the final step, this pixel value is compared with the centroid for the same star in the "reference" image – the image to which the others in the set are to be registered. This routine is carried out for each star in the coordinate list and a mean shift for all stars on the frame is calculated. In this scheme, the user executes `imcentroid` with parameters input=(object frame list file), reference=(first image in series, used in `daofind`), and toleran=0. The last parameter is a pixel value for the "tolerance" of the fit, which was set to zero to assure absolute convergence of the fit; otherwise, positional error can accumulate rapidly if the software attempts to match stars which have drifted off the detector over the course of several integrations with those on the master frame. Box sizes can also be adjusted if needed in order to provide for some flexibility in which stars are identified such that the fits *do* actually converge.

The resulting output of `imcentroid` is echoed to the screen, which can also be piped to an output file with a redirect (">") command. For the purpose of extracting the pixel shifts to be applied to each individual image for registration, the user must delete the first few dozen lines of the output file, up to the section headed "#SHIFTS". The preamble to this file must be deleted, for in the next step when the task `fields` is applied to literally extract the pixel shifts as a two-column file,

the fitting information preceding "#SHIFTS" causes `fields` to quit prematurely. In practice, such a manual edit results in a generic file arbitrarily called "temp". The extraction is performed with the command string

```
fields temp 2,4 > shifts
```

where the output is directed into a file called "shifts". This file contains one line per image in the series being registered, each line consisting of two columns (x and y pixel shifts, respectively).

In order to distinguish registered images from their unshifted precursors, the name of each object image was changed after the registration shift has been applied to it. By convention, an underscore is placed in the file name between the MJD and the image sequence designation; e.g., P51935CV $\longrightarrow$ P51935_CV. Renaming is a consequence of applying pixel shifts to the images via the task `imshift`, which requires for execution both an input and output list of file names. Currently, editing of the input list to produce an output list with the slightly changed file names is done by hand, but with adequate effort at programming, in order to automate this process, one could envision streamlining the process by doing this list update automatically.

Finally, the user runs the task `imshift` with the proper input and output file name lists. The resulting images are now ready to be co-added, under the assumption that the registration just performed on the images will minimize any trailing of stars

in the finished image. To combine the images, the task `imarith` is used with the adding ("+") operation turned on. As written, `imarith` is evidently incapable of adding the contents of a list into a single image, so the frames must be added one at a time. For example, the first image in the set is added to the second, then the result is added to the third; this result is added to the fourth, and so on. In order to assure that the registration was properly implemented, the final step in the process is physical inspection of the co-added result. A contour plot of a few stars on the frame should show reasonably round profiles.

6.3.   Selection of targets

The nominal duty cycle of GNAT observations involves making ten one-minute integrations on each of two fields ("A" and "B") for a total cycle length of twenty minutes plus readout time. The context of GNAT fields "A" and "B" is shown in Figure 26 with respect to the map given by Eggen & Sandage (1964). Note the overlap between the two frames which guarantees that some of the stars in the dense central region are observed in all object frames, resulting in a very high cadence in the time-series observations of these stars.

A set of rules for selection of objects for photometry was developed with the goal of maximizing the temporal consistency of the time series and minimizing the photometric error of each program star. Objects falling within the outer 20% of the

Fig. 26.— Outlines of the two nominal GNAT observing fields in the central portion of M67 overlayed on Figure 1 from Eggen & Sandage (1964).
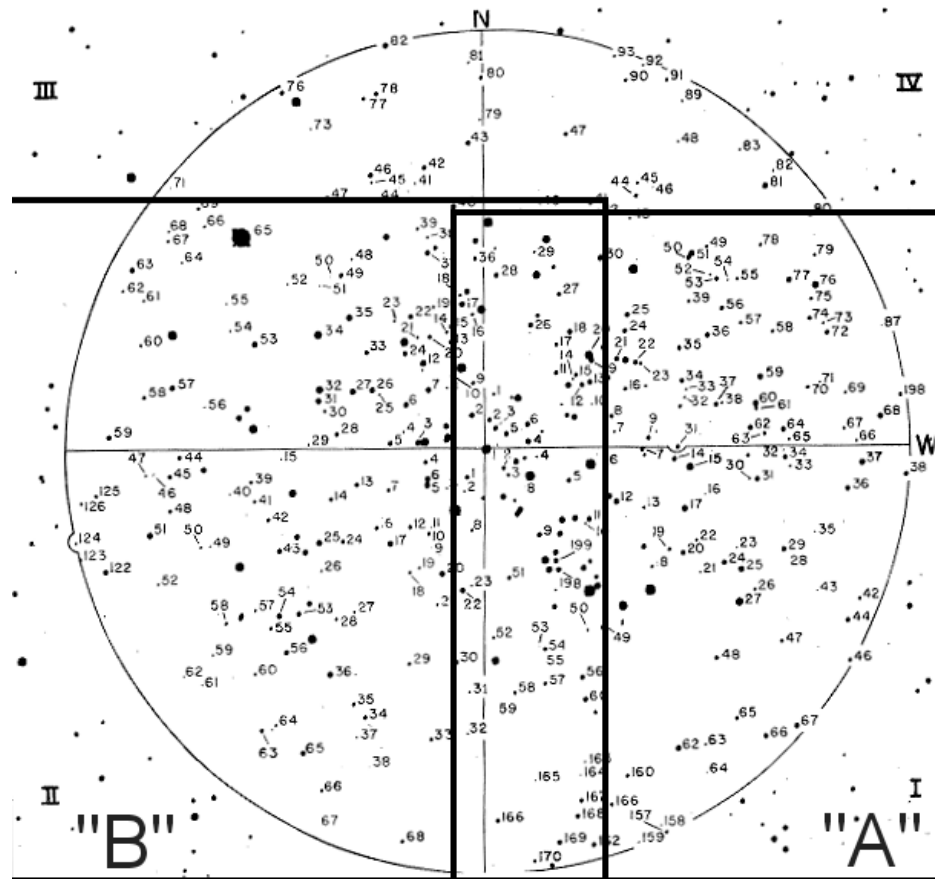
nominal boundary for each field were rejected because of their propensity to fall off the edge of the chip during even short integrations; this can be attributed to the tracking problems discussed earlier. Saturated stars were also eliminated outright on account of their inherently unreliable photometry. When working with coadded images, the "sigma clipping" pixel rejection algorithm in the IRAF tasks for combining images was used with the rejection threshold set at $\pm 3\sigma$; this typically removes all cosmic rays from the coadded result. In the case of single 60 s frames, a combination of

automated star identification (with `daofind`) and examination of selected images by hand was used to eliminate the inadvertent photometry of cosmic rays, hot pixels, etc. In some cases (e.g., testing of simple aperture photometry) targets were deliberately chosen by hand to prevent overlap of program objects with other field stars, but for the most part automatic detection was relied on to maximize efficiency. In the cases where `daofind`was used, the task's user-defined detection thresholds controlled selection of the stars.

6.4. Ensemble differential photometry

Once reduced object images are obtained and properly coadded, instrumental magnitudes must be obtained from them in order to build light curves for the observed stars. Simple aperture photometry is not very appropriate in this case, as M67 meets the qualification for a "crowded" field, in which many stars are close enough to their neighbors such that at least the sky annulus for a given photometric observation would overlap the profile of a neighboring star. Several photometry methods for use with crowded field data were evaluated. Point Spread Function (PSF) Photometry was developed in response to the need to perform photometry in such fields; by empirically modelling the PSF of field stars, their neighbors can be reliably "subtracted" momentarily from the frame to allow for standard aperture photometry to be performed on a star of interest. Thus even fields as crowded as globular star clusters

can benefit from the two-dimensional sensing nature of the modern CCD to carry out photometric observations of a great number of stars simultaneously. This method of photometry was chosen, using IRAF scripts originally produced at the Dominion Astrophysical Observatory (IRAF/DAOPHOT)[9] For sake of comparison, additional testing of aperture photometry on uncrowded stars was performed. These methods and how they apply to the data are briefly described in following sections.

6.5. PSF Photometry Protocol

In this section the steps in the process of PSF photometry performed on GNAT images are described. In brief, these steps are: automatically locate stars on the object frames, perform 'first pass' photometry and mathematically model the PSF, fit the model PSF to stars on the frame, perform a second round of photometry on the fitted stars and finally extract tabular data from the results for plotting light curves.

---

[9]For a full account of the capabilities of this software, see the document "A Reference Guide to the IRAF/DAOPHOT Package" by Lindsey E. Davis, available at the IRAF website `http://iraf.noao.edu`.

6.5.1. Locating stars on object frames

In a crowded-field situation like that in the central few arcminutes of M67, automation of a stellar finding routine on object frames lends itself well to increasing the efficiency of the photometric process. This calls for an intelligent finding algorithm which can distinguish point sources from radiation events and other obviously nonstellar features on object frames. The task `daofind` was written with this goal in mind; it finds all point sources on the frame whose intensities are some user-defined number of standard deviations above the background, calculates approximate coordinates, instrumental magnitudes and shape parameters for each found object, and writes the results to a coordinate file for use in later steps in the photometry.

The `daofind` task is a good "first pass" attempt at locating stars on object frames, but it is far from foolproof. In fact, `daofind` is acknowledged to be imperfect at locating *all* stars on the frame and frequently misses even the brighter point sources well above the detection threshold. Fortunately, the DAOPHOT tasks `nstar`, `substar` and `allstar`, run subsequently in the photometry process, with very few exceptions detect the remaining stars not identified in the first pass of `daofind`. This insurance has the unwanted side effect of also identifying more nonstellar sources on the frames. However, as detailed in Section 6.5.4, the method of producing light curves from these photometric data necessarily rejects ephemeral, nonstellar sources from the analysis.

6.5.2. Initial pass at aperture photometry and modelling of the PSF

The results from `daofind` are then subjected to a kind of "first pass" at actual photometry in the task `phot`, where a user-defined aperture is placed over the star of interest and the flux within it summed as the first step of calculating a provisional instrumental magnitude. Given that `daofind` was designed to make only a rough approximation of the position of each point source it finds, `phot` reads in the coordinate list generated by `daofind` (*image name*.coo.1) and calculates new coordinates via a centering algorithm the user specifies in the `phot` parameter *calgorithm* applied to a box of size *cbox* around the position identified by `daofind` ("centroid" and 6 pixels for the algorithm and centering box size, respectively, were used). Additionally, `phot` sets the basis for the instrumental magnitude scale all measurements are placed on. The zero-point of the scale is established by arbitrarily setting the parameter *zmag* to the default value of 25, and observations from individual object frames are scaled in magnitude to account for varying exposure times, denoted by the image header parameter EXPTIME.

In PSF photometry, the apparent problem of performing aperture photometry in a crowded field is mitigated by the "subtraction" of stars on a case-by-case basis as photometry is performed on their neighbors; the otherwise interfering pixels within a subtracted stellar profile are replaced with the average background value in order to simulate how the surrounding, star-free sky would appear to the photometry aper-

ture. If all stellar profiles on a given frame were perfectly well-behaved Gaussians or Lorentzians, this problem would be made quite trivial; however, as already shown for the GNAT prototype telescope (see Section 5.3.2), stellar profiles are never so well-behaved in real life situations. Given that the shape of stellar PSFs in GNAT data vary significantly even within a single observing night, a robust algorithm for computing an analytic model for the PSF in each coadded image is required. The task `psf` allows the user to interactively choose the stars in a frame best suited for PSF modelling (generally isolated stars well above the background level). Note that the canonical task `pstselect` to generate a list of PSF stars is not used; rather, it is made an interactive step in the task psf by entering "" as the name of the input list of PSF stars. This is more a matter of personal preference in streamlining the photometry process rather than having any specific programmatic benefit.

6.5.3. PSF fitting

To apply the PSF model to stars in the object image for subtraction, a three-pronged approach was used that has the additional benefit of locating stars which `daofind` routinely fails to detect. This approach involves running the tasks `nstar`, `substar` and `allstar` sequentially. The combination of `nstar`+`substar` is nearly equivalent to running `allstar` once, which will likely cause the astute reader to ask the question "Why not simply run either process twice?" The answer to this is

more complex than the problem appears to be on the surface. The task `nstar` fits the PSF model to stars on object frames according to logical groupings which are among the output files of `psf`; `substar` then subtracts the fitted profiles from the object frame such that aperture photometry can be performed on the remaining stars. `allstar` is a second pass at the fitting to check that no stars are missed in the final photometry; it also reports the photometry results in a tabular fashion from which desired information can be extracted with the `txdump` task.

6.5.4. Extracting tabular data for generating light curves

Upon the completion of `allstar`, a text file containing the photometry results is generated and named *image_name*.als.1. It consists of a five-column table containing the following information: star ID number, x centroid (in pixels), y centroid (in pixels), instrumental magnitude and magnitude error. The `allstar` result file contains a great deal more information for each identified object including a number of parameters not germane to this analysis; the `txdump` task is used to extract only the desired quantities from the *image_name*.als.1 file. This task is invoked with the file name, parameters of interest and a Boolean term for matching, if a certain search pattern is desired for the output. `txdump` is run with the following syntax, redirecting the output to a text file with the ">" sign: **txdump** *image_name*.als.1 id,xcenter,ycenter,mag,merr yes > *image_name*_photresults.

6.5.5.   The DAOPHOT *error model*

The DAOPHOT algorithms `nstar` and `allstar` report the photometric precision for a given observation in the form of a magnitude error, in addition to other photometry parameters such as star coordinates, flux within the photometry aperture, etc. This is an empirical model drawing on a variety of noise sources present in a typical observation and computes the error "MERR" using an equation of the form

$$MERR = \sqrt{term1 + term2 + term3 + term4} \tag{12}$$

where $term1 = readnoise/epadu^2$, $term2 = 1/epadu$, $term3 = (0.01 * flaterr * I)^2$, and $term4 = (0.01 * proferr * M/p_1/p_2)^2$. Within the terms, *readnoise* is the effective CCD readout noise in electrons, *epadu* is the effective gain of the CCD in electrons per ADU, I is the pixel intensity in ADUs, M is the PSF model intensity in ADUs, *flaterr* is the flat-fielding error, *proferr* is the interpolation error and p_1 and p_2 are the FWHMs of the stellar profile in x and y, respectively. This model treats all the noise sources as essentially Poissonian ($\sqrt{N}$) in nature. Any deviation of the flat-fielding, readout and interpolation errors from a Poisson model represents higher-order terms dropped in favor of simplicity in this model. Deviations from Poissonian noise in the background cause this model to be inadequate for high precision work, but it still gives an order of magnitude estimate of the error.

MERR is only a rough estimate of the uncertainty on an individual magnitude

measurement (Everett & Howell 2001). In assigning error bars to points on the light curves, the uncertainty from a more fundamental point of view was calculated, as described in Appendix B.

Light curves are assembled from the tabular data output by the photometry software with the use of spreadsheets as described in Appendix A.

6.6.   Aperture photometry

In order to gauge the relative merits of different types of photometry given the condition of the data, simple aperture photometry was applied to a selection of stars in Field "A". The number of available stars was significantly less than that in the case of PSF photometry, as the crowded nature of the field in M67 gives rise to the possibility of contamination of the photometry results on a particular star by its neighbors. To this a sample of thirty stars spread around the central two-thirds or so of the frame was selected by hand; this spatial restriction was intended to maximize the number of frames in the series that all sampled stars appeared on in the time series, given the large pointing shifts from frame to frame. The stars in this region were subjected to the additional test of whether they had neighbors. Only those stars with no neighbors for a radius of at least 12 pixels from the star's centroid position were kept. The reason for this choice of radius will become clear momentarily. Stars passing both these tests are listed in Table 8.

Table 4.   User-added image header parameters relevant to calibration and
photometry tasks

Parameter Name	Parameter Description	Nominal Parameter Value
GAIN	Gain of the detector (e^-/ADU)	13
RDNOISE	Read noise of the detector (e^-/ADU)	1
DATE-OBS	UT Date of observation	yyyy-mm-dd
EPOCH	Current epoch for precession	yyyy
UT	UT time of observation	JD.FJD - JD
ST	Sidereal time of observation	(see text for description)
OBSERVAT	Name of observatory location	"kpno"

Table 5.   Parameter values for the `phot` task, DAOPHOT package.

Parameter	Nominal Value
Input image(s), `image`	(image name)
Output coordinate file(s) (default: image.coo.?), `output`	default
Output density enhancement image(s), `starmap`	""
Output sky image(s), `skymap`	""
Data dependent parameters, `datapars`	""
Object detection parameters, `findpars`	""
Boundary extension (constant—nearest—reflect—wrap), `boundary`	nearest
Constant for boundary extension, `constant`	0
Interactive mode, `interactive`	no
Verify critical daofind parameters, `verify`	)_.verify
Update critical daofind parameters, `update`	)_.update
Print daofind messages, `verbose`	)_.verbose
Graphics device, `graphics`	)_.graphics
Display device, `display`	)_.display
Image cursor: [x y wcs] key [cmd], `icommands`	""
Graphics cursor: [x y wcs] key [cmd], `gcommands`	""
mode	"ql"

Table 6.   Parameter values for the `phot` task, DAOPHOT package.

Parameter	Nominal Value
Input image	(*image name*)
Input coordinate list(s)	image.XX.coo
Output photometry file(s)	*image name*.mag.1
Centering algorithm	none
Sky fitting algorithm	mode
Inner radius of sky annulus in scale units	10
Width of sky annulus in scale units	10
File/list of aperture radii in scale units	3
Minimum good data value	0
Maximum good data value	32000

Table 7. Parameter values for the `psf` task, DAOPHOT package.

Parameter	Nominal Value
Input image(s), *image*	(image name)
Input photometry file(s) (default: image.mag.?), *photfile*	default
Input psf star list(s) (default: image.pst?), *pstfile*	""
Output PSF image(s) (default: image.psf.?), *psfimage*	default
Output PSF star list(s) (default:image.pst.?), *opstfile*	default
Output PSF star group file(s) (default: image.psg.?), *groupfile*	default
Output plot metacode file, *plotfile*	""
Data dependent parameters, *datapars*	""
Psf fitting parameters, *daopars*	"" ""
Match psf star list to photometry file(s) by id number, *matchbyid*	yes
Compute the psf interactively, *interactive*	no
Show plots of PSF stars, *showplots*	yes
Default plot type (mesh—contour—radial),*plottype*	mesh
Print daofind messages, *verbose*	)_.verbose
Verify critical psf parameters, *verify*	)_.verify
Update critical psf parameters, *update*	)_.update
Graphics device, *graphics*	)_.graphics
Display device, *display*	)_.display
Image cursor: [x y wcs] key [cmd], *icommands*	""
Graphics cursor: [x y wcs] key [cmd], *gcommands*	""
mode	"ql"

Table 8.   The selected stars measured with aperture photometry.

Designation	V
I15*	11.55
F83*	13.24
IV59	12.725
I36	13.285
IV35	13.795
IV36	13.340
I29	13.488
IV58	14.823
I48	14.052
IV68*	12.95
I37*	12.66
I51	14.122
IV77	12.862
IV27	13.898
I38*	13.61
I47	14.632
IV69	
IV39	14.925
I42	14.693
I44	13.640
II8	14.972
IV16	14.333
IV57	14.562
II20	12.650
I58	14.695
IV30	12.831

The aperture photometry process in IRAF proceeds as follows. First, the program objects are identified either manually or automatically, as with the `daofind` routine, borrowed from the PSF photometry package DAOPHOT. Next, sky background values are determined for each of the selected objects with the task `fitsky`; it calculates values for parameters such as the mode, standard deviation and skew of the pixels in the sky annulus as declared in the parameter files `fitskypars`. A text file for each object is generated in which these values are recorded; the `phot` task, the final step in the procedure, parses these files for the information it needs in order to do a proper sky background subtraction from each program object. Finally, `phot` sums the flux in the software aperture around each star, corrects for the sky background, and outputs a formatted text file for each frame with magnitudes and error estimates for each object. These text files are in the same format as those resulting from the photometry routines in DAOPHOT, which are manipulated with the task `txdump` to extract fields of interest. These extracted, tabular data are imported into a spreadsheet for selection of photometry ensembles, calculation of differential magnitudes, and assembly of light curves.

This time the frames were registered using the `interp.csh` cshell script packaged as part of the ISIS image subtraction software (give URL) in order to reduce the pain involved in assembling the photometry results for plotting. Photometry was performed on the resulting, registered images using an aperture size of 3 pixels. This

value was chosen after early comparative results testing apertures as small as 3 and as large as 6 pixels; a 3-pixel radius aperture consistently gave the lowest estimated photometric error, due to the fact that it just contained the PSF width (averaging 2.5 pixels) and yet rejected most of the background immediately around the star. A gap of 3 pixels between the aperture and the inner radius of the sky annulus was allowed; the annulus had a width of 5 pixels. This is something of an arbitrary choice, but gives about 300 pixels in the sky annulus from which to draw statistical information about the background level. Annuli narrower than about 3 pixels seem to undersample the background and yield misleading results; those wider than about 10 pixels provide no useful, additional information about the background to justify the processor time required to sample all their contained pixels.

The photometry results from `phot` were assembled using the Excel spreadsheet software, as before; the registration method used required considerably less manual effort to produce light curves than reported previously for the "spreadsheet reduction" process outlined in the previous section on PSF photometry. Some work is still necessary in order to format the columns for plotting and to calculate empirical errors. An ensemble of six stars, I58 ($B-V$=0.761), I38 ($B-V$=0.550). I42($B-V$=0.632), II30 ($B-V$=0.597), IV57 ($B-V$=0.862) and I44 ($B-V$=0.659), was chosen based on the standard deviations of their instrumental magnitudes being the lowest of the thirty program stars and hence least likely to show any variability to contaminate

the differential photometry. Differential magnitudes for all stars in the sample were

calculated, and checks for variability of the ensemble stars were performed to assure

a "clean" ensemble selection.

Table 8—Continued

Designation	V
I13	15.107
II30	13.148
F153*	11.30
IV56	14.054

Note. — Magnitudes for stars with asterisks taken from Eggen & Sandage (1964); the remainder are from Montgomery et al. (1993).

7.   Photometry Results

One major goal of this work was to evaluate several different photometry methods, applied to GNAT data, to understand their relative strengths and weaknesses. In this way it was hoped a more informed decision could be made regarding which method to use for routine data analysis in future GNAT efforts. Of the two photometry methods tested, simple aperture photometry best suited the data despite the limited selection of targets it provides. In each case, however, some sample light curves are provided here with commentary on the difficulties the characteristics of the data pose.

7.1.   PSF Photometry

The principal weakness of the PSF-fitting method of photometry, as tested here with the IRAF package DAOPHOT, is in the use of a constant PSF model applied across an entire object frame. After the user identifies a particular number of "PSF stars", the software computes an empirical model which is used with all the remaining stars on the frame for subtraction. If the PSF varies significantly across the frame, as can be the case in situations involving e.g., optical distortions, the major source of photometric error will be the individual errors between the model and actual PSFs. This is an issue addressed specifically in the case of the image subtraction method,

which allows for spatial variations in the size and shape of the PSF to better conform

to the actual stellar profiles on object frames.

One way of testing the accuracy of the photometry is to see how well the data

follow the error model. Figure 27 shows an example of this kind of test; here is
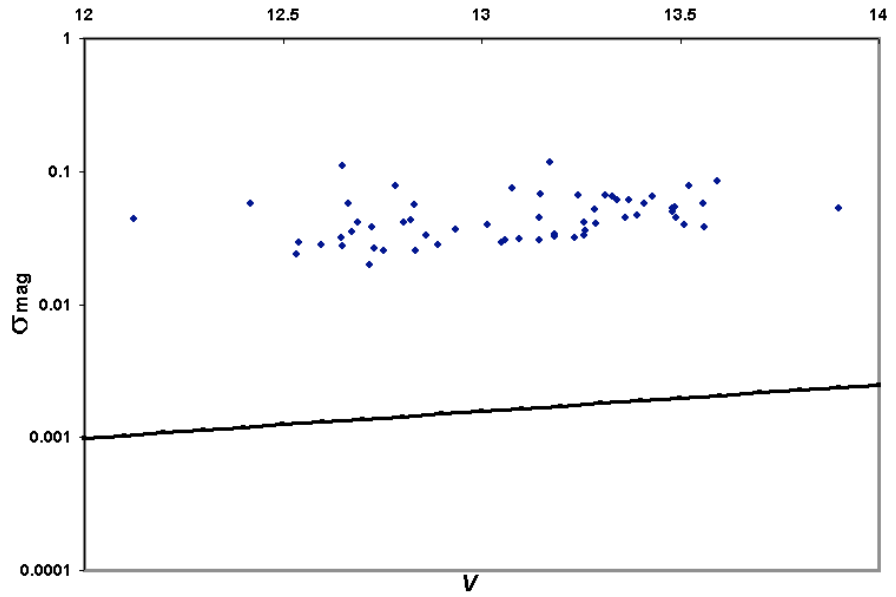
Fig. 27.— The "time series error" of ensemble differential magnitudes from PSF photometry as a function of V magnitude in M67 over the period of nights from MJD 51935-51991. Actual data are plotted as points; the overplotted solid line is the curve expected for errors determined solely by Poisson statistics.

presented the standard deviation error of the time series differential light curves of the

brightest 59 stars in Field "A" of M67 for which V magnitudes from Montgomery et al.

(1993) as a function of those magnitudes were available. Also plotted as a solid line

is the expected result for noise limited by Poisson statistics. While the distribution

of points generally follows the line, note the roughly constant offset between them.

This is a concrete demonstration of the difference between the precision theoretically achievable with a telescope of the 0.5-meter's size and the actual precision attained with, in this case, PSF photometry. The fact that the offset is a constant value suggests that whatever the source of noise causing it, there is no correlation between the brightness of the star and the magnitude of the effect. In other words, it is independent of external factors such as magnitude or position on the sky. This further suggests a source of noise internal to the system which is not spatially variable across a frame.

Suspicion immediately returns to the issue of the variable background level described previously in Section 5.3.7. Further evidence for this behavior can be seen if the time series sigma is plotted against differential magnitude, as in Figure 28. In this plot there is an effect very different from the expected result: the error is distributed about a value of approximately zero, meaning that the scatter in the light curves is generally smallest for stars whose instrumental magnitudes are closest to the ensemble mean. The expectation, on the other hand, is that the values of σ_{mag} ought to be smallest for the brightest stars (most negative differential magnitudes), increasing gradually as stars get fainter. This is in accord with the Poisson-limited noise model. But what do the light curves look like; i.e., is the scatter of points random or structured? The clearest demonstration of the effect comes if light curves of stars both brighter and fainter than the ensemble mean are plotted simultaneously,
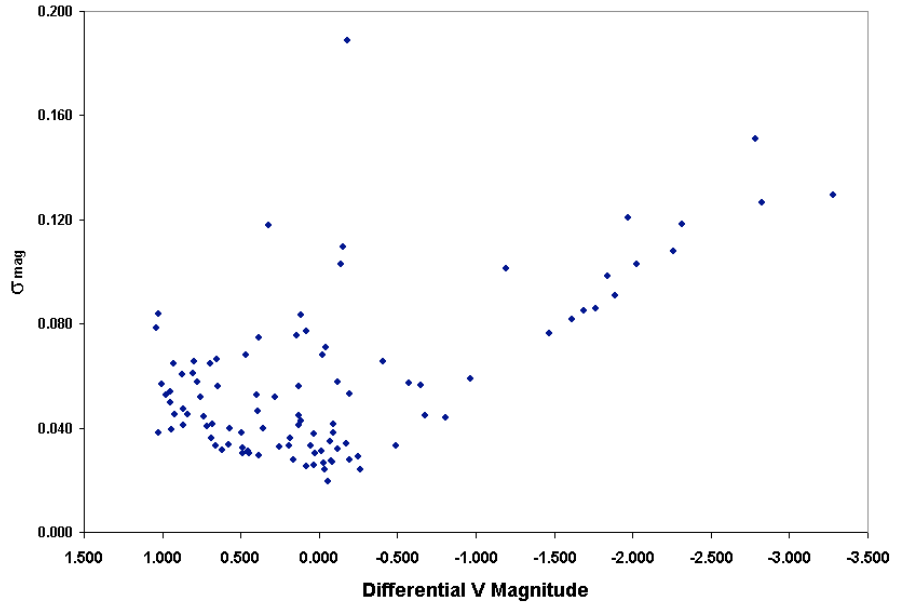
Fig. 28.— The time-series photometric error σ_{mag} as a function of ensemble differential magnitudes for the period MJD 51935-51991.

as in Figure 29. The bizarre behavior of these light curves is immediately obvious: relatively bright stars become "brighter" and relatively faint stars grow "fainter" as a night goes on, then the process resets for the following night. To illustrate this effect the curves for three stars bracketing the set of differential magnitudes about zero were selectively plotted; also, the abscissa has been scaled to only a few nights' time in order to show the slopes clearly, but the effect is consistent for each night throughout the time series. The star F127 presents a flat curve as expected for any nonvariable star in the field, regardless of brightness. That is, after all, the result of making a differential measurement between two objects of essentially constant flux. However, as differential magnitudes move away from zero, the behavior of the light curves be-
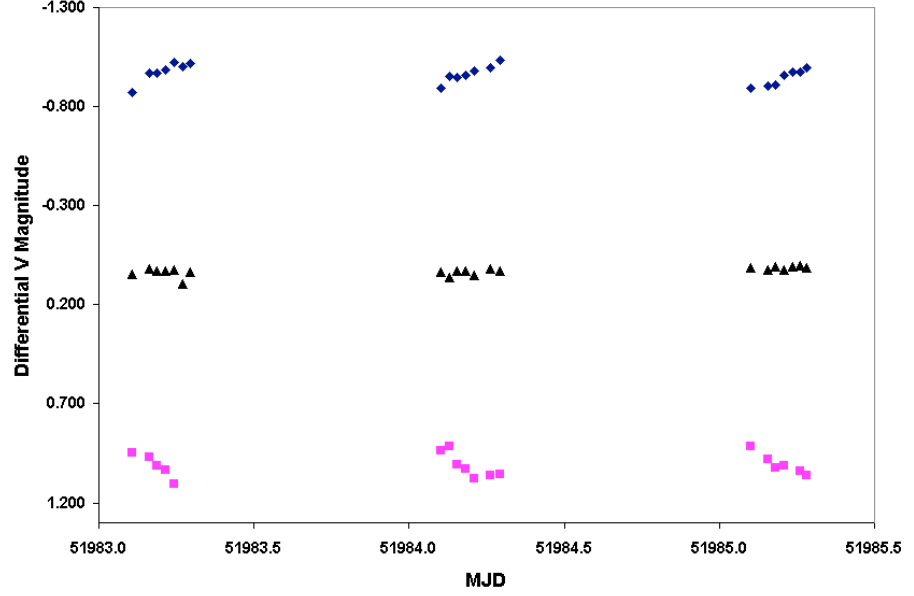
Fig. 29.— Light curves of three stars generated with DAOPHOT photometry routines; IV76 (diamonds), F127(triangles) and I31(squares). Error bars are not included as they are approximately the dimensions of the points at this resolution.

gins to explain what is seen in Figure 28. On the faint end, the increasing value of σ_{mag} is not due to increased random scatter as expected, but rather the downward slope of the light curve. The same is true for the bright star which again violates expectations. The nature of the effect is variable with time and repeats consistently from night to night with approximately the same magnitude and duration. Having ruled out any external effect which could account for this, it is most probable that a noise source internal to the system of telescope and detector causes the behavior seen in the light curves. The only noise source that behaves in this manner is the variable background level.

A reasonable solution to this problem that works well in cases where one wishes

to plot only a small number of light curves is to adjust the selection of ensemble

stars to roughly match the instrumental magnitude of the program stars in question.

Alternately, one can achieve the same effect by adding or subtracting a constant scale

factor to the ensemble means. When this is done, the values of σ_{mag} are brought

much closer to the Poisson-limit. Variability of some of the known variable stars of

M67, such as the W Ursa Majoris star I24 (Figure 30), has been detected using this

method. There is clear evidence for variation here, as the amplitude of the curve is
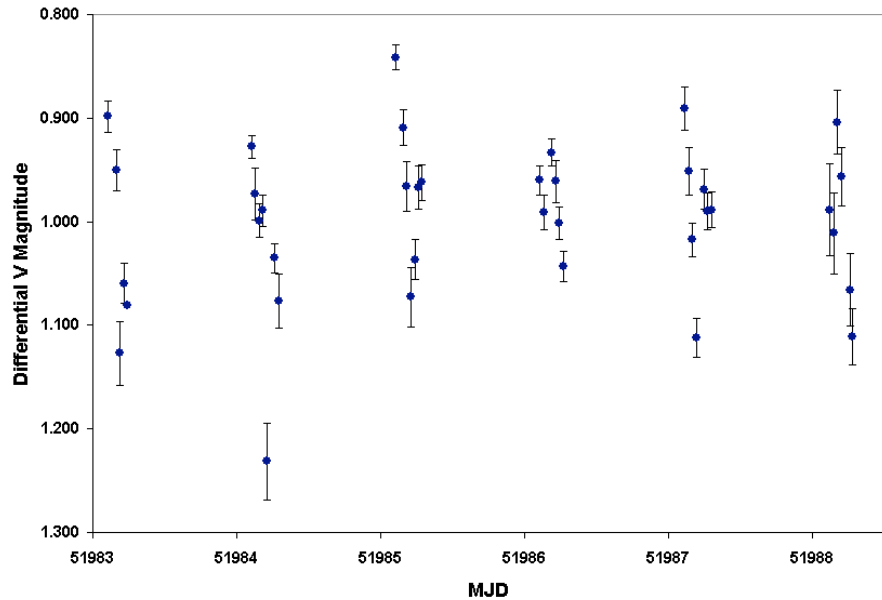
Fig. 30.— Light curve of the W UMa binary star I24 generated with PSF photometry.
Error bars are those computed by IRAF.

well outside the errors on the individual measurements. However, if the ensemble

needs to be constructed individually for each star of interest in a field, the need for

custom software becomes clear.

7.2.   Aperture photometry

Results of experiments with simple aperture photometry reveal some information about the quality of the data. First, the same "sawtooth" pattern behavior is seen in the light curves of stars whose differential magnitudes are significantly higher or lower than zero. This is evident in Figure 31, a plot of the ensemble mean as a function of time. Error bars have been calculated empirically according to Everett
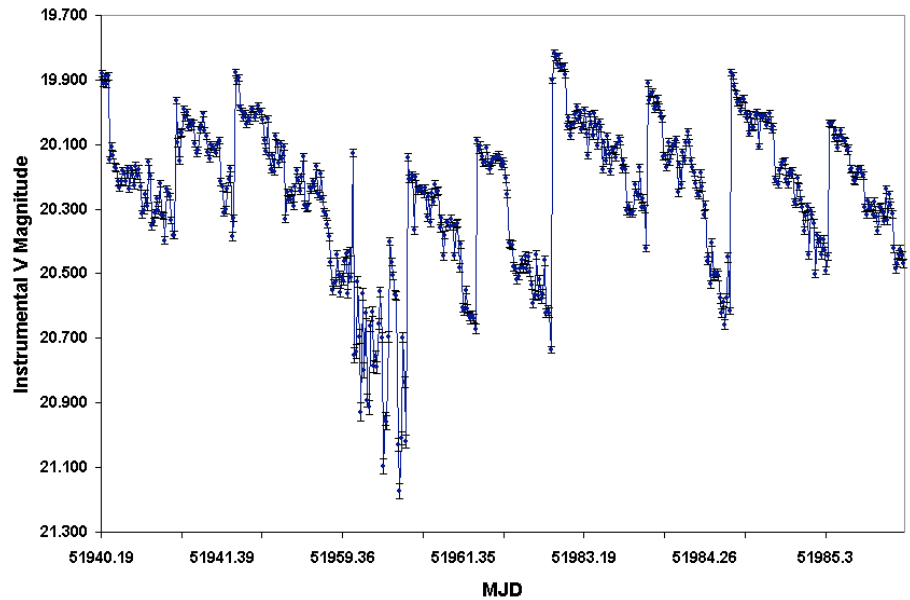
Fig. 31.— The ensemble mean instrumental magnitude as a function of MJD for the aperture photometry method. Note that gaps in the time series have been eliminated.

& Howell (2001) (see Appendix B); note that the sawtooth is statistically significant given how small the errors are. Consequently, the light curves of stars much brighter or fainter than the ensemble behave as in Figure 29. The most egregious example of how the changing background level affects the quality of the photometry results

occurs on the night of MJD 51960 in this figure. The steep drop in the ensemble mean magnitude is indicative of the unusually high background values in images from this night (see Figure 23). Note that this effect imprints itself also upon the light curves, as in Figure 32 below, for they derive ultimately from the ensemble means. The
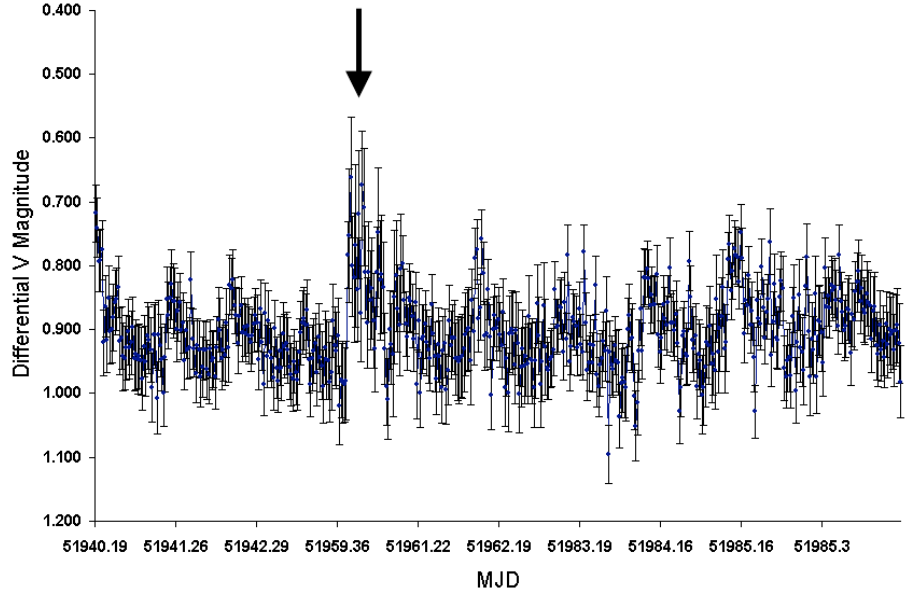
Fig. 32.— Light curve of the star I38 (V=13.61) generated with the aperture photometry package APPHOT; note that gaps in the time series have been deliberately removed for this plot. The arrow marks the feature on MJD 51960 discussed in the text. This light curve has a time series precision of σ_{mag}=0.060 mag.

suspect location is marked with an arrow in this figure; comparison with Figure 31 demonstrated the correlation between wildly varying background values and the effect on light curves.

One method developed to handle the effect of a background that changes at a constant rate is to fit the change with a line and subtract the slope from differen-

tial magnitudes. Zhou (2001) used this method in a similar method on time series photometric data of stars in M67. They did not make corrections for extinction and removed its effects from their light curves by subtracting off a linear fit to their data. A similar strategy could be exploited in dealing with the light curves, but the variation within a night is not linear; fits to the data give r^2 values from 0.70 to 0.80, leading to rejection of the hypothesis that the underlying cause of the "sawtooth" behavior is linear. Rather, it is a higher order function – likely directly proportional to the variation in background seen in Figure 22.

The best representative light curve of the lot examined is that of the star I58, shown in Figure 33; best, in this case, simply means that of the star closest in instrumental magnitude to the ensemble mean on each frame, key to eliminating the "sawtooth" pattern. Note that there is still some residual effect from the background variations on MJD 51960 already discussed. However, the curve is remarkably flat over the 45 nights spanning this plot, which bodes well for the repeatability of the results reported here. Light curves with only 1-2% variation over a span of weeks are required in order to approach the data quality required by the GNAT science agenda.

As found in the case of PSF-fitting photometry with DAOPHOT, the magnitude of the background dependent effect is large enough to overwhelm any useful information in the data about the quantitative differences between PSF and aperture photometry results. Based on the scatter in the light curves, the differences in the quality of results
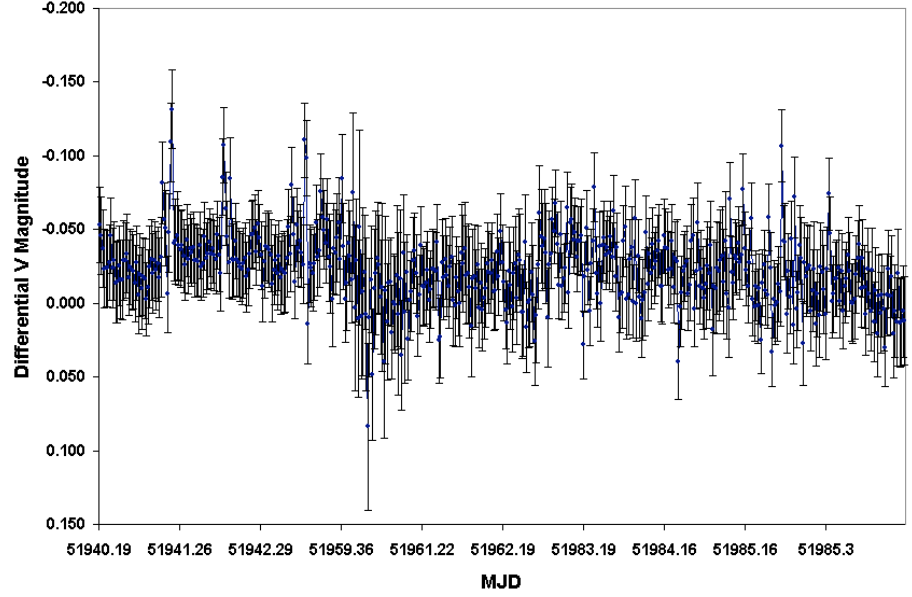
Fig. 33.— Light curve of the star I58 (V=14.695) generated with the aperture photometry package APPHOT. Gaps in the time series have again been removed. Error bars have been calculated empirically as in Appendix B. This light curve has a time series precision of σ_{mag}=0.024 mag.

generated with the two approaches must differ by less than about 10%. This figure is also considerably higher than the threshold of around 1-2% needed to achieve in order to study low-amplitude variability of stars in a cluster such as M67. Additionally, a time series precision of ~10% for most stars effectively rules out detection of planet transits.

Finally, the same kind of diagnostic plot as previously in the case of PSF photometry is presented for the aperture photometry results. Figure 34 shows the time series scatter of the stars selected for aperture photometry. The data are again well above the cutoff for pure Poisson noise, established by the solid line. The difference
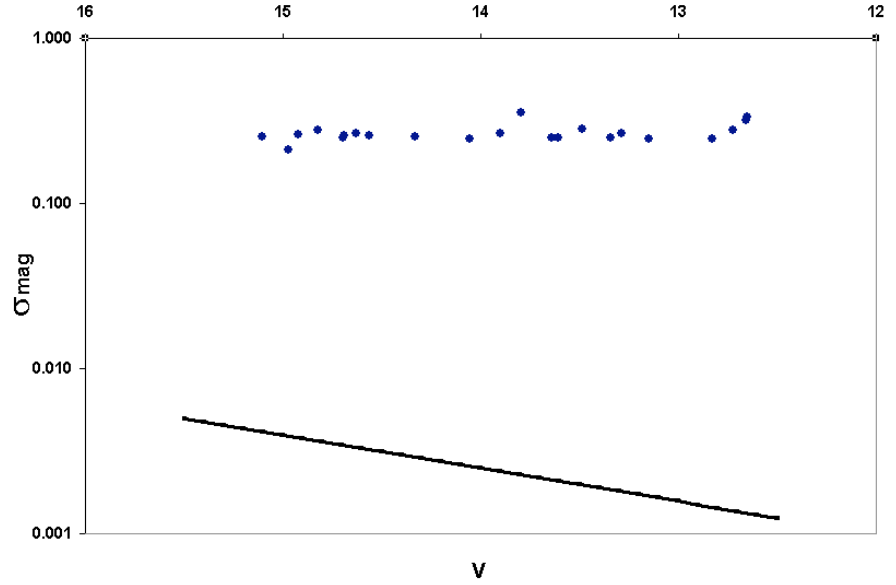
Fig. 34.— The "time series error" of ensemble differential magnitudes from aperture photometry as a function of V magnitude in M67 over the period of nights from MJD 51935-51991. Actual data are plotted as points; the overplotted solid line is the curve expected for errors limited by Poisson statistics.

between this figure and Figure 27 is most evident in the case of the brighter stars. It is thought this is the result of some flux from neighboring stars falling in the aperture of the brighter stars on the frame, as most are coincidentally more crowded than the fainter stars. In any case, the values of σ_{mag} are still well above the floor established by Poisson noise, returning suspicion to the elevated background levels common to all data frames.

7.3. Solving the "sawtooth" problem

The most serious problem affecting the GNAT differential photometry results is the previously described "sawtooth" pattern in the light curves, affecting stars differently depending on their differential brightness. This is, once again, the trend in the light curves of bright stars to get "brighter" and faint stars to get "fainter" as the night goes on, then returning to their initial magnitudes at the beginning of the following night. The only stars which do not show this behavior are those whose differential magnitudes are closest to zero. The sawtooth would be easier to understand if it were not *differential* magnitude-dependent; in fact, such systematic behavior in differential light curves defies the very nature of such differential measurements. Thus, suspecting some unaccounted-for factor at work here, some suggested leads were pursued which might shed light on the problem.

First, a search was made for any residual extinction or external scattered light effects in the data by plotting differential magnitudes for a selection of stars in one of the search fields against the airmass at the time of observation. Four stars approximately spanning the range of brightnesses sampled in the data were chosen, at its limits corresponding to the strongest pitch of the sawtooth. Results are shown in Figure 35, and come as some surprise. These curves should be essentially flat, given that variations in stars' intensities due to airmass-dependent extinction; note, however, that these points were obtained over a 43-night interval with major gaps in
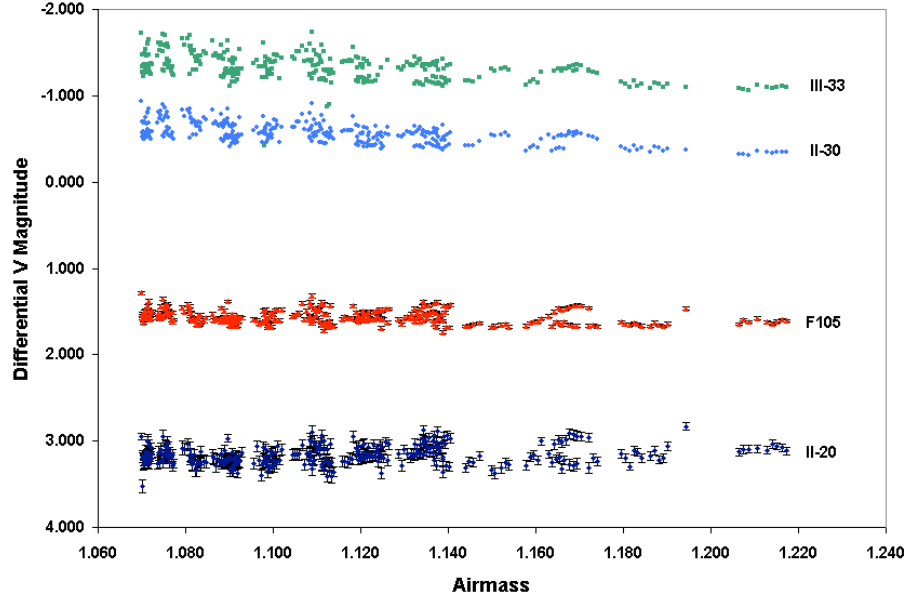
Fig. 35.— Differential V magnitudes versus airmass at time of observation for four stars in Field "B" chosen to span the approximate range of magnitudes in the sample. Error bars for the brightest stars are smaller than the data points themselves.

the time series. While it is possible that long-term transparency variations occurred in this interval, any such changes should still be accounted for in the ensemble, thus rendering these curves flat again.

The results are doubly interesting. First, the brightest stars show the greatest scatter in differential magnitude for a given airmass, particularly near the zenith. Since extinction depends quadratically on airmass (Equation 7), the lowest scatter should be at the zenith, rapidly increasing with larger zenith angles. Note that the scatter is much larger than the error bars on the brightest stars' points in Figure 35, whereas for the faintest star shown, all variation with airmass is less than 1σ. Second, there is an overall residual trend among the brighter stars toward lower differential

magnitudes at increasingly larger airmass. The trend is barely evident in the figure among the two brightest stars, but it is significant in comparison to the fainter stars we observed. The total variation in the differential magnitudes of the brightest star in the figure over the plotted range of magnitudes is about 0.3 mag. While this is approximately the pitch of the sawtooth for the brightest stars, a correlation would only be possible between that affect and the airmass dependence seen if time and airmass had a linear relationship. Instead, a quadratic relationship is noted with a global minimum at the moment of transit.

One difficulty with this analysis is that there is a bias in the data towards observations at low airmass. This is a desirable consequence of observing an object that transits near the zenith, as it limits the effect of extinction on the data. However, it yields an incomplete picture of the behavior of differential magnitudes for all brightnesses of stars at relatively high airmass. In consideration of this fact, it is concluded that any dependence of differential magnitudes on airmass is not responsible for the sawtooth effect.

Our decision to omit certain calibrations from the processing of raw data was next proposed as an explanation for residual effects in the light curves. Dark current and bias level subtraction were dropped from the reduction pipeline upon the discovery that applying these calibrations introduced an unacceptable level of spatial pattern noise to the object images. However, the relatively high running temperature of the

camera causes non-negligible dark current, a source of noise in the photometry. To

ascertain how data are affected by dark current and the bias level, a sample night of

data was reduced again, including those calibrations and the results compared against

data from the same night reduced without darks or biases. An example of the results

is shown in Figure 36. This plot shows the light curve of the same star made with the
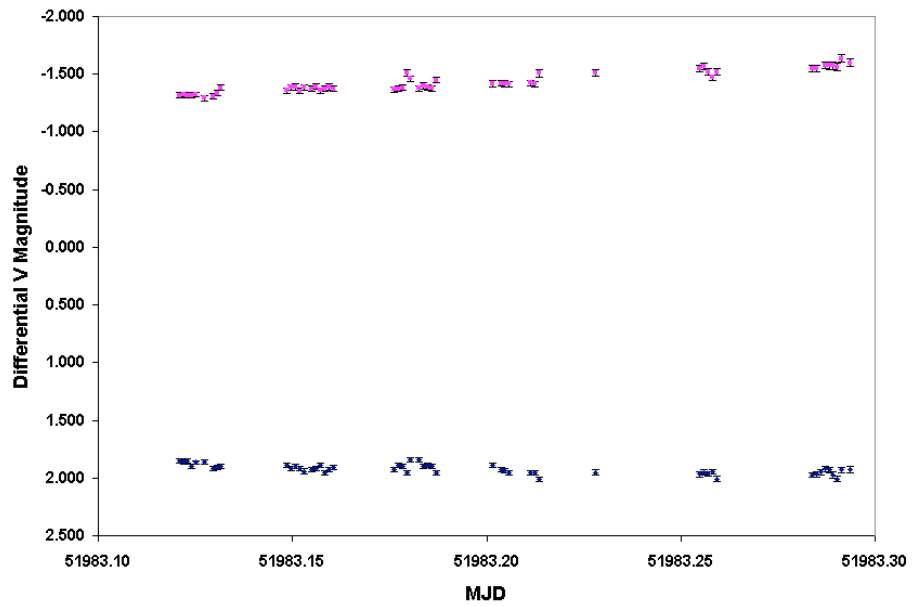
Fig. 36.— A comparison of light curve results for two different data reduction methods. Both traces show the light curve of the ensemble star F23; the upper trace results from data where dark subtraction was performed while the lower trace was made without dark subtraction.

two different approaches in the reductions; the relatively large offset between them

is the result of the changing ensemble mean value. All stars on the frame were also

subjected to the two different reduction methods, and it is the different background

values that cause the large changes in instrumental magnitude. Of the two data sets

plotted, the "properly reduced" version shows the greatest variation – about 0.2 mag

– over the night, while the set made without dark and bias subtraction shows a total change of about half that value. Similar results were obtained for a variety of stars over a range of brightness. This result appears to confirm suspicions regarding the contribution of the pattern noise in dark and bias frames to the noise in the time-series photometry. This possibility in explaining the origin of the sawtooth has therefore been discarded.

The possibility of strong color differences between ensemble stars and program stars as a source of the sawtooth was investigated. An average $B - V$ color of 0.598 was noted among target objects, nearly all of which are M67 cluster members, so two test ensembles were established: one comprised of stars whose $B - V$ colors fall within 1σ (0.107) of the mean, and another whose stars' colors are redder than 1σ above the mean. The 1σ limit is entirely arbitrary, but motivated by the near-absence of stars redder than this limit in the available sample. A "blue" ensemble could not be created and tested due to the dearth of blue stars in the M67 fields observed. Light curves for a number of stars were produced using both ensembles; an example is shown for the star I198 in Figure 37. This star was chosen to illustrate the results for two reasons: first, its color ($B - V$=0.566) is very close to the cluster mean such that it is "representative" of cluster stars at least in the color sense, and second, its differential magnitude is sufficiently nonzero to show the sawtooth effect well in the first place. Differences in the ensemble mean between the two ensembles account for
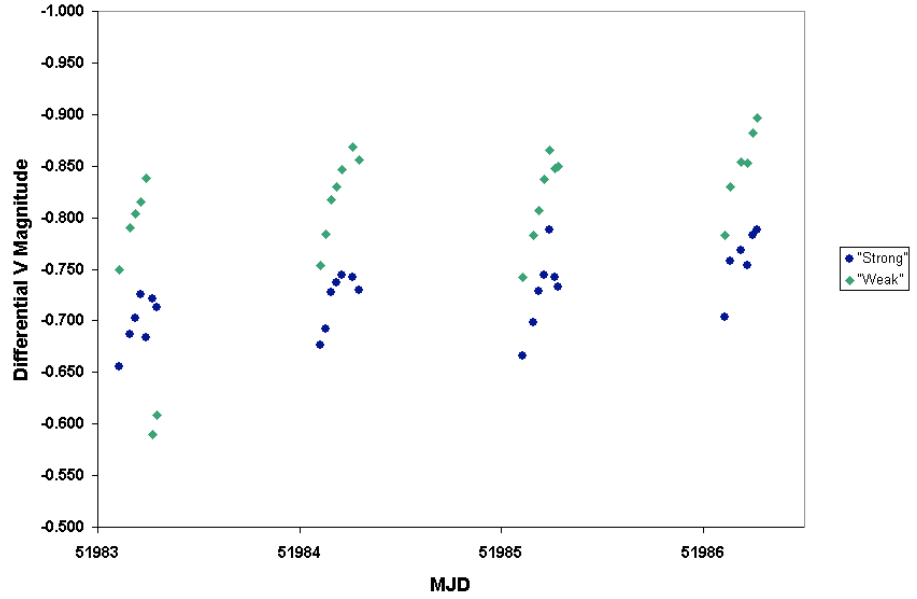
Fig. 37.— Light curves of the star ES I-198 (V=13.145, $B-V$=0.566) made with two color-dependent ensembles: one "strong" (average $B-V$=0.835) and another "weak" (average $B-V$=0.581).

the displacement of the two light curves in the magnitude direction. The figure shows that there is no mitigation of the sawtooth either with an ensemble similar in color to the program star, or one showing an extreme color difference.

Figure 38 shows a plot of the two curves in the previous figure versus one another; there is clearly a direct relationship, discounting the few outliers above the noise. When those four points are removed, the remaining data are correlated at r^2=0.832; given the scatter in the points, attributable to differing observing conditions over the time series, there is a reasonably positive correlation between the light curves. Any effect due to color differences amounts to, at the very most, perhaps a percent in the photometry.
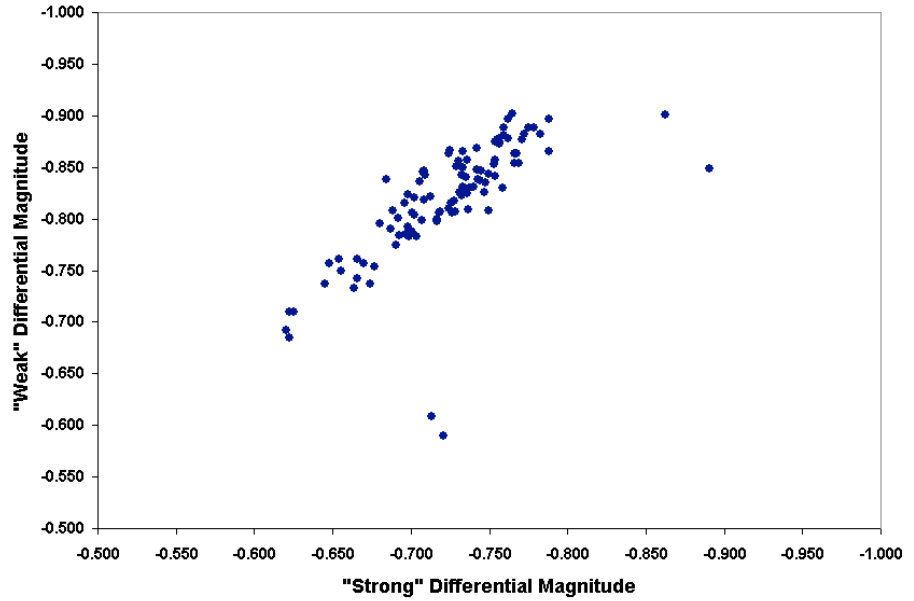
Fig. 38.— "Weak" versus "strong" differential magnitudes for the star I198 (see Figure 37 for explanation of terms).

Finally, a growth curve analysis was performed to examine the effect of aperture radius selection on the resulting instrumental magnitudes. The character of the sawtooth − instrumental magnitudes varying linearly with time from the beginning to end of nights − suggests that the optimal aperture choice, maximizing the S/N of a given photometric observation, varies during the night. In this manner, for a fixed aperture radius choice, an observation at maximum S/N at one time during a night may not be repeatable at another time. Presumably the fixed aperture choice *is* appropriate at some time of the night, therefore maximizing S/N in a way which should be observable vis growth curves. To test this idea, growth curves were generated for stars of different brightness at times throughout the night of MJD 51983; any change

in the ideal aperture radius choice should manifest as a time evolution of the curves for any particular star.

Recall the discussion of aperture radius selection in Section 4; the ideal radius aperture encircles as much of the light from the target object as possible while minimizing the number of background or "sky" pixels it contains. The S/N is maximized in this circumstance. Increasing the radius beyond this optimal choice diminishes S/N by increasing the total number of background photons collected, and hence, the noise in the observation. Conversely, decreasing the radius decreases the S/N by excluding light from the PSF of the star, thus decreasing the signal in the observation. Yet the ideal aperture radius choice often fails to encompass the light from the stars in the extreme wings of the PSF; this light is sacrificed as its level drops into the noise. For large aperture radii, increasing the radius causes the S/N to drop. It is expected that in the large aperture limit, the resulting instrumental magnitudes will asymptotically approach a limiting value. Further increasing the aperture radius only serves to encompass additional background pixels without adding any signal from the star; the additional $\sqrt{N}$ noise merely makes for larger error bars.

Growth curves constructed for M67 stars in GNAT images show curious results. Figure 39 contains curves of S/N for several stars spanning the typical magnitude range of stars recorded in a typical 60 s integration. The data in this plot were taken from images recorded on MJD51983, a night thought to be representative of
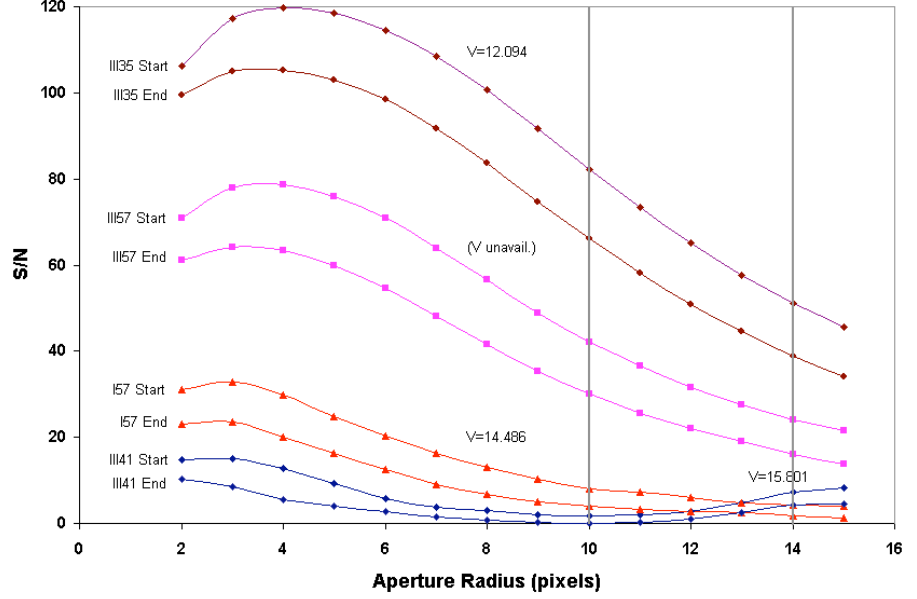
Fig. 39.— Growth curves for several stars in M67 derived from images captured on MJD51983. Vertical lines give the inner and outer radii of the annulus used in sky subtraction.

the best quality data obtained in the spring of 2001. Stars selected for inclusion in this plot had no neighbors within a radius of 20 pixels plus the seeing FWHM to help ensure against overlap. Aperture radii values between 2 and 15 pixels are included; for reference, the seeing FWHM averaged around $3''$ on this night. The sky background was sampled with an annulus having inner and outer radii of 10 and 14 pixels, respectively, such that the aperture selection plotted overlaps and slightly exceeds the sky sampling region. S/N values were calculated from the first-principles approach of Everett & Howell (2001) (see Appendix B).

To test the idea of time-evolution in the growth curves, two traces are plotted for each star: one trace for the first image in the time series that night and one for

the last image in the time series. During this time M67's observed position on the local sky changed from an hour angle of approximately 2h east of the meridian to 2h30m west, bracketing its transit. These curves behave essentially as expected: with the notable exception of the faintest star, the S/N of each star peaks at an aperture radius about 1 pixel larger than the seeing FWHM and gradually drops off at larger radii. Note, however, that the peak S/N aperture radius shifts slightly through the night for the brightest two stars from 4 to 3 pixels. No similar change is seen in the curves of the V=14.486 star I57, while the faintest star, III41, at a magnitude of almost V=16, shows a double maximum. At large aperture radii, the measured S/N is nearly equal to the values at small radii; visual inspection of images confirms this effect is not caused by the presence of nearby stars. At a minimum, this plot suggests that the optimal aperture radius value for maximizing S/N changes throughout a night for brighter stars.

If instrumental magnitude is plotted rather than S/N in the growth curves, different behavior is expected, for the two vary in distinctly different ways as a function of increasing aperture radius. While the S/N curves are expected to show maxima at aperture radii approximately equal to the seeing FWHM, instrumental magnitude curves should not show such maxima. Instrumental magnitude is determined in the software by summing the background-subtracted flux within the aperture and placing

the value on a $\log_{10}$ scale as follows:

$$m_{inst} = -2.5log_{10}(F) + C, \tag{13}$$

where F is the flux in counts and C is the instrumental zeropoint, the latter an arbitrary value. This relation predicts that as F increases (a consequence of increasing the aperture radius), m_{inst} will asymptotically approach a limiting value determined by the total flux from the star integrated across the entire PSF. Just where the wings of the star finally drop to zero flux is a matter of the individual conditions of telescope, site and atmosphere; beyond this radius from the stellar centroid position, no additional flux from the star is added with increasing aperture radius. The consequence for S/N is a decrease as more sky is sampled, but with instrumental magnitude, assuming good background subtraction, F levels out to a constant value. However, due to the finite width of the distribution of sky pixel values, sampling more sky will tend to enlarge the error bars on instrumental magnitude measurements.

GNAT data do not always follow this expected pattern, providing some additional information on the quality of those data. Instrumental magnitudes were calculated for several stars over a range of aperture radii, again overlapping the sky annulus radii. Figure 40 gives growth curves of instrumental magnitude for aperture radii between 2 and 15 pixels for some of the same stars plotted in the previous figure. Their magnitudes, again, span the approximate range for stars detected in individual 60 s integrations, and the individual plots are arranged in order of descending brightness.
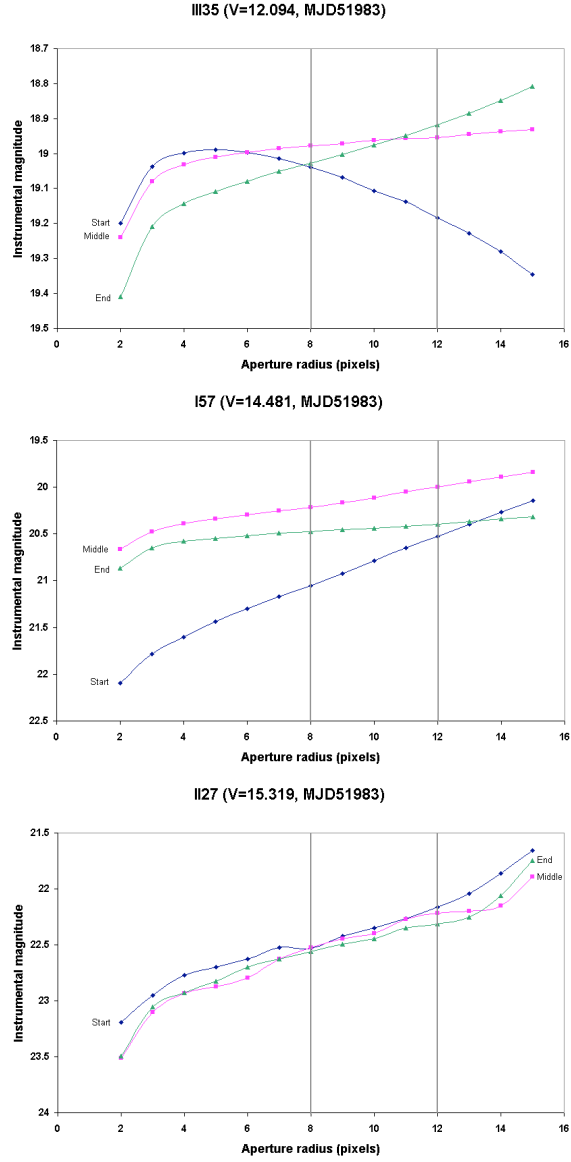
Fig. 40.— Growth curves of instrumental magnitude for several stars in M67 derived from images captured on MJD 51983. Vertical lines give the inner and outer radii of the annulus used in sky subtraction.

To examine the behavior of these curves throughout an observing night, three traces are given for each star on the night of MJD 51983: one each for the first and last images in the set for that night, and an intermediate trace roughly halfway through

the night. None of the plots show consistently "correct" behavior of the curves ac-
cording to expectations, but the evolutionary behavior of the individual stars' curves
is interesting. The curve of the bright star III35 acts like expected for a S/N curve
at the beginning of the night, its instrumental magnitude *decreasing* after the initial
expected rise. Later in the night, the curve resembles the ideal pattern more closely,
peaking at an instrumental magnitude of about 18.95, but by the end of the night, the
growth curve is increasing without limit toward large apertures. Unrestrained growth
is seen in the curves of the other two stars; the faint star II27 shows this behavior at
all times during the night. Comparison of the same stars' curves from other nights
in the data set shows similarly inconsistent behavior, and the scattered positions of
these stars around the frame suggests a non-local effect all three stars are subject to.
The inconsistent behavior of the curves is troublesome, particularly in cases such as
the peaked curve in the plot of III35.

Those inconsistencies aside for a moment, given that these data lend support to
the notion of changing optimal aperture radius throughout the night, the following
scheme for constructing light curves is envisioned. S/N growth curves are calculated
for each individual star in software, and the instrumental magnitudes are calculated
through the aperture empirically shown to maximize S/N. In this way, the high-
est S/N observation of each star on each frame alone is used for constructing the
light curves. In practice, this can be done in a spreadsheet such as Excel with the

cell function MAX, which returns the value in a range of cells with the highest numerical value. The aperture radius of the value returned by MAX is compared to another sheet containing the growth curve values for instrumental magnitude for the same stars, and these highest S/N magnitudes are extracted and plotted. When this approach was applied to the three stars in the previous figure, the "sawtooth" virtually disappeared from the ensemble differential light curves. Figure 41 shows the instrumental magnitude light curves derived in this manner. The most obvious
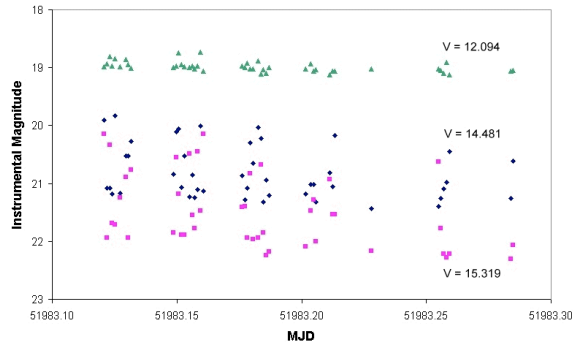
Fig. 41.— Instrumental magnitude light curves of several stars observed on MJD51983 plotted according to maximum S/N for each observation.

effect of this reduction process is the large scatter in magnitudes of the fainter stars, revealing that maximizing S/N does not necessarily correspond to a consistent set of magnitudes, particularly as flux decreases with fainter magnitudes. An ensemble was defined by these three stars and used to calculate ensemble differential magnitudes for each. The resulting light curves are shown in Figure 42. In this plot, the scatter in the light curves for all three stars is about the same, regardless of magnitude. More importantly, the strong pitch of the sawtooth is not evident in this figure for any of
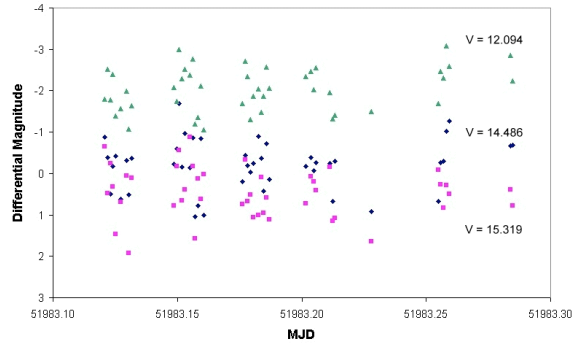
Fig. 42.— Ensemble differential light curves of the three stars in Figure 41.

the traces. This statement comes with the caveat that the scatter in the points may be masking any underlying trend in the light curves. As a diagnostic test, then, it cannot be conclusively shown that optimizing the selection of apertures eliminates the sawtooth effect. Nevertheless, evidence exists suggesting that changes in the optimal aperture choice throughout a night explain the sawtooth at least in part.

The problem of the sawtooth has not been definitively solved after all. There remains some systematic effect in the data which produces it, yet is elusive despite testing a number of ideas. It is something peculiar to this telescope and detector combination which was consistently present throughout the spring of 2001 when this analysis was conducted. Testing of future GNAT instrumentation is strongly recommended in order to prevent this effect from influencing data collected with those instruments.

7.4.   A new variable star in M67?

Finally, some scientifically useful results from this characterization effort are presented that add some complexity to the picture of variable stars in M67. In the course of examining light curves of stars in Field "B", one ensemble star, III28, was found whose light curve (Figure 43) was definitely not the expected shape of a non-
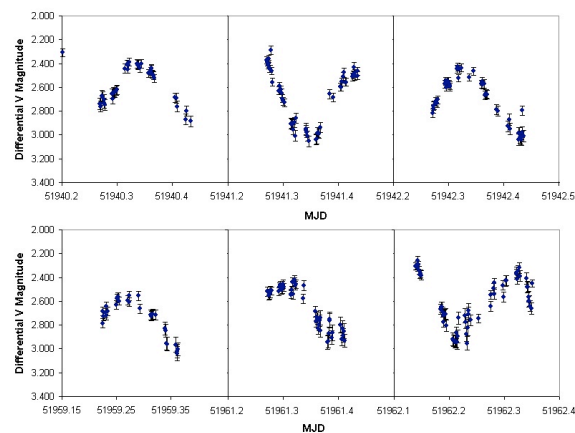
Fig. 43.— Light curve of the suspected variable star ES III-28.

variable star. Instead, clear, semi-periodic variation is seen well above the amplitude of the sawtooth. This star has not previously been reported as variable; it is likely that it was missed in previous time-series observations of the cluster because it lies just beyond the traditional 15′ search field established by Eggen & Sandage (1964).

Montgomery et al. (1993) report colors of $B-V$=0.592 for this star while Sanders (1971) gives $B-V$=0.570. This range of colors corresponds to a dwarf star of approximate spectral type G0 or a late F giant (Cox 2000), but at M67's distance its

apparent magnitude suggests a dwarf. Furthermore, there is cause to believe that this star is an inertial member of M67; Zhao et al. (1993) find a 60% probability of membership for III28 based on their proper motion study while they calculate a probability of 94% from the data of Sanders (1971). Therefore, if other observations confirm the variability, this star represents an addition to the list of known variables presented here in Table 1.

As to this variable's type, note the semiregular period which seems to preclude any sort of eclipsing binary system. To try discerning the major period in the light curve, the period-folding algorithm built into the commercially-available image reduction software package MaxImDL (version 3.03) was used. The best period was empirically found by folding the light curve over periods ranging from a few hours to a few days. The upper panel in Figure 44 indicates a suggested period of 16.0 hours for this star; two peaks, one at 4.0 hours and another at 10.5 hours, are observed. However, when the data are folded on those periods in the center and lower panels, there is clearly no correlation. This fact supports the conclusion that multiple periods are superimposed on the signal in this star's light curve. Further analysis is required to separate those periods.

The possibility of multiple superimposed periods suggests multimodal radial pulsation. Given the star's spectral type and age, the closest match is the SX Phoenicis class of evolved pulsators, a subset of the δ Scuti family of oscillating blue stragglers.
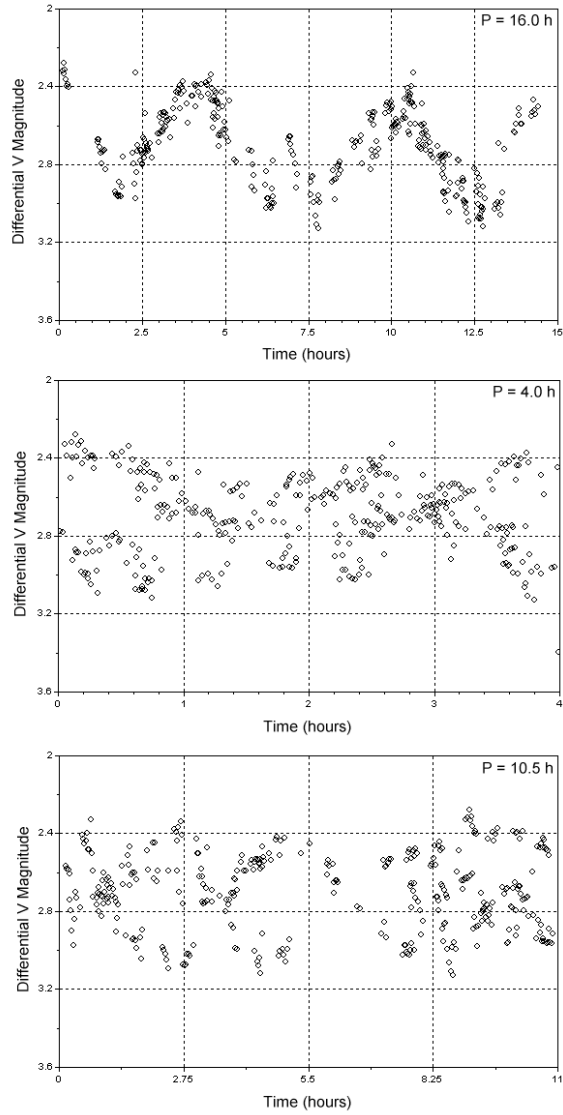
Fig. 44.— Periodograms for three potential periods of the star ES III-28. The panels show, top to bottom, periods of 16.0 hours, 4.0 hours, and 10.5 hours.

ES III-28 is of a slightly later spectral type than the latest SX Phe stars and its period longer than expected, but it fits the general profile of a radial pulsator with a semiregular period. In future work this star will be revisited to better fill in the gaps in the light curve presented here. Spectroscopic studies would help clarify its spectral

type and may resolve uncertainty as to which variable class it belongs.

8. Factors Limiting GNAT Photometric Precision

After a careful analysis of actual photometric data obtained with the GNAT prototype, a series of characteristics of the telescope, detector and site location was identified which will tend to diminish the system's ultimate attainable precision. Nearly all of these factors deal with effects which diminish the values of $N_\star$ and/or N_{sky}, a fundamental constraint on the S/N and error formulae of Section 4.1.1. This section is presented to help guide GNAT in designing future observing programs with the SciTech telescope or any other instrument it may choose.

8.1. Noise structure in object images

Despite the decision to avoid correcting object frames for bias and dark current, in order to prevent the stacking of changing noise profiles atop one another, the horizontal banding structure discussed in Section 5.3.6 remains evident in all object images. To quantify its effects "blank sky" portions of object images were sampled in order to determine the amplitude in counts that the structure presents relative to the background. The banding structure amounted to 6% to 9% of the background values, which themselves are typically 1% to 10% of the signal of most of the brighter stars on the frame. This structure will likely contribute relatively little to the magnitude determination error of the brighter stars, but may in fact dominate the error for the

very lowest S/N objects.

8.2. Non-Poissonian, variable background

Of all the sources of noise and, hence, photometry error identified in the data, the character of the sky background comes closest to rendering the images unusable. Noise models in virtually all widely available data reduction software assumes a Poisson-distributed background. The only suitable method of accounting for the nature of the background in GNAT images would be to write custom software to reduce the data using an empirical noise model that would account both for its time-variability and its statistics. But the need for any kind of custom components in the GNAT data pipeline defeats the purpose of its streamlined, "off-the-shelf" approach. As this problem is inherent to the camera and detector, it is this combination which requires the most serious further study to bring the background in the images it yields into line with software expectations. Uncorrected, this problem contributes as much as 10% error to time series data and effectively precludes achieving precisions in the 1% regime important to GNAT science goals.

8.3.   Poor guiding

The large positional drift from frame to frame in time-series observations, as previously described in Section 5.3.3, introduces random error into photometric observations by causing a given star image to land on different pixel clusters upon each integration. Error accumulates because of small pixel-to-pixel sensitivity differences which are not accounted for in typical flat field division, particularly given flats with color or illumination function-dependent responses. Twilight sky flats, such as those routinely used in the GNAT scheme, are the primary suspects in this case, for reasons given in the following section.

The reader is encouraged to take a second look at Figure 15, which shows the effect of the positional drift on the location of a given star on the detector array. In the case of ideal guiding, i.e., the centroid of a given star remains identical with the center of one pixel, the sensitivity issue becomes moot as the response is identical in every frame, given that all the object frames were treated with the same calibration images. While this approach does not account for intrapixel quantum efficiency variations, such effects are thought to be negligibly small in almost all cases. This ideal case is not very realistic; however, a much easier scenario to realize, especially given modern autoguiders, is that of one-pixel guiding in which the centroid of a star can be maintained *somewhere* within a one-pixel boundary throughout a time series. Other than the effects of intrapixel sensitivity variations, which even the best flat

field cannot correct for, the result is very nearly that of the "ideal" case. Variable seeing at most observing sites along with error-prone autoguiding capabilities often lead to 1-2 pixel guiding, which introduces another layer of sensitivity error, yet is not nearly fatal.

Figure 15 clearly shows that in the case of the GNAT prototype, the positional drift is generally much larger than 2 pixels. It is difficult to estimate the exact amount of uncertainty this effect introduces into photometry performed with this detector, given random low-amplitude sensitivity deviations from pixel to pixel. For an individual star this amounts to a relatively small contribution to the overall photometric error of the measurement. If such a star, however, were chosen as part of the ensemble, it would clearly impact the photometric error of all other stars on the frame referenced to the ensemble. Broadly, the effect would vary as the statistical average of all interpixel variations across the detector; the σ of a Gaussian fit to the distribution of pixel values in an average flat would be a good first-order approximation of this variation. In consideration of actual data, this method fails due to the large fraction of the chip encompassed by cosmetic errors, which being highly localized have the effect of distorting image statistics enough to prevent useful information being extracted from them. In principle, a subregion could be selected from an average flat containing only "good" data, but any contribution from large-scale illumination changes over the frame would be lost. Therefore the estimate of flattening errors given in the next

section may serve as some sort of first-order approximation to the photometric error attributable to poor guiding, but it should not be treated as anything but a rough estimate.

8.4. The use of twilight sky flats

An important aspect of performing high precision photometry on a variety of targets spread across a two-dimensional sensing array, as opposed to single channel photometers or PMTs, is the need for very careful field flattening. Manufacturing and raw material quality issues lead to individual pixels having slightly different quantum efficiency values than their neighbors. These variations must be corrected to some standard, such that the number of counts reported by any individual pixel can be reliably compared to others on a given frame – this is the essence of doing "good" differential photometry. An ideal flat field frame, therefore, is one in which each pixel is uniformly illuminated by a light source equal in spectral output to the objects being routinely imaged by the camera. Various methods of illuminating the detector to make flats are available, but GNAT has chosen to use twilight sky flats, which involve imaging of the twilight sky shortly after sunset or before sunrise. It is acknowledged that the whole issue of whether reliable flat fielding of CCDs can be performed remains controversial within the astronomical community, and all methods developed to date have some degree of associated problems. Therefore, in this section

the merits of twilight sky flat fields are considered in relation to other methods.

While the illumination function of a detector by the twilight sky can be reasonably good, the main problem with the use of twilight sky flats involves color terms. The spectral emission of stars involved in M67 observations are very different from the emission of a twilight sky illuminated by the Sun; therefore, the correction applied by the flat field frames to the object frames is strongly color-dependent. While all flat fielding methods suffer from some degree of color-related problems, this method is particularly susceptible. If the targets were highly localized within some sub-region of the detector frame, such imperfections in the flat field would not contribute as significantly to the final photometric uncertainty. The large-scale sensitivity gradients observed in normalized flats involve areas of broad spatial extent. However, with the goal in mind of generating light curves for as many stars in the cluster as possible, good flat field information is required over a very large spatial scale on the CCD. The problem of uneven illumination of sky flats prevents that information from being obtained.

To get an idea of the actual variation over a region of the detector free of visible cosmetic defects, simulating the expected results for a "clean" CCD, counts were examined in the subregion [84:145,116:182] of the average flat field frame generated for the night of 25 January 2001, shown in Figure 45. Pixel values in this subregion have a mean of 23,462 counts according to statistics generated with the task `imstat`.
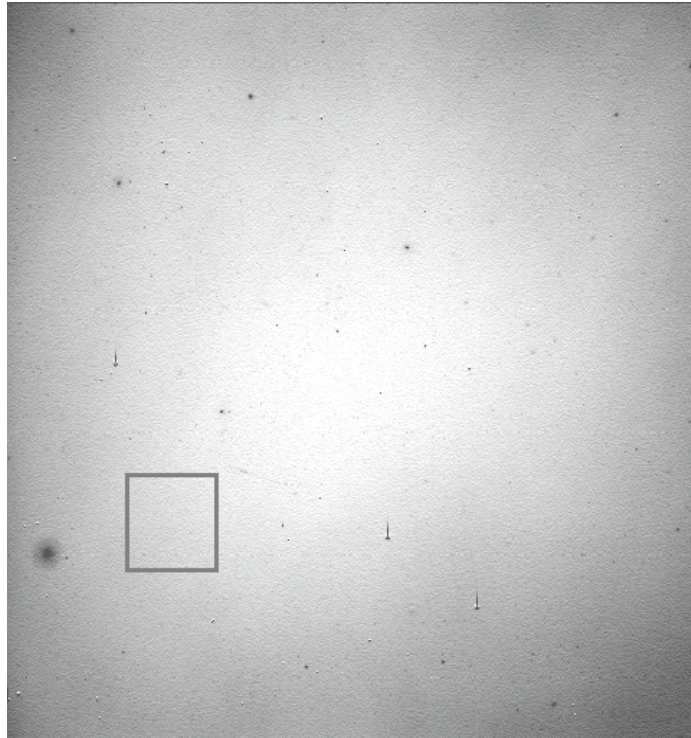
Fig. 45.— Average flat for 25 January 2001. The box at lower left indicates a sampling region for determining flat statistics.

Division of this region by the mean normalizes the pixels to unity; a histogram of values in this region after normalization is given in Figure 46. The statistics show good agreement with the mean value used in the normalization: this subregion has a mean of exactly 1. The histogram is more or less Gaussian in shape, expected for a random distribution of small-scale pixel response variations, and has a standard deviation of 0.012. This σ corresponds to a variation of approximately 1.2% over this region. If it is assumed that these statistics hold for the other parts of the flat field frame not besieged by charge traps or dust spots, then this percentage establishes a first-order approximation of the contribution of the flat to the photometric error.
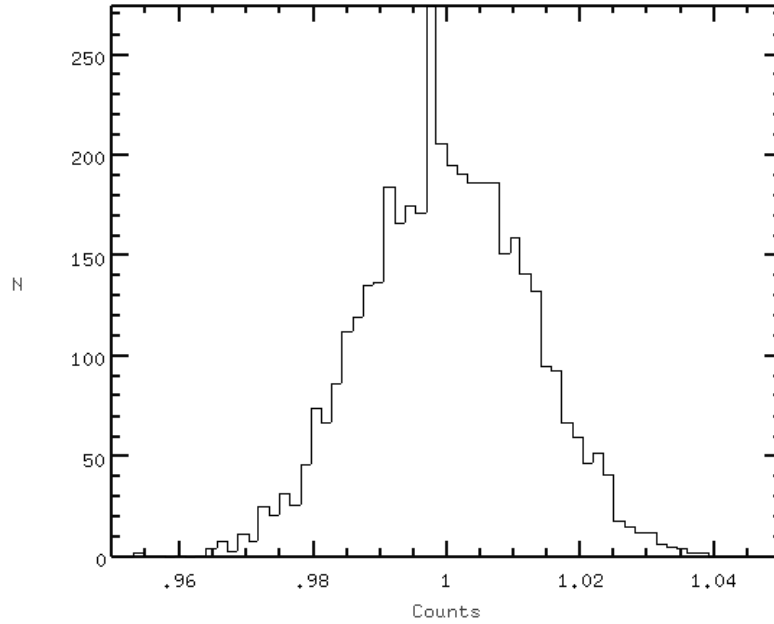
Fig. 46.— Histogram of pixel values in the subregion in Figure 45 after normalization to unity.

Examination of other similarly clean subregions on the frame supports this conclusion; values of 1.0% to 1.4% were obtained from varying points across the frame. Presuming uniformity of these results across the frame, this establishes a benchmark of between 10-14 mmag as the ultimate precision obtainable due strictly to flattening errors. This value compares well with the estimated photometric error of 4-10 mmag for the brightest stars on the longest co-added images.

There are few reasonable alternatives to twilight sky flat fielding. The small enclosure of the 0.5m telescope effectively precludes so-called "dome flats," typically made by imaging some kind of screen painted to have a fairly uniform spectral emission upon white light illumination. There is no suitably flat surface of sufficient size

within the enclosure to illuminate for this purpose. The only other serious contender is the process of taking "night sky" flats; this method involves pointing at the night sky in a region of few stars and taking several long exposures with small offsets in between. When the data are reduced, these object images are median-combined, which results in elimination of the stars from the resulting image. This image comprises a so-called "superflat" in which any spatial dependence of the illumination function of the night sky is eliminated because of offsetting the component images. There is a distinct advantage to this method, as it best matches the illumination function and color-dependence of the night sky background, but comes at the loss of the time required to take the necessary images. Because of this, alternative flat fielding methods were not investigated.

8.5.   Undersampling on nights of good seeing

Good sampling of the stellar PSF onto the two-dimensional detector array is critical in order to preserve the true shape of the PSF for modelling purposes. An improperly modelled PSF will result in flux either being gained or lost in the photometry aperture or the sky annulus, resulting in a systematic accumulation of photometric error dependent on sampling. To provide some quantitative understanding of this

problem, Howell (2000) defines a sampling parameter r

$$r = \frac{FWHM}{p},\tag{14}$$

where $FWHM$ is the full width at half maximum of the source PSF and p is the pixel size. As r is given as a unitless parameter, the FWHM and p must be specified in the same units. Values of $r \leq 1.5$ are considered undersampled. Given the relatively large (24μm$\times 24\mu$m) pixels of the SITe detector, under conditions of relatively good seeing we the images would be severely undersampled. However, given the average seeing FWHM of 2.6 pixels, the combination of routinely poor seeing at the GNAT prototype site and large pixels bring the data reasonably close to the Nyquist condition (FWHM$\sim$2$\times$pixel size). Howell further cites a condition of FWHM=2.355 pixels as critical sampling size for a Gaussian PSF, which we the data are comfortably close to.

Figure 47 shows the changing shape of the stellar profile over several hours of an average night from the GNAT prototype location. FWHMs were measured interactively by displaying a series of object images in Ximtool and using the IRAF task `imexamine` to fit Gaussians across the profile in both x and y (using the keystroke commands 'j' and 'k', respectively). The figure shows that significant changes of up to two pixels (3.64″ at the GNAT plate scale) in the FWHM of the stellar profiles can occur within a given night. The information from this figure can be used to
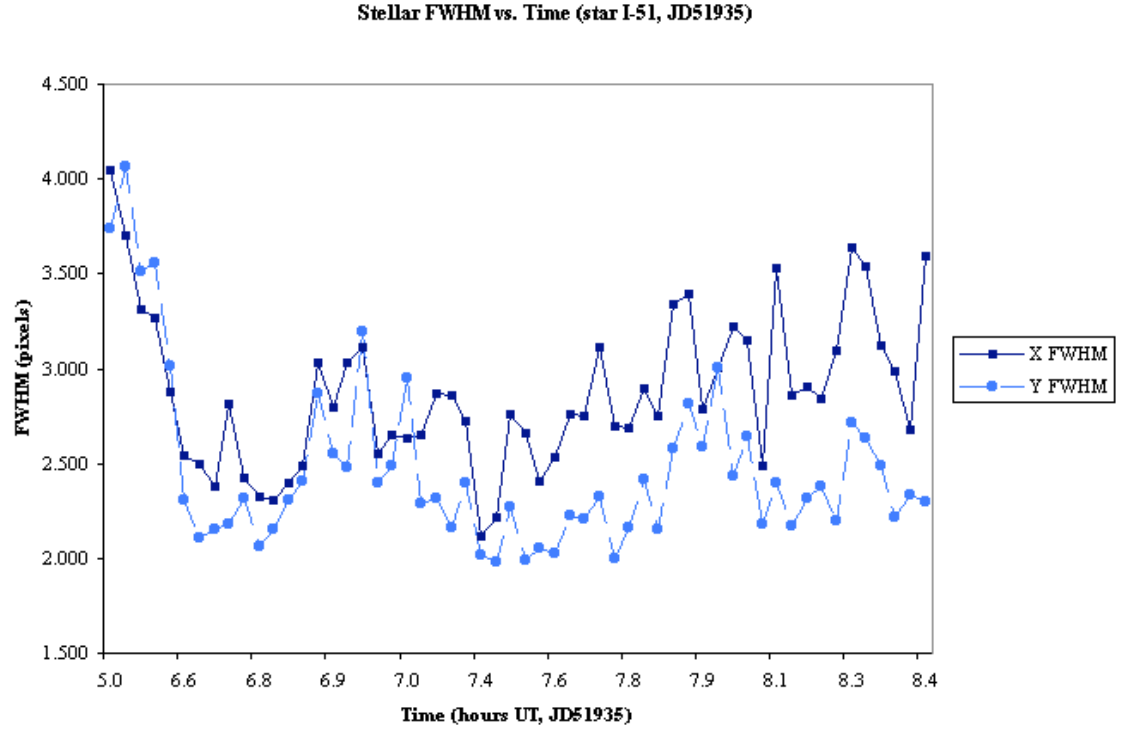
Fig. 47.— FWHMs (in pixels) in x and y of the stellar profile of star I-51 measured over the course of several hours on 25 January 2001.

compute the seeing by averaging the FWHM in the two directions; results are shown in Figure 48. One can see from the figure that the average stellar FWHM value is equivalent to seeing of $4.5''$ to $5''$. These values are typical for most nights in the data set.

Thus in most situations, the images are very near the critical sampling condition for the combination of site and detector characteristics. However, on nights of exceptional seeing, we images will definitely be undersampled and, consequently, the photometry will suffer. Using Howell's definition of undersampling, the threshold is
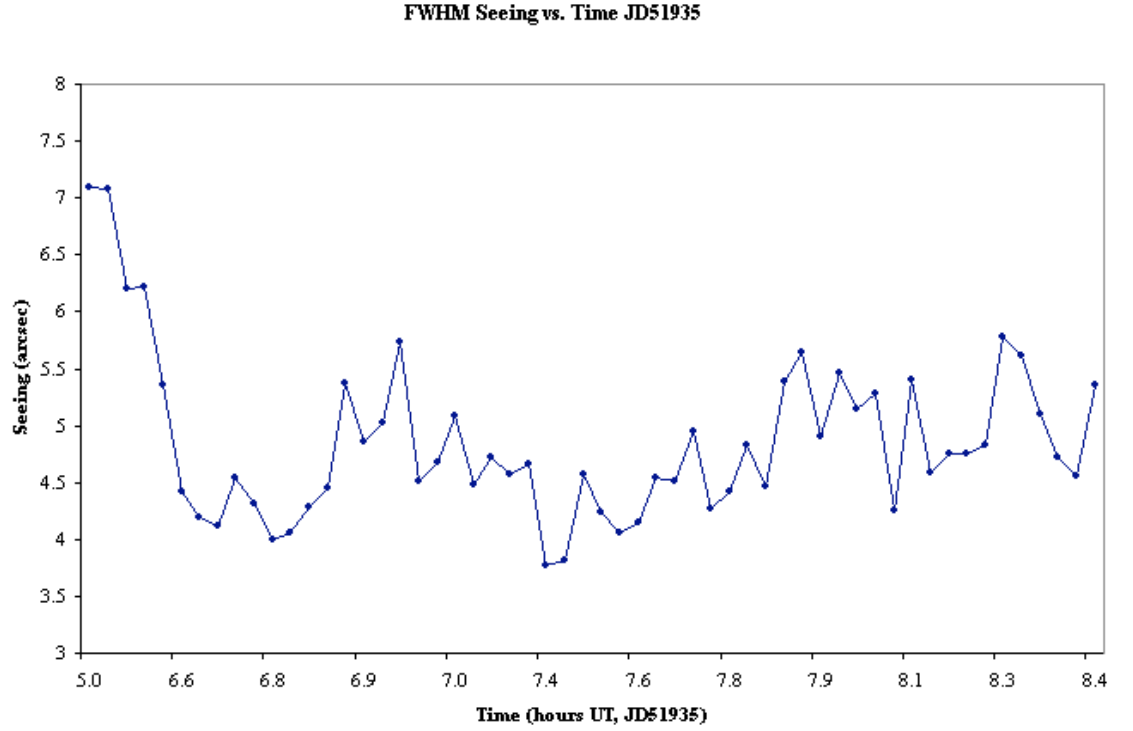
Fig. 48.— FWHM seeing (in arcseconds) as a function of time on 25 January 2001.

crossed when the seeing FWHM becomes $\leq 2.7''$. As the value of r approaches the

undersampling condition, standard data analysis methods will begin to yield increas-

ingly larger errors in determining stellar centroids as r decreases.

A solution to this and other problems would be to implement an autoguiding

scheme on the telescope that can, through software, actively calculate and track the

seeing changes throughout an observing night. In this manner, observations could

be suspended if the seeing dropped below the critical value of $2.7''$. Another simple

solution is to deliberately defocus the image under good seeing conditions to increase

the stellar profiles to a more acceptable size. Until such a program is in place, users of GNAT data for high precision photometric work are advised to monitor the FWHM of stellar images periodically while reducing and working with a data set to avoid the unpleasantries of undersampling.

8.6. Poor Charge Transfer Efficiency (CTE)

Any "spiking"[10] of star images, caused by poor CTE, saturation or any number of other effects, presents a serious problem to precision photometric measurements. These spikes will coincide, for some spatial distance, with both the photometry aperture placed around the star as well as the sky annulus beyond. If the spikes were uniform in counts and spatial extent, their contribution within the photometry aperture would be mitigated by subtraction of an equal amount of flux from the sky annulus. However, there is significant variation in three dimensions of these spikes, particularly along the intensity axis. This consequently leads to an overestimation of the stellar flux within the photometry aperture and a disproportionate estimate of the sky background. The problem becomes more pronounced when dealing with brighter stars, as the profile and length of the CTE spike appears to be very different from those of the fainter stars, whose spikes become quickly drowned in the background.

---

[10]Spiking is defined here as extension of the wings of a stellar profile along straight lines directed radially outward from the centroid of a star.

It should be reiterated that this is a treatable disorder on the part of the detector electronics. With some fine adjustment, the CTE can be raised to a more acceptable level, which we is enthusiastically recommended.

8.7.   Charge traps that do not clean

The charge traps discussed in Section 5.3.5 yield an effect similar to the CTE spikes of the previous section, but are spatially oriented along columns rather than rows. There exist three very strong traps on the SITe detector in the GNAT prototype which do not "clean", i.e., do not become filled with a pedestal level of charge upon readout, thereby in a sense "filling the hole". A star falling exactly on the pixel location of the charge trap, however, would suffer an irreparable loss of signal which should immediately discount its selection for photometry in such a frame.

A possible solution to this problem that has been suggested is to create a so-called "bad pixel mask" which is applied to object images and essentially negates pixels plagued by problems like charge traps and surface dust. This method was not investigated for the purposes of the study at hand.

8.8.   Flaws at the detector surface

Like the isolated charge traps of the previous section, shadows from dust particles on the detector surface (see Section 5.3.4) affect only a very limited area of the detector and thus are not frame-wide effects. If the telescope pointing and guiding were better and the frame-to-frame drifts (see Figure 15) not as large as they are, this problem could be dealt with by simply eliminating the stars situated on those spots from the list of program objects. The loss of a few stars is balanced by the fact that their photometric errors would be much larger than others in "clean" regions of the chip. This is due to a fundamental reduction in the photon flux reaching the pixels under the dust particle; a simple reduction in $N_\star$ affects the resulting S/N of a star rather strongly as noted in Section 4.1.1.

An examination of Figure 18 allows an estimate to be made of the error induced by a surface irregularity such as the large antireflection coating defect mentioned earlier at (99,125). Taking the maximum and minimum values across the plot gives a decrease of light of 7.7% from the edge of the profile to the center. Assuming a Lorentzian profile (Howell & Merline 1995) for a star which might fall on top of this spot and the Gaussian profile of Figure 18, merging the two results in a stellar profile still generally Lorentzian in shape. The width of the Lorentzian tends to become narrower in proportion to the depth of the Gaussian "well" underneath it. Evidence for this effect can be seen in Figure 49, where it has been simulated by

adding sections from the same image containing an antireflection coating flaw (see

leftmost circle in Figure 17) and a moderately bright star. The leftmost frame in the
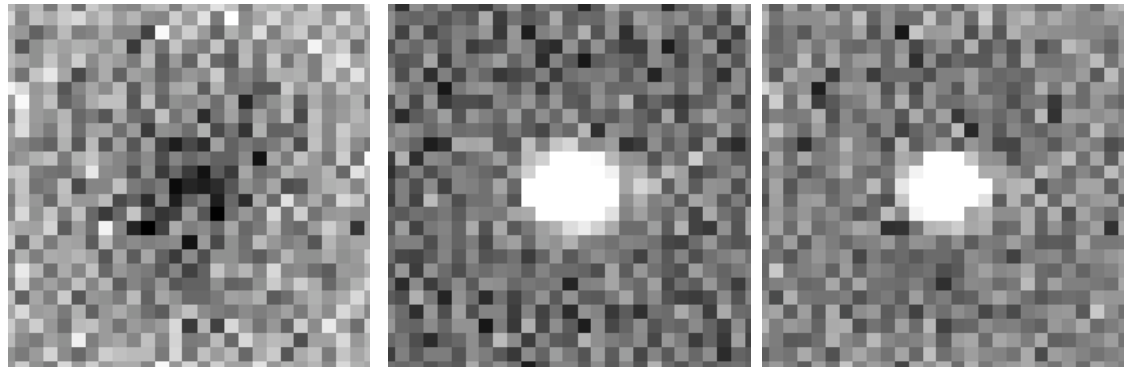
Fig. 49.— Illustration of signal loss due to superimposition of a star profile with a
large antireflection coating flaw at the surface of the detector.

figure is the section [77:103,121:147] taken from the object frame P51960FI taken on

the night of 20 February 2001, comprising a 44x44 box centered on the flaw. The

middle image is the section [86:112,130:156] centered on a bright star approximately

40 pixels away from the spot. It has the same dimensions as the AR flaw box in order

to facilitate 1:1 image addition. The center of the box for the flaw was determined

visually by identifying the lowest pixel values in the spot; the star box was defined

with the centroid of the star coinciding with the center of the box. To obtain the

centroid, a first guess at the position was made using the cursor in Ximtool and these

coordinates saved to a file. The IRAF task `imcentroid` (see section 6.2.3) was used

to geometrically determine the centroid at [108.032,134.070] from the initial guess.

For the final frame in the figure, the first two frames were median combined with the

IRAF task `imcombine`. This final image shows a marked decrease in the size of the

PSF. This example has the additional effect of raising the background by essentially doubling it, but because the star is so far above background, the decreased PSF effect is real. The AR flaw changes the value of $N_\star$ in two ways: first, by making the PSF smaller, resulting in fewer pixels containing signal from the star ending up in the photometry aperture, and second, by actually increasing the number of incoming photons reflected off the detector surface.

The S/N of that star will decrease in accordance with the results of Equation 3, consequently raising the photometric error of the observation. To illustrate this, aperture photometry was performed on the center and right images in Figure 49 using an aperture of 6 pixels and a sky annulus with inner and outer radii of 7.5 and 10 pixels, respectively. The presence of the AR coating defect in the second image resulted in a reduction of the flux within the photometry aperture from 4267.438 to 1660.87 counts, raising the reported photometric error from 0.026 mag to 0.046 mag. Note that this $\Delta\sigma_m$=20 mmag result is valid *only* for the *largest* (and presumably darkest) spot on the frame and merely sets an upper limit on the photometric error contributed by this phenomenon. However, there are approximately 20 other such spots, generally much smaller in radius but still larger than one pixel, scattered over the frame as visible on a typical flat field image. Many dozens or hundreds more exist at the 1-2 pixel level and in principle could be dealt with as "bad" pixels in the sense that a bad pixel mask could be constructed to smooth over these spots by substituting

in the average of pixels surrounding the bad ones in the flats. This approach is still somewhat risky, because even very small dust spots will still effectively lower $N_\star$, but not to the extent reported in the previous example.

Reduction of $N_\star$ is not the only potential contribution to photometric error here. The narrower Lorentzian profile under a dust spot will have the effect of making the PSF smaller and leading to undersampled conditions. This raises the prospect of combining multiple forms of error into a single observation, further degrading the value of stars which fall on these spots. Such an effect would depend strongly on the magnitude of the star falling on top of the spot, as the smaller PSFs of fainter stars became undersampled much more quickly their brighter compatriots.

The only clear way to avoid this problem is the complete rejection of any star falling partially or completely under a ≥ 2 pixel spot from the time series. Again, because of guiding errors, which stars are affected by the spots will change almost on a frame-to-frame basis leading to random dropping of points from light curves. The loss of $\leq 1\%$ of the program objects on a given GNAT frame is acceptable in consideration of the photometric error that keeping such stars would transmit to their light curves.

8.9. Short exposure times

The aforementioned shortcomings of the SciTech telescope mount and guiding are well-known enough in the anecdotal sense to constrain integrations made with the telescope to short intervals. This is done to mitigate the effect of guiding errors on the resulting object images, as fewer errors tend to accumulate in shorter integration times. Alas, as discussed in Section 5.3.3, many of these errors crop up in GNAT frames regardless, resulting in a high rate of rejection of raw object frames (see the following section). Seeing conditions at the site (see Section 8.4) are sufficiently poor to eliminate the worry of undersampling; in fact, longer exposure times, leading to a greater degree of "seeing blur", serve as further insurance against undersampling on nights when the seeing is better than usual. Since the photometry discussed in this work was performed on point sources rather than over the surfaces of extended objects, seeing blur is less important in the degradation of results. The fact remains, in any case, that shorter exposure times ultimately mean lower values of $N_\star$ regardless of whether or not frames are co-added. This not only restricts the range of stellar magnitudes accessible in a single integration, but represents another fundamental limit to the obtainable precision of the system.

8.10.   Large data rejection rate

Finally, there exists a source of error which has more to do with the continuity of the time series (and prospects for the science objectives it is sensitive to) than the actual photometric measurements themselves. Rejection of images from the set on the order of 30% (see section 5.3.3) may result in a significant temporal undersampling of light curves, consequently increasing the noise level in power spectra taken of those light curves to look for periodicity. Rather than affecting the error bars on individual data points, the data rejection rate influences the error bars of the time series *itself* for a given star. It is important to make this distinction, because under the best of circumstances, when the photometric precision is highest on individual data points, poor sampling of data leading to a large time series error can still aversely affect GNAT science goals. Again, replacement of the telescope mount – which would practically solve the pointing and tracking error problem – is a useful remedy.

9.   The Future Of High Precision Photometry With GNAT

The success of any scientific program to be carried out with the GNAT proto-type telescope hinges on the reliability of its results in terms of both precision and accuracy. Both are strongly tied to the error parameters identified and discussed in this work; as a concrete example, calibrations of instrumental magnitudes to an absolute scale, defining the accuracy of a system, depend inevitably on the precision to which photometric standard stars can be observed and measured. In this section, the precision of actual data taken with GNAT will be compared to the requirements of some of the proposed scientific objectives in an effort to answer the ultimate question: can this telescope, in its present incarnation, perform to expectations?

9.1.   Extrasolar Planet detection among M67 stars

Of primary interest is whether the SciTech telescope and Tucker camera combination can observe the signature dimming of light from stars due to the transits of extrasolar planets; Figure 50, adapted from and used with the permission of Howell et al. (1999), shows clearly how detection is a strong function of photometric precision. The percentage by which the light drops during a transit event is directly correlated to the sizes of both the star and planet, as the diminution of light depends on the portion of the surface area in projection which is obscured by the planet. The
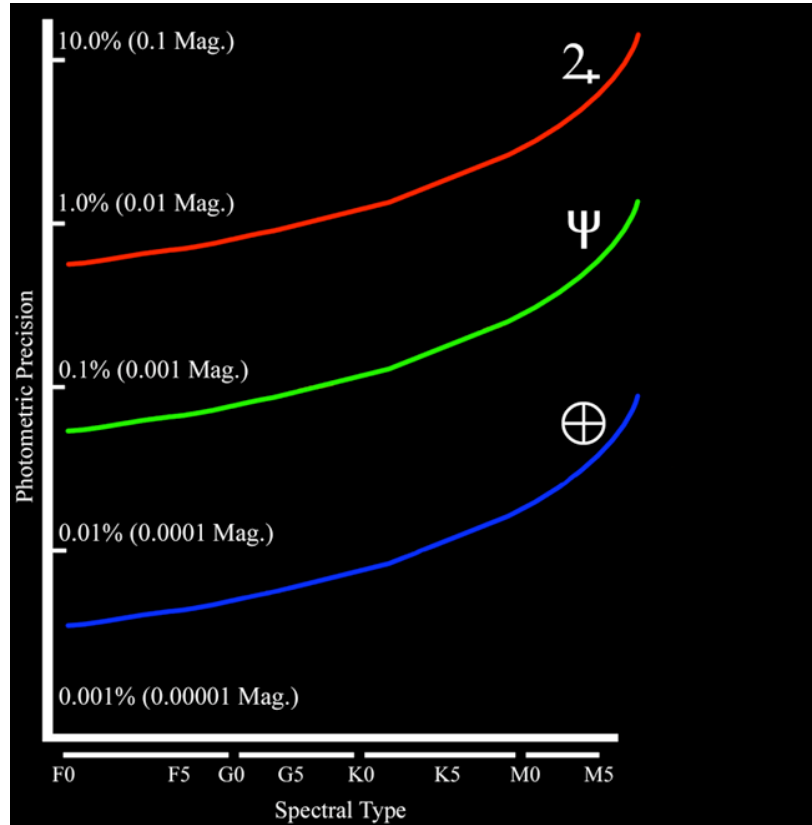
Fig. 50.— Photometric precision thresholds for detection of transits events involving extrasolar planets of varying size ("Jupiters", "Neptunes", and "Earths") as a function of stellar spectral type.

lines representing detection thresholds for planets of various sizes were calculated on

the basis of knowing sample radii for Main Sequence dwarf stars and the percentage

obscuration of each for the various planetary radii. There is some implied leverage

around the plotted lines to allow for small differences in the sizes of either the planets

or stars.

Where on this diagram does the SciTech telescope/SITe detector combination

fall? The photometric precision of several stars (IV77, IV30, I5, I46, III2, I38, I62

and IV18, in the notation of Eggen & Sandage (1964)) in the m_V=12 to 14 range, determined empirically by the IRAF task `qphot`, is plotted as a function of their magnitudes in Figure 51. Additionally, the figure has been overplotted with a fit line based on the error model built into `qphot`,
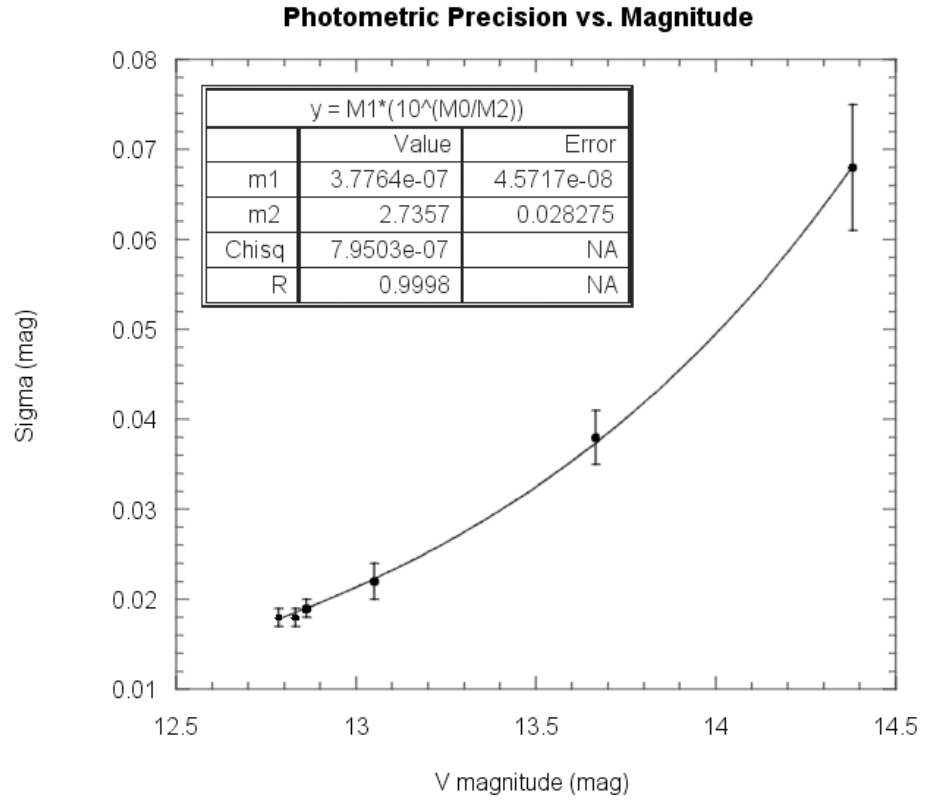
Fig. 51.— Photometric precision of the GNAT prototype as a function of stellar magnitude.

$$\sigma_p = \frac{1.0857 \cdot err}{flux} \qquad (15)$$

where

$$err = \sqrt{\frac{flux}{epadu} + area{\cdot}\sigma^2 + area^2{\cdot}\frac{\sigma^2}{nsky}}$$

(16)

In the definition of err, $flux$ is the flux from the star being observed falling within the photometry aperture, $epadu$ is the gain in electrons per ADU, $area$ is the area of the photometry aperture, σ^2 is a term representing the variance of all the noise terms considered in Section 4.1, and $nsky$ is the number of pixels in the sky annulus. The model fit to the data is based on Equations 14 and 15, along with the definition of the magnitude scale,

$$m = -2.5 \log_{10} \frac{I}{I_0}$$

(17)

where I (equivalent to $flux$) is the irradiance of the star at the surface of the earth in W m^{-2} and I_0 is the irradiance of a zero magnitude star at the surface of the Earth, also given in W m^{-2}. Rearrangement of this equation and considerations of Equations 14 and 15 resulted in a model of the form $\sigma_p = A{\cdot}10^{\frac{m_V}{B}}$, with A and B as free parameters. A was expected to be of order the value of I_0 ($2.8{\times}10^{-8}$ W m^{-2}) and B approximately 2.5 with consideration allowed for the other constants floating about in the above equations. A and B were determined in an iterative manner using χ^2 minimization, and found to be A=(3.2108$\pm$0.6197)$\times10^{-7}$ and B=(2.7001$\pm$0.0442). As is clear from Figure 51, the fit is very good and appears to model the trend well.

According to this fit and the contents of Figure 50, the GNAT prototype reaches the threshold of detection of Jupiter-sized objects near m_V=12 for the mid to late spectral type stars of M67. Comparison with the cluster magnitude histogram in Figure 3 shows 38 candidate stars around which Jupiters might be detected. This is a mere 2.6% of the total number of stars in the central region of M67. Candidate star numbers decrease rapidly as the radius of detected planets decreases; none of the stars in Table 3 of Montgomery et al. (1993) is sufficiently bright to reach the 1 millimag precision threshold with the GNAT prototype. Making some assumptions about the nature of the stars in M67 and the planets which may orbit them, the likelihood of observing a transit at any given instant can be calculated. The following analysis proceeds as in Howell et al. (1999).

First, given that M67 is an evolved open cluster, assume that all 38 of the stars above m_V=12 are solar-type or later dwarfs. It is acknowledged that this is not an entirely reasonable assumption, since the brightest 1% of stars are certainly giants. In the case of the stars belonging to M67, this would account for at least 14 of these 38 brightest stars. With larger radii than dwarf stars, planet transit durations would be longer; however, this does not change the probability of observing a transit in the first place. That probability is determined only by the number of on-sky hours and the period of a planet's orbit. There are some additional concerns regarding the inclination of planetary orbits, in that a grazing transit would present a different light

curve from a more direct passage across the face of the host star. However, for the moment the concern is only to calculate the chances of observing any transit event.

Next, assume that each of these stars has one (and only one) planet like 51 Peg, with an orbital period on the order of a few days; given random inclinations of these planets' orbits to the line of sight, approximately 10% will lie within the requisite 5° such that they will transit the star, leaving 4 candidates. The transit durations would be on the order of a few hours. If ∼50% coverage is achieved on nights during the approximately 6-month observing season of M67, this leaves about 90 nights averaging perhaps 6 hours of on-target observations per night for a total of 540 hours. If each planet has an orbital period of, say, 5 days (120 hours), this assures detection of at least one transit each within the 6 month observing season. On any given night, the chance of seeing a transit is 6÷120 = 0.05, or approximately 5%, keeping in mind that this value is highly sensitive to the period of the planet. Therefore, on average, a transit ought to be seen every twentieth consecutive observing night.

This analysis suggests that GNAT could, in theory, detect all the so-called "hot Jupiters" around the brightest ∼3% of stars in M67, contingent on the connotation of the term "detect". The hot Jupiters, being in very short period orbits, typi- cally present transits lasting 2-3 hours; the prototypical planetary transit system, HD209458, has a 3.1 h transit duration (Henry et al. 2000). These systems also have relatively fast ingress/egress times on the order of ≤1 h. Even with the poor temporal

sampling of the GNAT prototype, in principle a large part of the $\sim$0.5 h ingress or egress time (Jha et al. 2000) of a transiting system like HD209458 could be observed, and a complete transit could be recorded within one observing night. At m_V=+7.65 and a transit depth of approximately 0.017 mag, Figure 51 suggests that transits of the planet around HD209458 are within the capabilities of observation by the GNAT system.

The details of what constitutes a positive photometric transit "detection" are still the subject of debate within the ESP search community. Even the existence of the sole known planet observed by photometric transit (around HD209458) was previously known from the radial velocity studies of Vogt et al. (1994) and Baranne et al. (1996). Despite concerted transit searches in recent years involving hundreds of thousands of stars, no planets have been discovered outright by this method. A significant quantity of candidate events have been observed, which require additional followup efforts to discern the definite signature of planets from other phenomena such as starspots and orbiting brown dwarfs. Giampapa et al. (1995) comment on the ambiguity of "transit" results and suggest both optical and near-infrared observations as a means of distinguishing planets from spots. Their analysis indicates that planets detected by photometric transit will most often be discovered orbiting cool M dwarf stars. In this case, spectroscopic studies may well be required to distinguish between jovian-sized planets and brown dwarfs. Thus if ESP transit searches are to be a

primary operational program in future GNAT efforts, the need is evident for followup observations of transit candidates in either the near-infrared or spectroscopic domains.

Provided that observations were made with good contiguity over these time scales, detection would be certain within the specified observing season. The criterion for a truly positive "detection" of a hot Jupiter is observation of both the transit ingress and egress within a single observing night; the definition is strict to prevent other effects causing short-term variation in the observed output from a star to masquerade as planets when no transit-causing planets are in fact present. Given the large data rejection rate and details of the duty cycle, such a scenario is impossible with the current GNAT prototype. The telescope is neither on target long enough to see a complete ingress or egress, except for the few stars in the overlapping of regions in Figure 26, nor is the continuity of data assured within one duty cycle. Thus while independent detection (i.e., observation of a complete transit, including both ingress and egress) appears impossible with GNAT, transit candidates could be easily identified even with partial data for ingress or egress, allowing other instruments to make followup observations.

9.2.   Future GNAT efforts

As of this writing (mid-2002), the philosophy and approach taken by GNAT to the problem of deploying a truly global network of automated telescopes in a cost-

effective way has changed. Given that pointing and tracking constitute the most problematic aspects of the telescope evaluated here, the "next generation" of GNAT telescopes is likely to exploit the fixed-pointing nature of drift scanning. A prototype system developed by Roy Tucker is now under testing by GNAT as a possible successor to the SciTech prototype (Tucker 2002). The Moving Object and Transit Event Search System (MOTESS) consists of three 14-inch Newtonian telescopes fixed in pointing near the celestial equator and is equipped with drift scan-mode CCD cameras. This design allows for efficient survey operation (12 square degrees of sky per hour to unfiltered magnitude 20), but does not necessarily provide the capability needed to observe small targets away from the equator with sufficiently high temporal cadence. This may bring about a shift in the GNAT science goals to accommodate this new observing scheme.

10.   Review Of Findings And Recommendations

In this work the results of an extensive survey of factors limiting the achievable photometric precision of the GNAT/SciTech prototype telescope have been presented. This effort involved investigations of telescope systems mechanical, electronic and computer/software-related in nature. Suggestions have been made during this presentation of ways the precision can be improved with modifications to these systems.

Ten factors ultimately limit the photometric precision which can ever be obtained with the telescope as it is currently configured. There is evident, structured noise in all images generated by the telescope which changes in both frequency and scale, rendering it non-removable through standard CCD reduction techniques and the calibration images they require. The character of the noise originating in the Tucker camera is non-Poissonian and varies in strength in a spatially-uniform manner throughout the night. The remarkably poor pointing and tracking scheme employed in this telescope causes serious positional drifts of individual stars on successive object images, introducing error from pixel-to-pixel sensitivity variations not accounted for in flat fielding. The flat fielding process itself (i.e., using the twilight sky for an illumination source) results in "bad" flattening of object images because of color differences between object and flat field images and an added component of sensitivity to changes in the illumination function. The potential for undersampling of stellar profiles on nights of better-than-average seeing, while not anticipated to be a frequent

occurrence, is nevertheless unaccounted for in normal telescope operations. The low (but correctable) measured values of charge transfer efficiency on the SITe chip in the telescope's CCD camera leads to 'spikes' emanating from stars which interfere with aperture/PSF photometry. Cosmetic defects on the chip, in the form of charge traps and dust and other flaws at the array surface, render localized regions of the chip virtually useless for photometric applications. The short integration times necessitated by the telescope tracking problems lead to a fundamental diminution of the parameter $N_\star$, the number of photons detected in the signal of an object, a value tied strongly to models of photometry error.

An additional effect, correlated to the error of the time series in light curves generated with GNAT, is caused by the large temporal data rejection rate, again due to the pointing and tracking errors. This effect represents a significant obstacle to GNAT science goals as it undermines the effort to obtain and assemble time series observations. It further presents a roadblock to the synoptic observing programs seen as among the long-term science goals of the project.

Improvements to the existing telescope – or its outright replacement – are suggested in order to maximize the attainable photometric precision, allowing for reliable observations of increasingly fainter targets. Most important, if the telescope is to remain otherwise intact, is replacement of the existing mount and drive system. Short of such drastic action, refinement of the telescope pointing and tracking models come in

a distant second as possible remedies. No significant flaws were found in the telescope optics, but consideration should be given to updating the detector to a higher-grade CCD chip. Such a chip would have fewer of the cosmetic defects which trouble the current SITe chip. In the absence of such a replacement, the CTE should be increased by adjusting clocking voltages in the detector electronics as described previously, and the source of the structured noise should be tracked down and eliminated.

On the whole, the GNAT prototype telescope was found minimally useful given the stated science objectives of the project, yet the goals are sound in consideration of this aperture class of telescope. With careful attention to details and further expenditure of resources, some of these objectives may finally start to be realized.

A. The GNAT Data Reduction Pipeline

A.1. Raw data reduction

This discussion assumes that the user is provided with a set of raw images from the GNAT 0.5m telescope and is familiar with both UNIX and the IRAF environment (e.g., how to invoke packages, how to edit parameter files, etc.) For file-naming conventions, note that "JDXXXXX" is taken to represent the five digit Modified Julian Date by which an individual night's images are identified.

1. **Copy the raw images from the data CD-R to the user's home directory** with the UNIX command

cp /mnt/cdrom/*.fts /home/user

2. **Change the file extension on the raw images from .fts to .fits**. This must be done because the three-letter FITS extension is not recognized by IRAF, and is done with the UNIX command rename:

rename .FTS .fits *.FTS

(NOTE: rename is a UNIX command and will not work by itself in IRAF without use of a trailing "!" before the command at the `cl` prompt.)

3. **Start IRAF.**

cl

4. Change the pixel type of each image to "real" from "short".

chpix *.fits *.fits "real"

This step is recommended[11] as early in the process as possible to reduce the contribution of quantization noise to the final photometric product

5. Add certain image header parameters[12] required in the reduction process. These can be added individually by hand with the hedit command, or they can be automatically added by using the script addheaderparams.cl.

cl < addheaderparams.cl

The reader will note that the values of TRIMSEC and BIASSEC are predetermined; beware, however, that these values were current for the camera configuration as of March 2001; should the camera aspects change (resulting in a different pixel range

---

[11]see Newberry (1999), p. 82

[12]This step will eventually no longer be necessary. The current GNAT camera control software does not contain the provision for adding these header parameters, but a future version of the software is planned which will. The user may wish to check for the presence of these parameters before performing step 5 by choosing any image in the set, here referred to generically as *image.fits*, with the command

imhead image.fits l+

This will display a list of image header parameters which can be checked for GAIN, RDNOISE, etc.

for these two header parameters), the reader should fill in the state pixel range in addheaderparameters.cl by hand.

6. View each image in the set individually to determine whether it should be accepted for further reduction or rejected due to tracking errors native to the GNAT SciTech telescope mount/drive design. This is done via an IRAF script viewimages.cl:

    list = "all.list"
    while (fscan (list, s1) != EOF) {
    disp (image=s1,frame=1,zr+,zs+)
    sleep 10
    }

The script requires as input a list of images called all.list which can be assembled with the command

<div align="center">

sections *.fits > all.list

</div>

The script is run by typing

<div align="center">

cl < viewimages.cl

</div>

Each successive image in the list is displayed to XImtool and remains on the screen for 10 seconds before the next image on the list is displayed. It is recommended that, before beginning this step, the user obtain a hardcopy of all.list in order to make notes as to which images are to be kept and which rejected. Alternately, a hardcopy of the ATIS file for that night's data can be used for the same purpose. These notes are important for the rejection process of Step 7.

7. **Delete images rejected from the data set in Step 6.** With the list of images in hand, copy all.list into a file called delete.list:

cp all.list delete.list

Edit this list by hand with an editor (e.g., vi or emacs) such that only the images to be rejected remain; that is, delete each line containing the name of an image which is to be kept. Then delete the images left in the list with

imdelete @delete.list ver-

(NOTE: the "@" symbol tells IRAF that the file named immediately after the @ is a list of files it is to read in executing the command.)

8. **Add additional header parameters relevant to photometry.** These are, again, not automatically added by the camera control software and so must be added

manually. A script has been written for this purpose, called hupdate.cl (see Appendix A). Invoke the script with

cl < hupdate.cl

9. **Convert files from FITS format to IRAF format.** The next step in the reduction process (ccdproc) includes file format conversion but results in awkward file names (e.g., adding "0001" to the end of each file name). It makes most sense to convert them ahead of time so that the file naming convention native to GNAT can be retained. First form a list of file names containing FITS extensions:

sections *.fits > inlist

Open the list using the vi editor and edit out the FITS extensions, replacing them with the .imh extension native to IRAF:

:1,$ s/.fits/.imh/g

All the entries in the list containing ".fits" as the extension will automatically update to ".imh". Save the list and exit using:

:w outlist

To convert formats, use the IRAF task `rfits`:

rfits @inlist @outlist

Unless messages are suppressed, the screen output will echo the results of each file conversion. As a last step, get rid of the original FITS files with the command:

imdelete @inlist

10. **Begin calibrations.** First enter the CCDRED (CCD Reduction) package with the following commands

noao

imred

ccdred

Run the setinstrument task to setup the parameters for the calibrations. Type "direct" when prompted for the Instrument ID. The user is then allowed the edit the parameters for setinstrument; make sure the parameter pixelty is set to "real real"; no other adjustments should be necessary. Do a CTRL-D to exit the editor.

The user is next taken to the parameter editor environment for the task `ccdproc`. The only changes the user might have to make are to parameters controlling the application of certain corrections in the process; at this stage, make sure flatcor=no, overscan=yes and trim=yes. This sets up ccdproc for its first pass over the data, where only trimming and biasing is performed.

11. **Perform the first pass of ccdproc to trim images**. First edit the parameter file for ccdproc with the following command:

epar ccdproc

Set "input" to "*.imh" such that all images are processed, including objects and flats. Make sure "overscan" and "trim" are set to "yes". Further down, where it asks for trim and overscan sections, enter "image" for both (the values were set previously and written to the image header). Do a CTRL-D to exit the parameter editor. At the prompt type

ccdproc

The parameter editor will come up again. Type CTRL-D to begin processing. An xgterm window will pop up with a column plot through the overscan region of the first image along with an overplotted line representing what IRAF thinks is the best straight-line fit to the data. For flats, this line should be horizontal; object images are typically sloped lines. If the data are sloped and the line is horizontal, do a :o 2 in the xgterm window and hit f to re-fit the line. Once you have a good match, hit q to resume processing. When it asks you in the IRAF window if you want to view the overscan for image blah-blah-blah, hit RETURN (defaults to 'yes'). After examining a couple of the plots, the fit will be consistently good and you can allow IRAF to do

the rest. The next time it asks you if you want to examine the overscan region, type NO (this must be in all caps) and it won't bug you again for overscan verification. Once complete, all your images will have been trimmed to the defined working size.

12. **Combine the flat field frames to an average flat.** Edit the parameter file for `flatcombine` and again make sure combine=median, reject=minmax, ccdtype=dark, rdnoise=RDNOISE and gain=GAIN. Combine the flats using

<div align="center">

flatcombine input=F*.imh output=flatXXXXX

</div>

The resulting average flat will have the filename *flatXXXXX*, where "XXXXX" is the five-digit JD number of the observation date.

13. **Perform the second pass of ccdproc.** In this final processing step, only flat field division is performed. Do a

<div align="center">

ccdproc input=*imh flatcor+ flat=flatXXXXX

</div>

Your images are now properly calibrated for photometry. If you intend to format them for archival to CD-R, for example, follow the remaining instructions:

14. **Convert images back to FITS format for long-term archival.** This is done mainly as a convenience to other users who may not be using IRAF for the analysis of reduced data. It is also conventional to rename the images to indicate they have been

calibrated, in order to distinguish them from the raw images they originated from.
A convention of adding an underscore between the JD number and the two-letter
sequence designation in the filename was established. To begin with, form an image
list of the IRAF images:

sections P*.imh > inlist

Edit this list to change the format to FITS and add the underscore to the file names:

vi inlist

:1,$ s/.imh/.fits/g

:1,$ s/XXXXX/XXXXX_/g

Save the resulting list to the new name "outlist":

:w outlist

and exit the vi editor. Now convert the images in "inlist" to the images in "outlist"
using the IRAF task `wfits`:

wfits @inlist @outlist

15. **Convert the average flat field image to FITS format for archival.** This is
preserved as a separate step because of the bulk file naming convention carried out in

the last step; since the average flat has the file name "flatXXXXX", the replacement

algorithm in the vi editor will place an underscore at the end, causing the IRAF file

flatXXXXX to be renamed flatXXXXX_.fits. To avoid this minor unpleasantry, carry

out the following command:

wfits input=flatXXXXX.imh output=flatXXXXX.fits

16. **Note the following with respect to which files are archived to CD-R**: To maximize the utility of the archived data product, the following set of files

from each night is written to CD-R:

All object images (P*.fits)

The average flat field image (flatXXXXX.fits)

all.list

delete.list

The ATIS file for the night (JXXXXX.doc)

A.2. "Spreadsheet reductions"

The simplest method of manipulating the type of tabular data generated with

the photometry software is via use of a spreadsheet. While a more time-consuming

process, it offers an important advantage in the portability of this data reduction

scheme: no standalone programming is necessary. Specifically, a combination of the commercial Windows spreadsheet Excel (part of the Microsoft Office suite of business applications) and the open-source Linux-based spreadsheet distribution Gnumeric was used. In brief, the process consists of choosing a reference frame to register all other frames to, calculating coordinate shifts directly from the images themselves, applying those shifts to the coordinates of objects found on those images and finally, matching coordinate entries star-for-star across adjacent images. This process is illustrated in a more concrete way in this section with a practical example and screen captures from the spreadsheet software.

The `txdump` output files must first be imported into the spreadsheet environment. Excel and Gnumeric each has a filter for converting fixed-width or delimited tabular data into the row-column cell format of a spreadsheet; the photometry results files consist of delimited text with one or more consecutive whitespace characters as the delimiter. Some identifying information is added to the first row of the sheet (field and MJD number) as well as to the rows immediately before the data begin (image file name the results are taken from, column headings); the first few rows and columns of a typical sheet are shown in Figure 52. The first two columns labelled "Reference Coords" are the x and y coordinates, respectively, of the objects identified on the chosen reference frame from the first night of observations (pass number two over field "A" on the night of MJD 51935). These coordinates are sorted by the

	A	B	C	D	E	F	G	H	I	J	K	L	M	N
1	**M67 FIELD A MJD51985**													
2														
3														
4			51985_fielda_pass1_10images						51985_fielda_pass3_8images					
5	Reference	Coords	XCENTER	YCENTER	MAG	MERR	NEWX	NEWY	XCENTER	YCENTER	MAG	MERR	NEWX	NEWY
6	319.843	293.299	295.001	132.895	16.732	0.020	319.801	293.111	310.847	139.271	16.701	0.021	319.877	293.269
7	403.938	200.911	379.110	225.254	17.182	0.014	403.910	200.752	394.907	231.684	17.176	0.011	403.937	200.856
8	435.275	177.894	410.458	248.265	17.211	0.017	435.258	177.741	426.244	254.699	17.200	0.013	435.274	177.841
9	420.758	7.255	395.959	418.820	17.225	0.016	420.759	7.186	411.650	425.288	17.235	0.018	420.680	7.252
10	341.368	303.779	316.482	122.362	17.676	0.048	341.282	303.644	332.309	128.760	17.672	0.048	341.339	303.780
11	430.993	72.406	406.164	353.694	17.733	0.013	430.964	72.312	421.905	360.154	17.755	0.015	430.935	72.386
12	352.633	113.024	327.815	313.063	17.952	0.014	352.615	112.943	343.565	319.486	17.983	0.014	352.595	113.054
13	440.697	337.054	415.805	89.114	18.063	0.015	440.605	336.892	431.693	95.551	18.069	0.011	440.723	336.989
14	378.131	23.787	353.325	402.330	18.016	0.020	378.125	23.676	369.017	408.742	18.047	0.022	378.047	23.798
15	387.297	49.861	362.487	376.229	18.139	0.015	387.287	49.777	378.201	382.685	18.181	0.022	387.231	49.855
16	253.901	307.513	229.011	118.681	18.163	0.011	253.811	307.325	244.874	125.031	18.190	0.010	253.904	307.509
17	397.427	264.862	372.554	161.306	18.261	0.012	397.354	264.700	388.398	167.729	18.286	0.010	397.428	264.811
18	408.617	141.461	383.767	284.663	18.346	0.010	408.567	141.343	399.543	291.115	18.385	0.012	408.573	141.425
19	282.998	203.299	258.144	222.863	18.456	0.006	282.944	203.143	273.948	229.260	18.513	0.011	282.978	203.280
20	464.100	166.803	439.248	259.336	18.635	0.053	464.048	166.670	455.000	265.831	18.727	0.058	464.030	166.709
21	178.132	73.945	153.319	352.180	18.935	0.018	178.119	73.826	169.042	358.541	19.010	0.027	178.072	73.999
22	382.488	235.796	357.590	190.363	19.069	0.012	382.390	235.643	373.434	196.789	19.125	0.012	382.464	235.751
23	395.113	272.376	370.213	153.812	19.200	0.015	395.013	272.194	386.079	160.236	19.264	0.015	395.109	272.304
24	359.437	287.194	334.509	139.010	19.316	0.022	359.309	286.996	350.384	145.470	19.391	0.025	359.414	287.070
25	477.907	109.446	453.144	316.662	19.152	0.015	477.944	109.344	468.924	323.141	19.229	0.019	477.954	109.399
26	325.215	119.130	300.422	306.966	19.224	0.010	325.222	119.040	316.189	313.403	19.298	0.019	325.219	119.137

Fig. 52.— The initial configuration of a spreadsheet file used for sorting photometry results extracted using the `txdump` task.

instrumental magnitudes of stars on that particular frame, establishing an order of the objects; each row thus becomes the entry for one star's photometry. Since the expected order of the stars, selected by instrumental magnitude, is roughly constant, the data for each frame are sorted by this value. Instead of this, x or y coordinates could be chosen as the sort parameter, but the tracking problems discussed previously eliminate this as a practical option. The stars are initially labelled in order of increasing magnitude (Star 1, Star 2, etc.) before later cross-referencing with existing catalogs.

Before beginning these reductions, a reference frame was designated to which all the subsequent images in the time series would be registered to. The first usable frame from the first observing night, MJD 51935, was selected as the reference, and a

few "registration stars" were marked on this frame. These are stars which are readily identifiable by sight and hence are easy to locate on other frames; such stars were selected scattered around the frame such that at least two would be visible on any given frame no matter how severe the pointing and tracking errors from frame to frame. Two stars are required at a minimum to register images in both the $x - y$ plane as well as in rotation; a single star only will not account for any field rotation. The positions of all the registration stars on the reference frame were recorded.

Next, the registration shifts for each image to the reference frame were determined by finding as many of the registration stars as possible on those images and recording their positions in the spreadsheet with the photometry results from each. Cell arithmetic is used to calculate the shifts by subtracting the registration stars' positions on each frame from their positions on the reference and averaging the results; residuals, representing the error of the shift, are typically of order one pixel or less. The shifts are added to (or subtracted from, as the sign dictated) the star coordinates in columns "XCENTER" and "YCENTER"; the results appear in nearby columns "NEWX" and "NEWY". The cells in these latter two columns are matched from frame to frame for consistent identification of the same objects throughout the time series.

Matching stars in adjacent images is straightforward. The list of entries for a given image is compared to the same list for the image preceding it in the time series.

It is the last two columns of an image's entries, the calculated, shifted x and y that are matched. An example is shown in in Figure 53; a set of matching entries is

	AG	AH	AI	AJ	AK	AL	AM	AN	AO	AP	AQ	AR	AS	AT	AU
1															
2															
3															
4	51985_fielda_pass7_10images						51985_fielda_pass8_6images								
5	XCENTER	YCENTER	MAG	MERR	NEWX	NEWY	XCENTER	YCENTER	MAG	MERR	NEWX	NEWY			
6	337.284	134.463	16.765	0.015	319.816	293.381	345.257	131.386	16.689	0.013	319.997	293.463		391.181	134.243
7	421.212	226.974	17.230	0.007	403.744	200.870	429.136	223.899	17.137	0.008	403.876	200.950		382.740	229.223
8	452.523	250.031	17.267	0.009	435.055	177.813	460.446	246.960	17.171	0.009	435.186	177.889		339.077	373.327
9	437.698	420.620	17.272	0.007	420.230	7.224	445.572	417.549	17.174	0.005	420.312	7.300			
10	358.797	123.993	17.761	0.023	341.329	303.851	366.736	120.906	17.677	0.022	341.476	303.943			
11	448.045	355.494	17.835	0.010	430.577	72.350	455.936	352.422	17.730	0.007	430.676	72.427			
12	369.740	314.704	18.061	0.015	352.272	113.140	377.626	311.621	17.966	0.009	352.366	113.228			
13	458.194	90.891	18.191	0.012	440.726	336.953	466.136	87.833	18.088	0.010	440.876	337.016			
14	395.101	404.032	18.143	0.016	377.633	23.812	402.970	400.948	18.042	0.013	377.710	23.901			
15	404.326	377.978	18.277	0.016	386.858	49.866									
16	271.338	120.157	18.325	0.014	253.870	307.687									
17	414.798	163.005	18.410	0.012	397.330	264.839									
18	425.786	286.423	18.507	0.017	408.318	141.421	412.184	374.893	18.162	0.012	386.924	49.956			
19	300.280	224.407	18.652	0.019	282.812	203.437	279.270	117.051	18.217	0.010	254.010	307.798			
20					463.829	166.737	422.716	159.922	18.301	0.008	397.456	264.927			
21	195.211	353.597	19.213	0.027	177.743	74.247	433.676	283.350	18.394	0.010	408.416	141.499			
22	399.811	192.056	19.313	0.019	382.343	235.788	308.184	221.302	18.543	0.014	282.924	203.547			
23	412.509	155.515	19.460	0.017	395.041	272.329	203.092	350.456	19.088	0.023	177.832	74.393			
24	376.931	140.599	19.527	0.042	359.463	287.245	407.720	188.967	19.215	0.014	382.460	235.882			
25					477.817	109.423	420.417	152.436	19.358	0.014	395.157	272.413			
26	342.431	308.592	19.508	0.022	324.963	119.252	350.299	305.513	19.388	0.018	325.039	119.336			

Fig. 53.— The previous spreadsheet with a matching set of coordinates highlighted. Spaces have been inserted above the highlighted row in columns AM-AR to allow for pasting of matched entries.

highlighted in yellow. The next step would be to cut and paste the rightmost set of highlighted cells such that they coincide with the row of the highlighted cells on the left, constituting a positive match. Note that the values of the shifted x and y do not match exactly. This is due to imprecision in locating the reference star's centroid on the coadded images; typically this results from non-circular stellar profiles often seen in images from the GNAT telescope. Despite the imperfect correspondence of shifted coordinate values, if the coordinates are taken as integers, the match is typically perfect. At this stage, one would use the spreadsheet's "cut and paste" feature to relocate the rightmost highlighted entry to the same row containing its match on the left. In this manner, one can read across rows in the completed spreadsheet and see

the information for given, individual stars. To signify a positive match, the entire entry is underlined.

Some stars are not matched upon comparison of the lists. These stars' entries are cut and pasted in columns adjacent to the "working" star's entries; an example of this can be seen at extreme right in Figure 53. The reason why they are not matched lies in the selection of stars with an initial reference frame in the first place. Since the stars are sorted according to brightness, some stars which were not detected on the reference frame by `daofind` will appear interspersed in later frames' photometry with those in the order of the reference image. By setting these stars aside temporarily, the way is cleared for stars that can be matched quickly; these stars are then tacked on to the end of the list and matched toward the end of the matching process for a given coadded frame.

The matching process continues until all entries in each coadded frame from a given night are complete. To make these individual nights' data sets more manageable, they are allocated one night to each spreadsheet file with the naming convention "FieldX_NNNNN", where X is the letter identifier of the field, and NNNNN is the MJD. Each of these files contains a series of tabular data to be extracted for the next step in the process, termed "merging." With the photometry results for adjacent coadded images correlated, those results are formatted for extracting stellar ensembles, calculating ensemble differential magnitudes and plotting light curves.

It is advantageous to pair the instrumental magnitude for a given star with its

associated photometric precision for reasons including spot-checking of measurements

and ease of overplotting error bars on light curves. Thus some formatting steps are

performed to result in the convention of data as shown in Figure 54, showing the first

	A	B	C	D	E	F	G	H	I	J	K	L	M
1	INSTRUMENTAL MAGNITUDES												
2	FIELD "A"												
3													
4	51935												
5	DESIGNATION	F81		I8		I1		F151		none		F56	
6		Star	Err	Star	Err	Star	Err	Star	Err	Star	Err	Star	Err
7	MJD.FJD	1	1	2	2	3	3	4	4	5	5	6	6
8	51935.276019	14.043	0.031	14.591	0.040	14.601	0.039	14.648	0.036	14.969	0.065	15.233	0.031
9	51935.207280			15.333	0.009	15.357	0.010	15.354	0.009	15.837	0.015	15.890	0.004
10	51935.296088			15.832	0.014	15.845	0.017	15.857	0.010	16.342	0.047	16.413	0.008
11	51935.318183					14.422	0.029	14.456	0.028	14.816	0.069	15.051	0.021
12	51935.341435									15.239	0.055	15.360	0.018
13	51935.362454			15.725	0.037	15.726	0.036	15.748	0.030	16.205	0.065	16.346	0.028
14	51935.385058			15.652	0.036	15.630	0.034			16.169	0.069	16.290	0.030
15	51935.408113											15.329	0.033
16	51940.192697			15.366	0.008	15.396	0.008	15.372	0.007	15.841	0.032	15.907	0.005
17	51940.262789					15.381	0.018	15.394	0.017	15.869	0.042	15.960	0.016
18	51940.279549							15.224	0.021	15.698	0.048	15.794	0.020
19	51940.301736					14.891	0.010	14.910	0.015	15.372	0.047	15.472	0.016
20	51940.323854	15.490	0.016	15.949	0.006	15.982	0.008	15.983	0.013	16.464	0.035	16.537	0.014
21	51940.346111	15.187	0.016	15.614	0.009	15.646	0.010	15.643	0.009	16.102	0.042	16.209	0.014
22	51940.369676	14.929	0.020	15.369	0.007	15.404	0.009	15.397	0.008	15.916	0.030	15.966	0.013

Fig. 54.— The "Instrumental" sheet in the photometry results spreadsheet file. Stars are identified in rows 5-7 and alternate star-error across the columns. The first column is dedicated to the MJD of observation.

few rows and columns of the spreadsheet used to "merge" instrumental magnitudes

across many nights, called the "Instrumental" sheet. The first column is reserved

for the MJD at the time of observation, taken as close as possible to the midpoint

of the window of time defined by the range of images used in creating a coadded

result. Since the MJD is a parameter inserted into all the image headers of the data,

it is easily extracted for this purpose. Instrumental magnitudes begin in Column B

and alternate with the photometric errors as determined by DAOPHOT, described in

Section 6.5.5. The row labelled "Designation" gives, for each star and where available,

a common catalog designation found by matching coordinates of stars found in the
reference image to finder charts as in e.g. Eggen & Sandage (1964), Figure 1.

When the columns containing the instrumental magnitudes and photometric er-
rors are imported from the FieldX_NNNNN files, they must clearly be transposed
to rows in order to fit the format of the "merging" spreadsheet. This can be done
e.g., in Microsoft Excel, by selecting the columns containing these values, as shown
in Figure 55, copying the selected columns, and pasting them into the "merging"

	A	B	C	D	E	F	G	H	I	J	K	L	M	N
1	M67 FIELD A MJD51985													
2														
3														
4			51985_fielda_pass1_10images						51985_fielda_pass3_8images					
5	Reference	Coords	XCENTER	YCENTER	MAG	MERR	NEWX	NEWY	XCENTER	YCENTER	MAG	MERR	NEWX	NEWY
6	319.843	293.299	295.001	132.895	16.732	0.020	319.801	293.111	310.847	139.271	16.701	0.021	319.877	293.269
7	403.938	200.911	379.110	225.254	17.182	0.014	403.910	200.752	394.907	231.684	17.176	0.011	403.937	200.856
8	435.275	177.894	410.458	248.265	17.211	0.017	435.258	177.741	426.244	254.699	17.200	0.013	435.274	177.841
9	420.758	7.255	395.959	418.820	17.225	0.016	420.759	7.186	411.650	425.288	17.235	0.018	420.680	7.252
10	341.368	303.779	316.482	122.362	17.676	0.048	341.282	303.644	332.309	128.760	17.672	0.048	341.339	303.780
11	430.993	72.406	406.164	353.694	17.733	0.013	430.964	72.312	421.905	360.154	17.755	0.015	430.935	72.386
12	352.633	113.024	327.815	313.063	17.952	0.014	352.615	112.943	343.565	319.486	17.983	0.014	352.595	113.054
13	440.697	337.054	415.805	89.114	18.063	0.015	440.605	336.892	431.693	95.551	18.069	0.011	440.723	336.989
14	378.131	23.787	353.325	402.330	18.016	0.020	378.125	23.676	369.017	408.742	18.047	0.022	378.047	23.798
15	387.297	49.861	362.487	376.229	18.139	0.015	387.287	49.777	378.201	382.685	18.181	0.022	387.231	49.855
16	253.901	307.513	229.011	118.681	18.163	0.011	253.811	307.325	244.874	125.031	18.190	0.010	253.904	307.509
17	397.427	264.862	372.554	161.306	18.261	0.012	397.354	264.700	388.398	167.729	18.286	0.010	397.428	264.811
18	408.617	141.461	383.767	284.663	18.346	0.010	408.567	141.343	399.543	291.115	18.385	0.012	408.573	141.425
19	282.998	203.299	258.144	222.863	18.456	0.006	282.944	203.143	273.948	229.260	18.513	0.011	282.978	203.280
20	464.100	166.803	439.248	259.336	18.635	0.053	464.048	166.670	455.000	265.831	18.727	0.058	464.030	166.709
21	178.132	73.945	153.319	352.180	18.935	0.018	178.119	73.826	169.042	358.541	19.010	0.027	178.072	73.999
22	382.488	235.796	357.590	190.363	19.069	0.012	382.390	235.643	373.434	196.789	19.125	0.012	382.464	235.751
23	395.113	272.376	370.213	153.812	19.200	0.015	395.013	272.194	386.079	160.236	19.264	0.015	395.109	272.304

Fig. 55.— Highlighting columns in the spreadsheet containing instrumental magni-
tude and photometric error values for transposition into the "Instrumental" sheet.

spreadsheet by choosing Paste Special under the Edit menu and selecting the Trans-
pose checkbox. Because the spreadsheet software does not "know" that the entries
in the copied columns are to be formatted into separate (but adjacent) columns in
the "merging" spreadsheet, they appear interlaced, as shown in Figure 56. The in-
terpretation of a single column, reading down successive cells in the column, now

	A	B	C	D	E	F	G	H	I	J	K	L	M
80		Star	Err	Star	Err	Star	Err	Star	Err	Star	Err	Star	Err
81	MJD.FJD	1	1	2	2	3	3	4	4	5	5	6	6
82	51985.102384	16.732	17.182	17.211	17.225	17.676	17.733	17.952	18.063	18.016	18.139	18.163	18.261
83	51985.155440	0.020	0.014	0.017	0.016	0.048	0.013	0.014	0.015	0.020	0.015	0.011	0.012
84	51985.182037	16.701	17.176	17.200	17.235	17.672	17.755	17.983	18.069	18.047	18.181	18.190	18.286
85	51985.208669	0.021	0.011	0.013	0.018	0.048	0.015	0.014	0.011	0.022	0.022	0.010	0.010
86	51985.235741	16.677	17.156	17.186	17.233	17.639	17.754	17.990	18.067	18.049	18.186	18.195	18.291
87	51985.262431	0.024	0.015	0.017	0.015	0.063	0.011	0.015	0.014	0.019	0.018	0.010	0.010
88	51985.288889	16.803	17.172	17.203	17.227	17.684	17.764	18.001	18.105	18.061	18.197	18.233	18.326
89		0.047	0.014	0.015	0.015	0.046	0.012	0.017	0.011	0.018	0.017	0.009	0.008
90		16.788	17.265	17.302	17.318	17.767	17.868	18.099	18.226	18.163	18.173	18.349	18.430
91		0.034	0.021	0.022	0.015	0.057	0.013	0.021	0.017	0.014	0.014	0.013	0.014
92		16.765	17.230	17.267	17.272	17.761	17.835	18.061	18.191	18.143	18.277	18.325	18.410
93		0.015	0.007	0.009	0.007	0.023	0.010	0.015	0.012	0.016	0.016	0.014	0.012
94		16.689	17.137	17.171	17.174	17.677	17.730	17.966	18.088	18.042	18.162	18.217	18.301
95		0.013	0.008	0.009	0.005	0.022	0.007	0.009	0.010	0.013	0.012	0.010	0.008
96													
97													

Fig. 56.— The "Instrumental" sheet after transposing the highlighted columns in Figure 55.

is star-error-star-error etc. This entanglement must, unfortunately, be sorted out manually.

Separating the instrumental magnitudes from their associated errors is a three step process. First, gaps are inserted between the columns in Figure 56 to accommodate the columns that will contain the errors; second, the cells containing the errors in each column of mixed data are copied to the now-empty adjacent columns; and last, those cells in the column one starts with are deleted. The result is *rows* rather than columns that read star-error-star-error across, as indicated in the column headers in the first two rows of Figure 56.

To insert the gaps to separate columns containing the data, each column must be manually selected; this is done by pointing to the first cell in the first column, clicking and dragging to select the range of cells desired, and then repeating the process for adjacent columns while holding down the "Ctrl" key. This process is illustrated in

	A	B	C	D	E	F	G	H	I	J	K	L	M
80		Star	Err	Star	Err	Star	Err	Star	Err	Star	Err	Star	Err
81	MJD.FJD	1	1	2	2	3	3	4	4	5	5	6	6
82	51985.102384	16.732	17.182	17.211	17.225	17.676	17.733	17.952		18.063		18.016	
83	51985.155440	0.020	0.014	0.017	0.016	0.048	0.013	0.014		0.015		0.020	
84	51985.182037	16.701	17.176	17.200	17.235	17.672	17.755	17.983		18.069		18.047	
85	51985.208669	0.021	0.011	0.013	0.018	0.048	0.015	0.014		0.011		0.022	
86	51985.235741	16.677	17.156	17.186	17.233	17.639	17.754	17.990		18.067		18.049	
87	51985.262431	0.024	0.015	0.017	0.015	0.063	0.011	0.015		0.014		0.019	
88	51985.288889	16.803	17.172	17.203	17.227	17.684	17.764	18.001		18.105		18.061	
89		0.047	0.014	0.015	0.015	0.046	0.012	0.017		0.011		0.018	
90		16.788	17.265	17.302	17.318	17.767	17.868	18.099		18.226		18.163	
91		0.034	0.021	0.022	0.015	0.057	0.013	0.021		0.017		0.014	
92		16.765	17.230	17.267	17.272	17.761	17.835	18.061		18.191		18.143	
93		0.015	0.007	0.009	0.007	0.023	0.010	0.015		0.012		0.016	
94		16.689	17.137	17.171	17.174	17.677	17.730	17.966		18.088		18.042	
95		0.013	0.008	0.009	0.005	0.022	0.007	0.009		0.010		0.013	
96													
97													

Fig. 57.— Highlighting cells in the "Instrumental" sheet for insertion of columns. The gaps (as in columns I, K and M) will contain the copied errors from the mixed data columns.

the leftmost columns of Figure 57. Once all the columns are selected in this way, the gaps are inserted by shifting the columns to the right; from the Insert menu, the option "Cells..." is chosen and the "Shift cells right" button selected from the pop-up window. The result of this action is shown in the rightmost columns of Figure 57; upon completion of this step, all data will now be located under columns headed with "Star".

Next the cells containing the photometric errors are copied to the empty columns headed with "Err". To do this, the user must individually select these cells using the Ctrl-shift method described in the previous paragraph. The affected columns should look like the columns under headings Star 1, Star 2, Star 3 and Star 4 in Figure 58. It should be noted that because of the way spreadsheets work, this operation can only be performed on *one column at a time*. Attempting to copy the contents of multiple columns at once will produce incorrect results. Once selected, the cells in an

	A	B	C	D	E	F	G	H	I	J	K	L	M
80		Star	Err	Star	Err	Star	Err	Star	Err	Star	Err	Star	Err
81	MJD.FJD	1	1	2	2	3	3	4	4	5	5	6	6
82	51985.102384	16.732		17.182		17.211		17.225		17.676	0.048	17.733	0.013
83	51985.155440	0.020		0.014		0.017		0.016		0.048	0.048	0.013	0.015
84	51985.182037	16.701		17.176		17.200		17.235		17.672	0.063	17.755	0.011
85	51985.208669	0.021		0.011		0.013		0.018		0.048	0.046	0.015	0.012
86	51985.235741	16.677		17.156		17.186		17.233		17.639	0.057	17.754	0.013
87	51985.262431	0.024		0.015		0.017		0.015		0.063	0.023	0.011	0.010
88	51985.288889	16.803		17.172		17.203		17.227		17.684	0.022	17.764	0.007
89		0.047		0.014		0.015		0.015		0.046		0.012	
90		16.788		17.265		17.302		17.318		17.767		17.868	
91		0.034		0.021		0.022		0.015		0.057		0.013	
92		16.765		17.230		17.267		17.272		17.761		17.835	
93		0.015		0.007		0.009		0.007		0.023		0.010	
94		16.689		17.137		17.171		17.174		17.677		17.730	
95		0.013		0.008		0.009		0.005		0.022		0.007	
96													
97													

Fig. 58.— Selecting cells in the "Instrumental" sheet to disentangle instrumental magnitude and photometric error values.

individual column are copied and then pasted to the first cell in the empty column immediately to the left. The result will be a range of cells half the length of that of the column the cells were copied from; examples are shown in the entries for Stars 5 and 6 in Figure 58.

Finally, the cells containing the photometric errors just copied are removed from the columns in which they were pasted as interlaced with the instrumental magnitudes. The blank cells left behind are shifted up to "compact" the column of instrumental magnitudes. To do this, the cells containing the errors are selected exactly as described in the previous paragraph, but this time the user can continue to select across multiple columns as the Delete command is more precise in its effects than the Copy sequence from the last step. Once the cells to be deleted are selected, the user chooses Delete from the Edit menu and selects "Shift cells up" from the pop-up window. The result should resemble Figure 59.

	A	B	C	D	E	F	G	H	I	J	K	L	M
80		Star	Err	Star	Err	Star	Err	Star	Err	Star	Err	Star	Err
81	MJD.FJD	1	1	2	2	3	3	4	4	5	5	6	6
82	51985.102384	16.732		17.182		17.211		17.225		17.676	0.048	17.733	0.013
83	51985.155440	0.020		0.014		0.017		0.016		0.048	0.048	0.013	0.015
84	51985.182037	16.701		17.176		17.200		17.235		17.672	0.063	17.755	0.011
85	51985.208669	0.021		0.011		0.013		0.018		0.048	0.046	0.015	0.012
86	51985.235741	16.677		17.156		17.186		17.233		17.639	0.057	17.754	0.013
87	51985.262431	0.024		0.015		0.017		0.015		0.063	0.023	0.011	0.010
88	51985.288889	16.803		17.172		17.203		17.227		17.684	0.022	17.764	0.007
89		0.047		0.014		0.015		0.015		0.046		0.012	
90		16.788		17.265		17.302		17.318		17.767		17.868	
91		0.034		0.021		0.022		0.015		0.057		0.013	
92		16.765		17.230		17.267		17.272		17.761		17.835	
93		0.015		0.007		0.009		0.007		0.023		0.010	
94		16.689		17.137		17.171		17.174		17.677		17.730	
95		0.013		0.008		0.009		0.005		0.022		0.007	
96													
97													

Fig. 59.— Highlighting cells for copying within (and eventual deletion from) the "Instrumental" sheet.

Despite the arduous task of compiling this spreadsheet, the final results are very convenient to work with. Another sheet called "Ensemble" is created to rapidly select the ensemble and calculate the average magnitude of its stars for each frame on each night. A final sheet called "Differential" is generated in which the position of the cells mirrors that of the "Instrumental" sheet, but now the cells consist of each instrumental magnitude subtracted from the ensemble average for that frame. In this point the value of using spreadsheets lies: changing the ensemble results in a very rapid recalculation of all the dependent differential magnitudes. Columns containing the differential magnitudes and photometric errors are adjacent to each other, so the selection of columns for plotting light curves with error bars is very straightforward. The effect of changing the ensemble is thus reflected immediately in the light curves, making for a very interactive experience.

B.   Statistical corrections to differential magnitudes

For both of the IRAF-based photometry packages examined here, error estimates on individual instrumental magnitudes were generated by the built-in error model (see Equation 12). This is a simplified version of the error equations considered in Section 2 of this work. A calculation of the error from a more fundamental perspective is needed. To maximize the reliability of our resulting differential magnitudes, the formalism of Everett & Howell (2001) and their technique for "ultrahigh-precision CCD photometry" was adopted. This involves making some assumptions about the behavior of the statistics of the data and correcting the magnitudes as required. These corrections are of somewhat higher subtlety than the factors considered in Section 2, causing us to explain them in the context of an appendix to the work.

First, the instrumental magnitudes and magnitude uncertainties are calculated using the flux from star and sky in each case as reported by IRAF. The motivation for doing so, as Everett and Howell point out, is that the `phot` task returns only rough values for the precision of each magnitude measurement. The team re-derives an expression for the uncertainty in a single magnitude measurement, σ_*, from the earlier Howell derivation of the S/N given here in Section 2:

$$\sigma_* = 1.0857 \frac{\sqrt{N_* \times g + n_{pix}[1 + (\frac{n_{pix}}{n_{sky}})](N_{sky} \times g + R^2)}}{N_* \times g} \tag{A-1}$$

where N_{sky} is the number of counts from the star in the software aperture, g is the gain of the detector in electrons/ADU, n_{pix} is the number of pixels in the photometry aperture, n_{sky} is the number of pixels in the sky annulus, N_{sky} is the flux per pixel in the sky, and R is the read noise of the CCD in electrons. This model does not take into account dark current, which may be nontrivial in GNAT data.

Night-to-night variations in transparency, large-scale seeing, etc. are accounted for in the following manner. The instrumental magnitudes reported by `phot` are corrected by subtracting the residuals between the ensemble mean magnitude for a night, weighted by the uncertainties σ_* of each star in the ensemble, $\langle m_i \rangle$, and the mean of all the $\langle m_i \rangle$ on all M frames in the time series. The weighted means are defined by

$$\langle m_i \rangle = \frac{\sum_{i=1}^{N} \frac{m_i}{\sigma_i{}^2}}{\sum_{i=1}^{N} \frac{1}{\sigma_i{}^2}}, \tag{A-2}$$

and the corrected instrumental magnitude m by

$$m = m_{obs} - \left(\langle m_i \rangle - \frac{1}{M} \sum_{j=1}^{M} \langle m_i \rangle_j \right). \tag{A-3}$$

The third term in the last equation is a constant for all frames and "...serves only to reduce the absolute value of the correction," in the words of the authors. Using weighted means is the most technically correct method of calculating the ensemble mean in the sense that it explicitly takes into account the uncertainties of the ensemble

stars' instrumental magnitudes. In other words, it "folds" the errors into the value

for the mean magnitude of the ensemble, whereas a straight average assigns the same

uncertainty to each object. While choosing relatively bright stars for the ensemble

holds an advantage, clearly the presence of relatively faint stars in the mix can skew

the results dramatically.

The error in the correction to m_{obs} is calculated from the σ_* of the N ensemble

stars as follows:

$$\sigma_{ens}{}^2 = \frac{1}{\sum_{i=1}^{N} \frac{1}{\sigma_{i*}{}^2}}. \tag{A-4}$$

This error adds in quadrature with σ_* to give the total uncertainty of each magnitude

in the resulting light curve:

$$\sigma = \sqrt{\sigma_*{}^2 + \sigma_{ens}{}^2}. \tag{A-5}$$

One can see from this equation that reducing the σ_* (i.e., by choosing brighter stars)

of the ensemble stars will render σ_{ens} small enough that it can be negated in the

determination of the final σ.

These corrections to the data were made in order to derive the most reliable light

curves possible.

REFERENCES

Anupama, G. C., Kembhavi, A. K., Prabhu, T. P., Singh, K. P., & Bhat, P. N. 1994, A&AS, 103, 315

Baranne, A., Queloz, D., Mayor, M., Adrianzyk, G., Knispel, G., Kohler, D., Lacroix, D., Meunier, J.-P., Rimbaud, G., & Vin, A. 1996, A&AS, 119, 373

Borucki, W. J., Scargle, J. D., & Hudson, H. S. 1985, ApJ, 291, 852

Brown, T. M. 2000, in IAU Symposium, Vol. 202, E8–+

Chevalier, C. & Ilovaisky, S. A. 1991, A&AS, 90, 225

Cox, A. N. 2000, Allen's astrophysical quantities (Allen's astrophysical quantities, 4th ed. Publisher: New York: AIP Press; Springer, 2000. Editedy by Arthur N. Cox. ISBN: 0387987460)

Culver, R., Alvarez, E., Angione, R., Craine, E., Crawford, D., & Epand, D. 2000, in American Astronomical Society Meeting, Vol. 196, 0907+

Dacosta, G. S. 1992, in ASP Conf. Ser. 23: Astronomical CCD Observing and Reduction Techniques, 90+

Dinescu, D. I., Demarque, P., Guenther, D. B., & Pinsonneault, M. H. 1995, AJ, 109, 2090+

Eggen, O. J. & Sandage, A. R. 1964, ApJ, 140, 130+

Everett, M. E. & Howell, S. B. 2001, PASP, 113, 1428

Fan, X., Burstein, D., Chen, J. ., Zhu, J., Jiang, Z., Wu, H., Yan, H., Zheng, Z.,
    Zhou, X., Fang, L. ., Chen, F., Deng, Z., Chu, Y., Hester, J. J., Windhorst,
    A., Li, Y., Lu, P., Sun, W. ., Chen, W. ., Tsay, W. ., Chiueh, T. ., Chou, C. .,
    Ko, C. ., Lin, T. ., Guo, H. ., & Byun, Y. . 1996, AJ, 112, 628+

Giampapa, M. S., Craine, E. R., & Hott, D. A. 1995, Icarus, 118, 199

Gilliland, R. L. & Brown, T. M. 1988, PASP, 100, 754

Gilliland, R. L., Brown, T. M., Duncan, D. K., Suntzeff, N. B., Lockwood, G. W.,
    Thompson, D. T., Schild, R. E., Jeffrey, W. A., & Penprase, B. E. 1991, AJ,
    101, 541

Gilliland, R. L., Brown, T. M., Kjeldsen, H., McCarthy, J. K., Peri, M. L., Belmonte,
    J. A., Vidal, I., Cram, L. E., Palmer, J., Frandsen, S., Parthasarathy, M.,
    Petro, L., Schneider, H., Stetson, P. B., & Weiss, W. W. 1993, AJ, 106, 2441

GrandPre, C. A., Backman, D. E., Marschall, L. A., & Stauffer, J. R. 2001, in
    American Astronomical Society Meeting, Vol. 198, 4606+

Hall, J. C. & Lockwood, G. W. 2000, ApJ, 545, L43

Henry, G. W. 1996, in ASP Conf. Ser. 87: New Observing Modes for the Next Century,
    145+

Henry, G. W., Marcy, G., Butler, R. P., & Vogt, S. S. 1999, IAU Circ., 7307, 1+

Henry, G. W., Marcy, G. W., Butler, R. P., & Vogt, S. S. 2000, ApJ, 529, L41

Hobbs, L. M. & Thorburn, J. A. 1991, AJ, 102, 1070

Howell, S. B. 1992, in ASP Conf. Ser. 23: Astronomical CCD Observing and Reduction Techniques, 105+

Howell, S. B. 2000, Handbook of CCD astronomy (Handbook of CCD astronomy / Steve B. Howell. Cambridge, U.K. ; New York : Cambridge University Press, c2000. (Cambridge observing handbooks for research astronomers ; 2))

Howell, S. B., Everett, M. E., Esquerdo, G., Davis, D. R., Weidenschilling, S., & van Lew, T. 1999, in ASP Conf. Ser. 189: Precision CCD Photometry, 170+

Howell, S. B. & Merline, W. J. 1995, Exper. Astron., 6, 163+

Israelian, G., Santos, N. C., Mayor, M., & Rebolo, R. 2001, Nature, 411, 163

Janes, K. A., Goklani, V., Kraemer, N., Boyle, L., Yoss, K. M., & Miller, G. 1997, in American Astronomical Society Meeting, Vol. 191, 8010+

Jha, S., Charbonneau, D., Garnavich, P. M., Sullivan, D. J., Sullivan, T., Brown, T. M., & Tonry, J. L. 2000, ApJ, 540, L45

Kim, S., Chun, M. Y., Park, B., & Lee, S. 1996, Journal of Korean Astronomical Society, 29, 43

Massey, P. & Jacoby, G. H. 1992, in ASP Conf. Ser. 23: Astronomical CCD Observing
    and Reduction Techniques, 240+

Mathieu, R. D., Latham, D. W., Stassun, K. G., Torres, G., van den Berg, M., &
    Verbunt, F. 2000, in American Astronomical Society Meeting, Vol. 197, 4111+

Montgomery, K. A., Marschall, L. A., & Janes, K. A. 1993, AJ, 106, 181

Newberry, M. V. 1999, in ASP Conf. Ser. 189: Precision CCD Photometry, 74+

Phelps, R. L. & Janes, K. A. 1994, in American Astronomical Society Meeting, Vol.
    185, 10302+

Radick, R. R. 2000, in IAU Symposium, Vol. 203, E11−+

Rajamohan, R., Bhattacharyya, J. C., Kuppuswamy, K., & Subramanian, V. 1988,
    Bulletin of the Astronomical Society of India, 16, 139

Richer, H. B., Fahlman, G. G., Rosvick, J., & Ibata, R. 1998, ApJ, 504, L91

Roberts, J. H., Craine, E. R., & Giampapa, M. S. 2000, in American Astronomical
    Society Meeting, Vol. 197, 4004+

Sagar, R. & Pati, A. K. 1989, Bulletin of the Astronomical Society of India, 17, 6+

Sanders, W. L. 1971, A&A, 14, 226

Sandquist, E. & Shetrone, M. 2001, in American Astronomical Society Meeting, Vol. 198, 4201+

Santos, N. C., Israelian, G., & Mayor, M. 2001, A&A, 373, 1019

Schild, R. E. 1983, PASP, 95, 1021

Stassun, K. G., van den Berg, M., Mathieu, R. D., & Verbunt, F. 2002, A&A, 382, 899

Taylor, J. M., Craine, E. R., & Giampapa, M. S. 1999, in ASP Conf. Ser. 189: Precision CCD Photometry, 238+

Tucker, R. A. 1994, in American Astronomical Society Meeting, Vol. 185, 6304+

Tucker, R. A. 2002, 200th American Astronomical Society Meeting, 200, 0+

van den Berg, M., Stassun, K. G., Verbunt, F., & Mathieu, R. D. 2002, A&A, 382, 888

Vogt, S. S., Allen, S. L., Bigelow, B. C., Bresee, L., Brown, B., Cantrall, T., Conrad, A., Couture, M., Delaney, C., Epps, H. W., Hilyard, D., Hilyard, D. F., Horn, E., Jern, N., Kanto, D., Keane, M. J., Kibrick, R. I., Lewis, J. W., Osborne, J., Pardeilhan, G. H., Pfister, T., Ricketts, T., Robinson, L. B., Stover, R. J., Tucker, D., Ward, J., & Wei, M. Z. 1994, in Proc. SPIE Instrumentation in Astronomy VIII, David L. Crawford; Eric R. Craine; Eds., Volume 2198, p. 362, Vol. 2198, 362—+

Young, A. T., Genet, R. M., Boyd, L. J., Borucki, W. J., Lockwood, G. W., Henry, G. W., Hall, D. S., Smith, D. P., Baliumas, S. L., Donahue, R., & Epand, D. H. 1991, PASP, 103, 221

Zhao, J. L., Tian, K. P., Pan, R. S., He, Y. P., & Shi, H. M. 1993, A&AS, 100, 243

Zhou, A. 2001, Informational Bulletin on Variable Stars, 5096, 1+

This preprint was prepared with the AAS LaTeX macros v5.0.

Index